Evaluating the Performance of the ProtoDUNE–SP Detector using Michel Electrons

Aidan Reynolds

University College
University of Oxford

A thesis submitted for the degree of
Doctor of Philosophy

Hilary 2020

Abstract

This thesis presents the results of a study of electromagnetic interactions in the ProtoDUNE–SP liquid argon time projection chamber (LArTPC) detector. The LArTPC detector technology provides high spatial resolution on the final states of neutrino interactions, allowing interaction modes to be distinguished based on the event topology. In order to perform high precision measurements of ν_e in LArTPC detectors, electrons must be identified and their energy accurately reconstructed. In this work EM activity is studied in the 10–50 MeV range using Michel electrons as a source with a well defined energy spectrum. The sensitivity, bias, and energy scale are studied and the implications for neutrino physics in the Deep Underground Neutrino Experiment are discussed.

Evaluating the Performance of the ProtoDUNE–SP Detector using Michel Electrons

Aidan Reynolds

University College

University of Oxford

A thesis submitted for the degree of

Doctor of Philosophy

Hilary 2020

Abstract

This thesis presents the results of a study of electromagnetic interactions in the ProtoDUNE–SP liquid argon time projection chamber (LArTPC) detector. The LArTPC detector technology provides high spatial resolution on the final states of neutrino interactions, allowing interaction modes to be distinguished based on the event topology. In order to perform high precision measurements of ν_e in LArTPC detectors, electrons must be identified and their energy accurately reconstructed. In this work EM activity is studied in the 10–50 MeV range using Michel electrons as a source with a well defined energy spectrum. The sensitivity, bias, and energy scale are studied and the implications for neutrino physics in the Deep Underground Neutrino Experiment are discussed.

Contents

List of Figures

Glossary

DUNE . . . . . Deep Underground Neutrino Experiment.

EW . . . . . . Electroweak.

LArTPC . . . Liquid Argon Time Projection Chamber.

MLP . . . . . . Multi–layer Perceptron

PMNS . . . . . Pontecorvo—Maki—Nakagawa—Sakata

SSM . . . . . . Standard Solar Model

1
Introduction

Since the discovery of neutrino flavour oscillations, which implies that neutrinos have mass, neutrino physics has enjoyed a period of rapid development. The field has begun to transition into an era of precision, with many of the parameters governing these oscillations having been well constrained. The fact that neutrinos have mass, and the success of the PMNS theory in describing neutrino oscillations, leads to a number of fundamental questions which have important implications in both particle physics and cosmology:

- What is the mechanism giving rise to neutrino mass?

- Are neutrinos Dirac or Majorana particles?

- What is the absolute scale and ordering of the neutrino masses?

- Do neutrinos and anti–neutrinos oscillate differently, and would this help to explain the matter anti–matter asymmetry in the universe?

In addition to these questions from the neutrino physics community, the high resolution and large masses of modern neutrino detectors make them useful tools for both astronomy and astrophysics. 2017 has widely been considered as the dawn of multi–messenger astronomy, with a measurement of gravitational waves at LIGO

being correlated with measurements of a neutron star merger from electromagnetic telescopes [1]. This measurement was shortly followed by a similar correlation but in the neutrino sector between a high energy neutrino event in ICECUBE and a number of traditional telescopes [2]. Within our galaxy, neutrino detectors provide a unique opportunity to understand the underlying mechanisms in supernovae; in the case of such a supernova, the structure of the neutrino flux at earth provides a mechanism to measure effects in the early stages of the supernova burst which are inaccessible with electromagnetic measurements [3].

Each of these questions places unique constraints on the design of an appropriate neutrino detector. The discovery of a matter anti–matter asymmetry in neutrino oscillations can be answered by making precise measurements of neutrino oscillations. This requires reliably identifying the flavour and energy of neutrinos in order to measure the appearance and disappearance spectra associated with neutrinos produced in long baseline neutrino experiments. To identify the low energy electrons produced in supernova neutrino interactions, a detector with low thresholds and low backgrounds is required. The Deep Underground Neutrino Experiment (DUNE) aims to tackle these challenges by utilising the Liquid Argon Time Projection Chamber (LArTPC) technology, whose high spatial and calorimetric resolution allows for more accurate topological classification of neutrino interactions [4]. To achieve these goals, a significant programme of LArTPC research is ongoing with construction, reconstruction, and analysis methods all under development in a number of LArTPC based experiments [5–8].

This thesis presents an analysis of charged particle interactions in the ProtoDUNE–SP LArTPC detector. A hit classification algorithm is developed and a sample of Michel electrons is used to provide a measurement of electron energy bias for low energy electrons. The analysis described in this thesis uses data collected with the ProtoDUNE–SP detector between August and November 2018.

Michel electrons have an energy spectrum spanning 0–60 MeV; understanding electrons in this energy range is important as they are the same energy as those produced when neutrinos from supernova bursts interact. In a LArTPC at these

energies, the energy deposition of electrons transitions between ionisation dominated and radiation dominated regimes making for a particularly complicated combined event topology [9]. The work presented here details a reconstruction strategy based on augmenting hit identification from a convolution neural network with simple clustering to identify and reconstruct Michel electron events. Analysis of these Michel electron events in ProtoDUNE–SP data and simulation quantifies the energy scale and energy scale bias for low energy electrons in a surface level LArTPC detector; this measurement can provide valuable input to studies of supernova burst neutrinos in LArTPC detectors.

Chapter 2 provides a theoretical overview of neutrinos within the standard model. Interactions, oscillations, and production will be discussed summarising the current knowledge in the field, as well as open questions which will be studied in ongoing and upcoming experiments. The role of neutrinos in supernova bursts and the detection of such neutrinos in a LArTPC detector will be discussed in more detail.

The ProtoDUNE–SP experiment is described in chapter 3, including details of the beam line, detector, cosmic ray flux, and simulations. An overview of the LArTPC detection principle will be given with specific details of the ProtoDUNE–SP design. Some details of detector operations will be discussed, paying particular attention to the monitoring of the detector via the online data quality monitoring system.

Chapter 4 will cover details of electromagnetic energy loss in liquid argon. Electron and photon energy loss will be discussed as well as processes leading to electron-ion recombination. The impacts of these effects on electron reconstruction in liquid argon will be highlighted.

The main analysis of this thesis will be described in chapters 5 and 6. Details of a hit classification algorithm based on convolutional neural networks will be given and Michel electron reconstruction will be highlighted as an example use for the output of this algorithm. Michel electron production and energy loss in liquid argon will be discussed. This will be followed by details of the reconstruction strategy used in the Michel electron analysis. The reconstructed Michel electron spectrum will be

compared between data and simulation, and the energy resolution and energy scale bias for low energy electrons in the ProtoDUNE–SP detector will be estimated.

Chapter 7 will analyse the implications of the results of the Michel electron analysis for supernova neutrino physics in the DUNE experiment; the impacts of energy scale bias on these analyses will be investigated, and the possible performance of DUNE assuming the measured bias will be discussed.

A summary of the results presented in this thesis will be given in chapter 8 along with a discussion of the implications of these results for neutrino physics in LArTPC detectors.

2

Neutrino Physics

Contents

Despite being one of the most abundant particle in the universe, neutrinos are some of the most elusive; due to the fact that neutrinos can only interact via the weak interaction. The history of neutrino physics is therefore strongly connected to the discovery and study of weak interactions. Measurements by Chadwick in 1914 showed that the energy spectrum of electrons released in (β–decays was continuous, this is in contrast to discrete spectra observed in α and γ decays, and seemingly violates conservation of energy under the assumption of a two–body final state which was expected at the time. In order to solve this problem, Pauli postulated that the continuous energy spectrum could be explained if the energy

released in a β–decay could be shared with an additional neutral weakly interacting fermion which Pauli named the neutron. Fermi later renamed Pauli's fermion to the neutrino after Chadwick discovered the neutron in 1932. Despite claims that neutrinos might never be detected, neutrinos have now been discovered and they have been found to have a number of interesting properties which were not anticipated when neutrinos were first postulated.

This chapter will detail some of the history and theory of neutrino's and their interactions. Section 2.1 will give a brief historical overview of neutrino physics. Section 2.2 will introduce the theory of neutrinos in the Standard Model, followed by a discussion of neutrino oscillations in Section 2.3. Neutrino interactions will be discussed briefly in Section 2.4. Finally Section 2.5 will discuss the production and measurement of neutrinos from supernovae.

2.1   A Brief History of Neutrino Physics

The first attempt to incorporate the neutrino into a theoretical model came in 1934 when Fermi presented his theory of β–decay, in this theory the neutrino takes part in a four–point interaction with the other components of the β–decay interaction [10]. The incredible success of this theory in explaining the observed properties of β–decays provided strong evidence for the neutrinos existence, however, in 1934 after using Fermi's theory to predict the strength of neutrino interactions, H. Bethe and R. Peierls found that the interactions were so weak that they might never be observed, a prediction that held true for over 20 years [11].

The first breakthrough in experimental neutrino physics would come in 1956. F. Reines and C. Cowan were attempting to measure positrons produced in inverse β–decay interactions,

$$\overline{\nu}_e + p \rightarrow n + e^+. \tag{2.1}$$

A detector containing 1400 litres of liquid scintillator was used to measure the large flux of electron anti–neutrinos in the vicinity of the Savannah River nuclear reactor. They observed a large increase in the rate of positron events when the reactor

was on compared to when the reactor was switched off, the first experimental evidence for the existence of neutrinos [12].

The discovery of the electron neutrino opened the door to answer questions of neutrino flavour. As neutrinos are produced alongside a charged lepton it is natural to compare the properties of neutrinos with their partners in the weak interaction. At the time of the discovery of the neutrino there were two known charged leptons, the electron and the muon, and physicists asked whether the neutrinos produced alongside muons are different from those produced alongside electrons. In 1962, Lederman et al discovered the muon neutrino at Brookhaven National Laboratory; by creating a beam of muon–associated neutrinos from decaying pions, and observing the leptons produced in neutrino interactions after all other particles had been absorbed. They found that only muons where produced in the resulting neutrino interactions, and therefore the neutrinos produced were only ever associated with a muon, which shows that neutrinos are produced with a distinct flavour in weak interactions [13].

In 1973 the Gargamelle experiment at CERN released results on the measurement of neutrino interactions [14]. They observed a new type of interaction, neutral current (NC) interactions:

$$\nu_l + N \rightarrow \nu_l + X \tag{2.2}$$

which are characterised by the lack of an observable charged lepton in the final state. Unlike charged current (CC) interactions, which are mediated by the charged W boson, these NC interactions are mediated by the neutral Z^0 boson.

With the discovery of the tau–lepton in 1977 it was expected that there should be an associated tau neutrino, however, it wouldn't be detected until 2001 by the DONUT experiment [15]. In the experiment, tau neutrinos where produced from the decay of charmed mesons produced in collisions between protons and a stationary target. The neutrino interactions where detected in emulsion detectors, where the unique geometry of the interaction, in which a short tau track is produced

at the vertex followed by a long muon track, allowed them to be distinguished from other decays.

While additional neutrino species are possible, data from measurements of the Z boson line–shape at LEP in 1992 restricts the number of active light neutrino species to be three [16]. An active light neutrino is any neutrino with $m_\nu < \frac{m_Z}{2}$ that can interact with the Z boson, such that the decay $Z \to \nu\nu$ is possible.

Alongside the discovery of three different types of neutrino, there were interesting results when observing neutrinos produced in the Sun. The flux of neutrinos from the Sun at the earth surface had been predicted with Bachall's Standard Solar Model (SSM), however, in 1968 when Davis et al measured the flux in the Homestake experiment they found a deficit with respect to the prediction of the SSM [17, 18], the so called solar neutrino problem. In the Homestake experiment electron neutrinos where being measured via there inverse beta decay interactions with the chlorine in the target,

$$v_e + {}^{37}\mathrm{Cl} \to {}^{37}\mathrm{Ar} + e^-. \tag{2.3}$$

The neutrino interaction rate was measured by counting the number of argon atoms in the chlorine tank by capturing them on helium gas which was periodically bubbled through the chamber.

In addition to the solar neutrino problem, a similar deficit was observed in 1988 for muon neutrinos produced during cosmic ray showers. The Kamiokande experiment was able to measure both electron and muon neutrino interactions via the cerenkov radiation produced by the charged leptons in water. Their data was consistent with the expected rate of electron neutrinos from the atmosphere, however, a deficit of muon neutrinos was observed [19].

The next generation of the Kamiokande experiment, Super–Kamiokande, aimed to understand the observed deficit of atmospheric muon neutrinos with a larger water cerenkov detector capable of resolving the angular distribution of atmospheric neutrino interactions. Super–Kamiokande consists of a cylindrical vessel containing 50 kt of ultra pure water, surrounded by an array of around 13,000 photomultiplier

tubes to detect the cerenkov light. Electron and muon neutrinos can be distinguished based on the pattern of cerenkov light that is left in the detector; muons leave clear cerenkov rings in the detector due to their higher mass while electrons, which can scatter and shower, tend to leave diffuse "fuzzy" rings on the wall of the detector. In 1998, Super–Kamiokande published measurements of the flux of atmospheric muon neutrinos as a function of azimuthal angle [20]. Since these neutrinos are created a short distance from the earths surface, the incoming angle of the neutrino can be used to estimate the distance travelled by the neutrino before arriving at the detector; the down–going neutrinos have only travelled a short distance in the atmosphere (~ 10km), while the up–going neutrinos have travelled through the entire earth to reach the detector ($\sim 13,000$km). Figure 2.1, shows the flux of neutrinos measured by Super Kamiokande as a function of L/E_ν; the muon neutrino flux is consistent with the no oscillation prediction at small L/E_ν, however, for large L/E_ν a clear deficit is observed.

While it wouldn't completely solve the solar neutrino problem, the Sudbury Neutrino Observatory (SNO) was able to provide unique insight into the observed solar neutrino fluxes in 2002. Unlike other water cerenkov detectors, SNO was filled with heavy water, D_2O, instead of its lighter isotope. The use of heavy water gives rise to additional neutrino interactions which allowed the SNO experiment to distinguish between three different interaction modes: charged current (CC), neutral current (NC), and elastic scattering (ES). Each mode is sensitive to different parts of the solar neutrino flux, including some sensitivity to the muon neutrino and tau neutrino fluxes via the NC and ES interactions. Analysis of the data for each of the three unique interaction modes lead to a measurement of the flavour composition of the solar neutrino flux at earth, while also finding the overall neutrino flux at earth to be consistent with the SSM. Figure 2.2 shows the composition of the solar neutrino flux as measured in the SNO experiment [21], the flux prediction based on the measured rate of NC events is consistent with the predictions of the SSM. The composition of solar neutrinos measured in the SNO experiment is not a result of neutrino oscillations, instead it is the result of the effect of matter
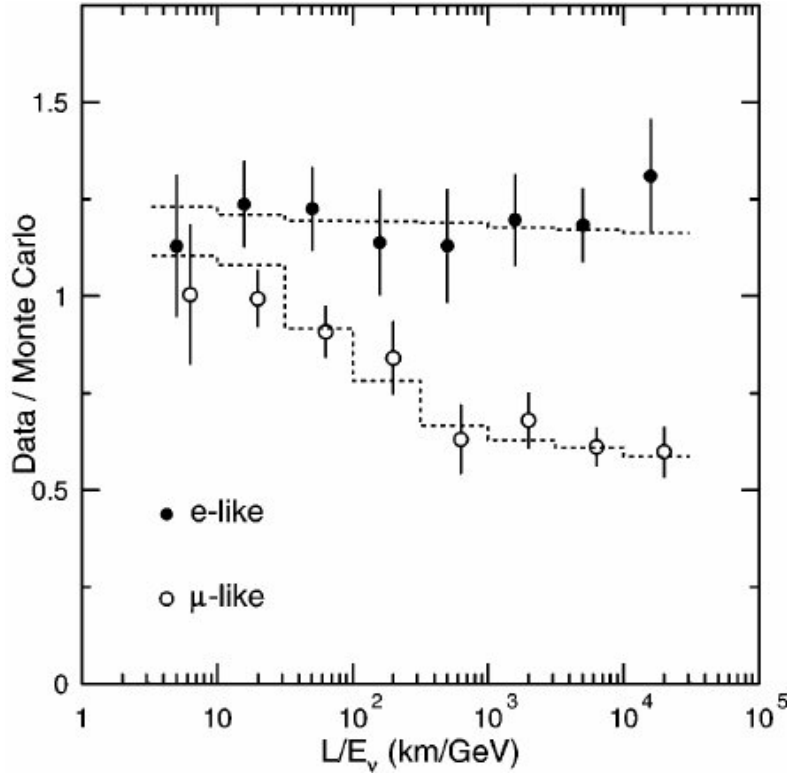
Figure 2.1: Ratio of data to Monte Carlo for electron and muon neutrino fluxes measured by the Super Kamiokande experiment as a function of L/E_ν. The Monte Carlo prediction is based on the assumption of no oscillations. The muon neutrino flux is consistent with the no oscillation prediction at small L/E_ν, however, for large L/E_ν a clear deficit is observed. The best fit under the assumption of atmospheric $(\nu_\mu \to \nu_\tau)$ oscillations is shown, the best fit parameters are $\Delta m^2 = 2.2 \times 10^{-3}\text{eV}^2$, and $\sin^2 2\theta = 1$. [20].

on the neutrino propagation in the Sun via the Mikheyev–Smirnov–Wolfenstein (MSW) effect. However at the time a number of solutions were still possible: MSW conversion, decoherence, neutrino decay, and others [22].

An L/E_ν dependence in the neutrino flux would have to be measured in order for neutrino oscillations to be the unique solution to the problem. To make this measurement a much shorter neutrino baseline would be needed, along with a source of neutrinos with a small energy spread, and a detector with good energy resolution. In 2002 the Kamioka Liquid Scintillator Anti–neutrino Detector (KamLAND) experiment measured $\overline{\nu}_e$ oscillations from a number of nuclear reactors, which produce neutrinos at the MeV scale [23, 24]. Along with an overall deficit of neutrino events, they were able to use the high energy resolution of the KamLAND detector to measure an L/E_ν dependence of the $\overline{\nu}_e$ survival probability. Figure 2.3,
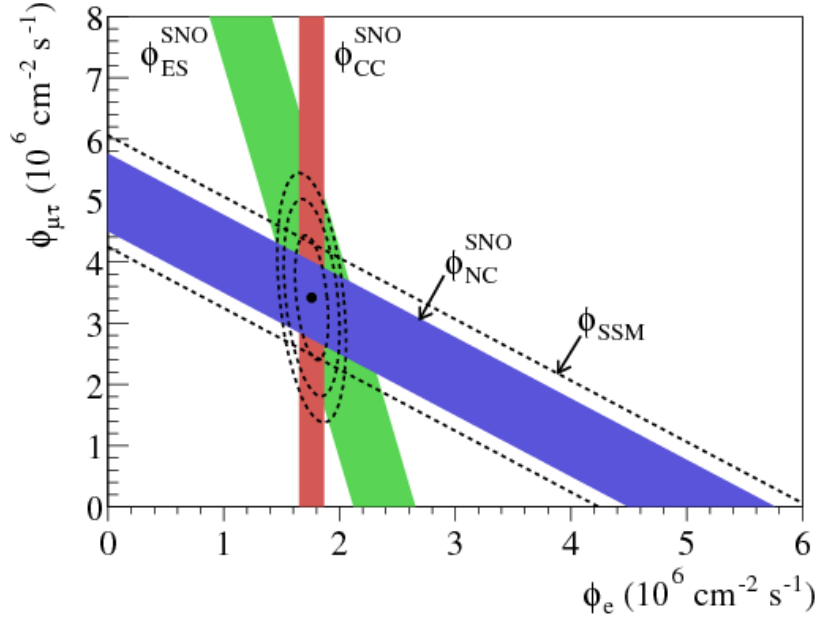
Figure 2.2: Solar neutrino flux composition as measured by the SNO experiment. The coloured bands represent the measured flux of charged current (CC), neutral current (NC), and elastic scattering (ES) events, including a $\pm 1\sigma$ spread. The central contours represent 68%, 95%, and 99% probability contours for the joint ϕ_e and $\phi_{\mu\tau}$ fit. The dashed lines represent the predicted flux of ^{8}B neutrinos based on the standard solar model [21].

shows the ratio of the observed neutrino flux with the no oscillation predicted flux as a function of L/E_ν, a clear dependence can be seen and this data was enough to prove that neutrino oscillations were the only solution to the solar neutrino problem.

Based on the results of the above experiments, it was assumed that electron and muon type neutrinos where oscillating into tau type neutrinos which where then left undetected. The first evidence of tau neutrino production in oscillations wouldn't come until 2010, when the OPERA experiment measure a ν_τ candidate in a ν_μ beam. They used similar emulsion detectors to those used to discover the ν_τ in DONUT, and a muon neutrino beam on a 730km baseline from CERN to LNGS. By the end of the experiment a total of 10 candidate events have been observed, 6.1 σ above the expected background [25, 26].

Since the discovery of neutrino oscillations, many more experiments have made measurements of oscillations and the majority of the parameters of the neutrino oscillation models have been constrained. Important results of these experiments for
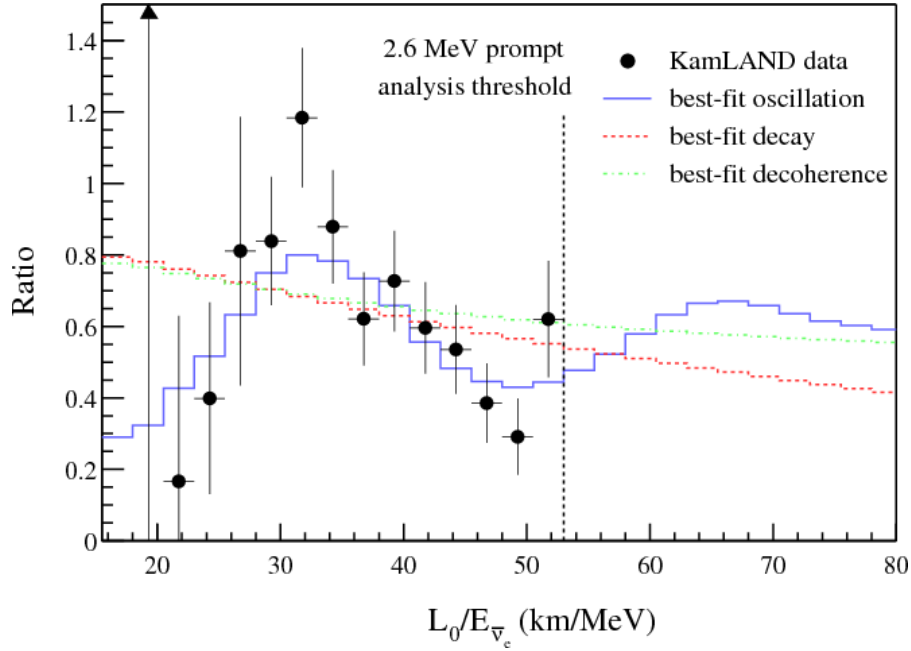
Figure 2.3: Ratio of observed neutrino flux to the predicted flux in the absence of neutrino oscillations in the KamLAND experiment as a function of L/E_ν. The data are fit with three different models: the red dashed line represents the best fit to a neutrino decay model, the green dashed line is for a decoherence model, and the solid blue line represents the best fit of the data to a neutrino oscillation model. The neutrino oscillation model, which has a different shape to the other two models, is found to give the best fit to the data [24].

constraining the parameters of the neutrino oscillation models will be highlighted in Section 2.3, along with a theoretical overview of neutrino oscillations.

Neutrino oscillations are currently the only measured effect that is not explained in the SM, and their observation proves that neutrinos are massive. However, the absolute mass of neutrinos is still unknown. The question of absolute neutrino mass, is one of a number of open questions in neutrino physics. At the time of writing, the main open questions in neutrino physics are:

- What are the absolute masses of the neutrinos?

- What is the mass ordering of the neutrino mass eigenstates?

- Is there CP violation in the neutrino sector?

- Are neutrinos Dirac ($\nu \neq \bar{\nu}$) or Majorana ($\nu = \bar{\nu}$) particles?

2.2 Neutrinos in the Standard Model

In the standard model neutrinos form part of the left handed fermion doublets

$$\psi_i = \begin{pmatrix} \nu_i \\ l_i^- \end{pmatrix}, \tag{2.4}$$

where they are paired with a charged lepton of the same flavour in CC interactions, and i represents any of the three known generations of leptons. Their interactions with other particles in the standard model is determined by the electroweak (EW) theory, which is derived from the $SU(2) \times U(1)$ gauge group. The neutrino fields enter into the SM Lagrangian in the CC and NC interactions:

$$\mathcal{L}^{CC} = -\frac{g_W}{2\sqrt{2}} \, j_\alpha^{CC}(x) \, W^\alpha(x) \; + \; h.c. \tag{2.5}$$

$$\mathcal{L}^{NC} = -\frac{g_W}{2cos\theta_W} \, j_\alpha^{NC}(x) \, Z^\alpha(x) \; + \; h.c. \tag{2.6}$$

Here

$$j_\alpha^{CC}(x) = 2 \sum_{\beta=e,\mu,\tau} \overline{\nu_\beta}(x) \, \gamma_\alpha \, l_\beta(x) \tag{2.7}$$

is the leptonic charged–current and

$$j_\alpha^{NC}(x) = \sum_{\beta=e,\mu,\tau} \overline{\nu_\beta}(x) \, \gamma_\alpha \, \nu_\beta(x) \tag{2.8}$$

is the neutrino neutral–current, $W^\alpha(x)$ and $Z^\alpha(x)$ are the vector boson fields for the $W^\pm$ and Z^0 bosons respectively, g_W is the electroweak coupling constant, and θ_W is the Weinberg angle.

Mass is included in the standard model through the Dirac mass term in the Lagrangian

$$\begin{aligned} \mathcal{L}^D &= m_D \overline{\psi}\psi \\ &= m_D \overline{(\psi_L + \psi_R)}(\psi_L + \psi_R) \\ &= m_D (\overline{\psi}_L \psi_R + \overline{\psi}_R \psi_L) \end{aligned} \tag{2.9}$$

where L and R represent the left and right handed components of the field. The lack of right handed neutrino states therefore means neutrinos are assumed to

be massless in the standard model. For massive neutrinos to exists the standard model, right handed neutrino fields need to be introduced. In addition, it is still not whether neutrinos are Dirac or Majorana particles, meaning that additional Majorana mass terms are possible. A more general neutrino mass term including both Dirac and Majorana components is

$$\mathcal{L}^{D+M} = \begin{pmatrix} \bar{\nu}_L & \bar{\nu}_R \end{pmatrix} \begin{pmatrix} m_L & m_D \\ m_D & m_R \end{pmatrix} \begin{pmatrix} \nu_L \\ \nu_R \end{pmatrix}. \tag{2.10}$$

2.3 Neutrino Oscillations

Neutrino oscillations are a result of quantum mechanical interference between different massive neutrino eigenstates. The mass eigenstates are produced and measured coherently because the energy and momenta of the neutrino states are not measured with enough precision to distinguish the mass eigenstate of the neutrino.

Neutrinos are produced in a state of definite flavour, $\alpha = e, \mu, \tau$, in charged current (CC) and neutral current (NC) weak interactions,

$$W^+ \to l_\alpha^+ \nu_\alpha, \quad W^- \to l_\alpha^- \nu_\alpha, \quad Z \to \nu_\alpha \overline{\nu_\alpha}. \tag{2.11}$$

The CC processes are used in neutrino oscillation experiments because they give information about the initial flavour state of the neutrinos. These processes are governed by the Lagrangian of the CC leptonic interactions, as in Equation 2.5.

Neutrino flavour states, ν_α, can be represented as a superposition of massive neutrinos in any case where the energy and momentum of the neutrino is not known with enough precision to determine the neutrino mass. The basis transformation takes the form

$$\nu_\alpha = \sum_k U_{\alpha k}^* \nu_k, \tag{2.12}$$

where ν_k are the neutrino mass eigenstates, and U is a unitary mixing matrix.

The representation of neutrino flavour states as a superposition of mass eigenstates gives rise to the phenomenon of neutrino oscillations. Consider a neutrino produced in a CC weak interaction with flavour α. This neutrino flavour state is

described by equation 2.12, where U is a unitary mixing matrix called the PMNS (Pontecorvo, Maki, Nakagawa, and Sakata) matrix. For three flavour mixing the PMNS matrix takes the form:

$$
U = \begin{pmatrix} U_{e1} & U_{e2} & U_{e3} \\ U_{\mu 1} & U_{\mu 2} & U_{\mu 3} \\ U_{\tau 1} & U_{\tau 2} & U_{\tau 3} \end{pmatrix}. \tag{2.13}
$$

In a vacuum, the neutrino mass states are eigenstates of the free particle Hamiltonian

$$
\mathcal{H} \left| \nu_k \right\rangle = E_k \left| \nu_k \right\rangle, \tag{2.14}
$$

with energy

$$
E_k = \sqrt{\mathbf{p}^2 + m_k^2}. \tag{2.15}
$$

So the solutions to the time dependent Schrodinger equation are plane waves

$$
\left| \nu_k(t) \right\rangle = e^{-iE_k t} \left| \nu_k \right\rangle. \tag{2.16}
$$

The time evolution of the initial flavour state is:

$$
\left| \nu_\alpha(t) \right\rangle = \sum_k U_{\alpha k}^* e^{-iE_k t} \left| \nu_k \right\rangle. \tag{2.17}
$$

The mass states can be written in terms of the flavour states by inverting Equation 2.12:

$$
\left| \nu_k \right\rangle = \sum_\alpha U_{\alpha k} \left| \nu_\alpha \right\rangle. \tag{2.18}
$$

Here, we have used the fact that the states form an orthonormal basis, $\langle \nu_\alpha | \nu_\beta \rangle = \delta_{\alpha\beta}$, and that the transformation matrix is unitary, $UU^\dagger = \mathbf{1}$.

Substituting Equation 2.18 into the time evolution of the flavour state, Equation 2.17, gives:

$$
\left| \nu_\alpha(t) \right\rangle = \sum_{\beta=e,\mu,\tau} \left(\sum_k U_{\alpha k}^* e^{-iE_k t} U_{\beta k} \right) \left| \nu_\beta \right\rangle \tag{2.19}
$$

So as the initial flavour state evolves with time, it becomes a superposition of different flavour states; this process is known as neutrino oscillation. The probability of finding the initial neutrino in flavour state ν_β as a function of time is:

$$P_{\nu_\alpha \to \nu_\beta}(t) = |\langle \nu_\beta | \nu_\alpha(t) \rangle|^2 \tag{2.20}$$

$$= \sum_{kj} U_{\alpha k}^* U_{\beta k} U_{\alpha j} U_{\beta j}^* e^{-i(E_k - E_j)t}. \tag{2.21}$$

All neutrino oscillation experiments to date operate in a regime where $E \gg m$, in this regime the relativistic energy relation for neutrinos can be expanded as $E_k \simeq E + \frac{m_k^2}{2E}$, where $E = |p|$. Hence,

$$E_k - E_j \simeq \frac{m_k^2 - m_j^2}{2E} = \frac{\Delta m_{kj}^2}{2E}. \tag{2.22}$$

In addition, neutrino oscillation experiments do not measure the neutrino propagation time t. Instead, they measure the propagation distance, L, also known as the baseline. In the ultra–relativistic limit we can approximate $t \simeq L$ in natural units. As a result, Equation 2.20 can be approximated as:

$$P_{\nu_\alpha \to \nu_\beta}(t) = \sum_{kj} U_{\alpha k}^* U_{\beta k} U_{\alpha j} U_{\beta j}^* e^{-i \frac{\Delta m_{kj}^2 L}{2E}}. \tag{2.23}$$

Splitting the sum into its real and imaginary parts emphasises the possibility of CP–violation in neutrino oscillations. CP–violation occurs if the imaginary component of the matrix product is none–zero.

$$P_{\nu_\alpha \to \nu_\beta}(t) = \delta_{\alpha\beta} - 4 \sum_{j>k} \mathrm{Re}(U_{\alpha k}^* U_{\beta k} U_{\alpha j} U_{\beta j}^*) \sin^2(\frac{\Delta m_{kj}^2 L}{2E})$$

$$\pm 2 \sum_{j>k} \mathrm{Im}(U_{\alpha k}^* U_{\beta k} U_{\alpha j} U_{\beta j}^*) \sin^2(\frac{\Delta m_{kj}^2 L}{2E}). \tag{2.24}$$

The third term here is responsible for CP violation in neutrino oscillations, the positive case corresponds to neutrinos and the negative case is for anti–neutrinos.

The probability of oscillation is therefore dependent on properties determined by nature, in the form of PMNS matrix elements and mass squared differences, and those which can be chosen by experiments, the distance travelled, L, and the neutrino energy, E. In a vacuum, the oscillation probability is only dependent on the

magnitude of the squared mass difference between the neutrino mass eigenstates, it gives no information about the absolute masses of the neutrino eigenstates or their ordering. The question of the absolute neutrino masses cannot be answered in neutrino oscillation experiments, to get access to the absolute masses other experiments are required, e.g. direct mass measurements with tritium beta decay experiments such as KATRIN [**TODO**]. Neutrino oscillation experiments can give insight on the ordering of the neutrino masses, but to understand how the oscillations of neutrinos in matter must be considered.

2.3.1   Neutrino Oscillations in Matter

In real neutrino oscillation experiments, neutrinos travel through matter, whether it be the matter in a star or the earths crust. Neutrinos propagating in matter are subject to an additional potential due to the interaction of the neutrinos with the electrons and nucleons in the medium. This interaction can significantly modify the flavour of the beam relative to oscillations in vacuum.

In matter neutrinos can scatter off particles by interacting with either the charged–current or neutral–current interactions as shown in Figure 2.4. These interactions give rise to additional effective potentials which the neutrinos experience while they are travelling,

$$V_{CC} = \sqrt{2}G_F N_e, \tag{2.25}$$

$$V_{NC}^f = \sqrt{2}G_F N_f g_V^f, \tag{2.26}$$

where G_F is the Fermi weak coupling constant, N_e and N_f are the number densities of electrons and other fermions respectively, and g_V^f is the vector coupling constant for a given fermion f.

Neutral–current scattering is independent of neutrino flavour meaning that the additional potential does not affect oscillations. However, the charged current potential is only present for ν_e, and therefore it will impact the mass eigenstates by different amounts depending on their relative ν_e component.

(a) Charged current scattering. **(b)** Neutral current scattering.
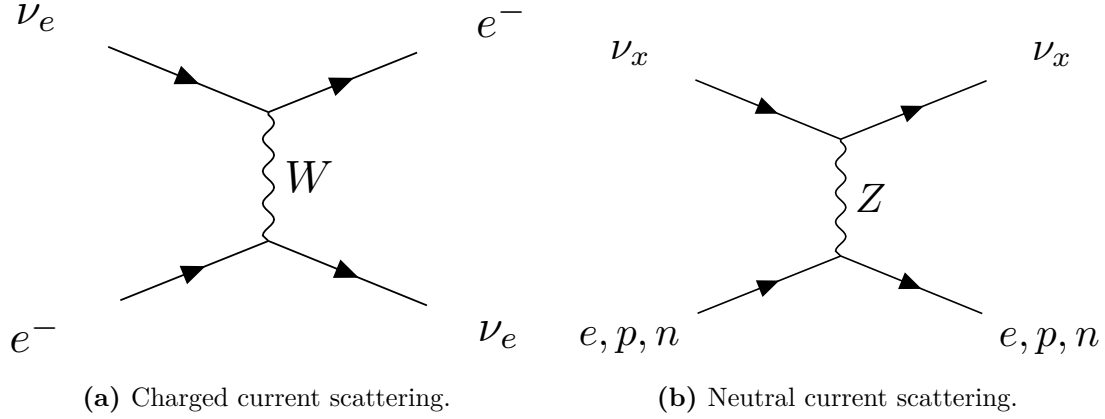
Figure 2.4: Feynman diagrams for neutrino scattering in matter.

A full description of the effects of matter on neutrino oscillations is beyond the scope of this thesis, although it is discussed at length in other sources such as [27]. For the purposes of this thesis it is sufficient to note that the propagation of neutrinos in matter changes the oscillations probabilities, and this must be taken into account by oscillation experiments.

One implication of the effects of matter on oscillations is that it introduces sensitivity to sign of the mass splittings [27], allowing experiments to determine the relative ordering of the neutrino masses. By considering the pattern of neutrino oscillations in the Sun it is possible to determine that $\Delta m_{21}^2 > 0$ [28]. The sign of the remaining mass splitting, Δm_{32}^2, remains unknown which leaves two possibilities for the ordering of neutrino masses. Normal ordering (NO), in which $m_3 > m_2 > m_1$, and inverted ordering (IO), where $m_1 > m_2 > m_3$, which are depicted in Figure 2.5.
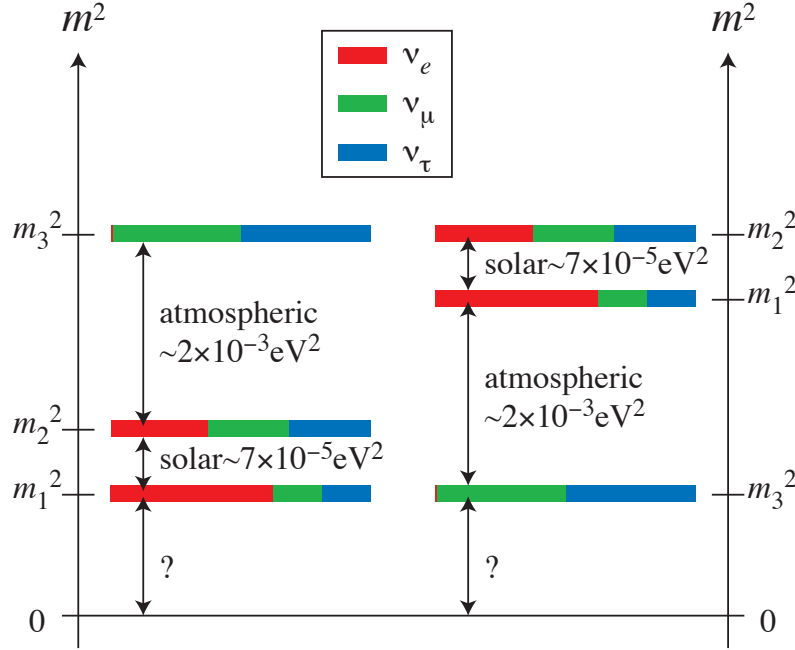
Figure 2.5: The two possible neutrino mass orderings. Left: normal ordering. Right: inverted ordering. Figure from [29].

2.3.2 Current Knowledge and Open Questions

At the time of writing the most widely accepted model of neutrino oscillations involves three neutrino mass eigenstates. In this model, the PMNS matrix is often parametrised in terms of three mixing angles θ_{12}, θ_{13}, and θ_{23} and three CP–violating phases δ_{CP}, α_1, and α_2:

$$
U = \underbrace{\begin{pmatrix} c_{12} & s_{12} & 0 \\ -s_{12} & c_{12} & 0 \\ 0 & 0 & 1 \end{pmatrix}}_{\text{Solar}} \underbrace{\begin{pmatrix} c_{13} & 0 & s_{13}e^{-i\delta_{CP}} \\ 0 & 1 & 0 \\ -s_{13}e^{i\delta_{CP}} & 0 & c_{13} \end{pmatrix}}_{\text{Cross–mixing}} \underbrace{\begin{pmatrix} 1 & 0 & 0 \\ 0 & c_{23} & s_{23} \\ 0 & -s_{23} & c_{23} \end{pmatrix}}_{\text{Atmospheric}} \underbrace{\begin{pmatrix} e^{i\frac{\alpha_1}{2}} & 0 & 0 \\ 0 & e^{i\frac{\alpha_2}{2}} & 0 \\ 0 & 0 & 1 \end{pmatrix}}_{\text{Majorana}} .
$$

$$(2.27)$$

Expressing the mixing matrix like this factorises the matrix into its components, which are responsible for oscillations in different regimes. The first component contains only θ_{12} which is dominant in Solar neutrino oscillations. The third component dominates in the mixing of atmospheric neutrinos, and is a function of θ_{23}. The final element which is significant for neutrino oscillations is the second

component, known as the cross–mixing matrix. This component depends on the final mixing angle, θ_{13} and on one of the CP–violating phases, δ_{CP}. If δ_{CP} is non–zero then U will have complex components in off diagonal elements, leading to different probabilities for CP flipped oscillations, $P(\nu_\alpha \rightarrow \nu_\beta) \neq P(\overline{\nu_\alpha} \rightarrow \overline{\nu_\beta})$. Discovery of this effect, which is known as CP–violation, is one of the major goals of the next generation of neutrino oscillation experiments.

The final matrix in the factorised version of the PMNS matrix is called the Majorana component. The CP–violating phases in this matrix cancel in the oscillation probability, and so they can't be measured in neutrino oscillation experiments. In fact, they only lead to physical effects if neutrinos are Majorana particles (i.e. if they are there own antiparticle). Other experiments are required to determine in neutrinos are Majorana particles, for example, neutrinoless double beta decay experiments such as CUORE [30], NEXT [31], and SNO+ [32]. The question of the nature of neutrinos has implications on neutrino mass generation, as mentioned in Equation 2.10.

A large number of neutrino oscillation measurements now exist in the form of solar, reactor, atmospheric, and accelerator neutrino experiments. When combined results from these experiments give us our current best estimates of the neutrino oscillation parameters. The current combined results, from the 2018 Review of Particle Physics by the Particle Data Group [28], along with the major contributing experiments for each measurement are summarised below.

θ_{12}

The constraints on the solar mixing angle θ_{12} are dominated by a combination of data from solar neutrino experiments (e.g. SNO [21] and Super Kamiokande [33]) with data from the KamLAND experiment [24]. The current constraint,

$$\sin^2(\theta_{12}) = 0.297\ ^{+0.017}_{-0.016}, \tag{2.28}$$

comes from a three neutrino fit to the solar and KamLAND data [34].

Δm^2_{21}

The best measurement of Δm^2_{21} comes from the same combined fit to the solar neutrino and KamLAND data [34]. The measured value is

$$\Delta m^2_{21} = (7.37 \ ^{+0.17}_{-0.16}) \times 10^{-5} \ \text{eV}^2. \tag{2.29}$$

θ_{23} and Δm^2_{32}

There is a strong correlation between θ_{23} and Δm^2_{32} and therefore their measurements are usually presented as a two–dimensional contour. Figure 2.6 shows a comparison of the world leading contours for $\sin^2(\theta_{23})$–Δm^2_{32}, with the tightest error bands coming from long baseline accelerator experiments such as T2K, MINOS, and NOνA [35–37]. The results are dependent on the neutrino mass ordering, based on a global three neutrino oscillation analysis [34],

$$|\Delta m^2_{32}| = (2.46 \ ^{+0.04}_{-0.04}) \times 10^{-3} \ \text{eV}^2 \quad \text{(NO)}$$
$$= (2.50 \ ^{+0.05}_{-0.04}) \times 10^{-3} \ \text{eV}^2 \quad \text{(IO)}, \tag{2.30}$$

and

$$\sin^2(\theta_{23}) = 0.437 \ ^{+0.033}_{-0.020} \quad \text{(NO)}$$
$$= 0.569 \ ^{+0.028}_{-0.051} \quad \text{(IO)}. \tag{2.31}$$

θ_{13}

Reactor neutrino experiments such as Daya Bay [38], Double Chooz [39], and RENO [40] have made the most precise measurements of θ_{13}. A three neutrino global fit to the reactor data gives [34]

$$\sin^2 \theta_{13} = (2.15 \pm 0.07) \times 10^{-2}. \tag{2.32}$$
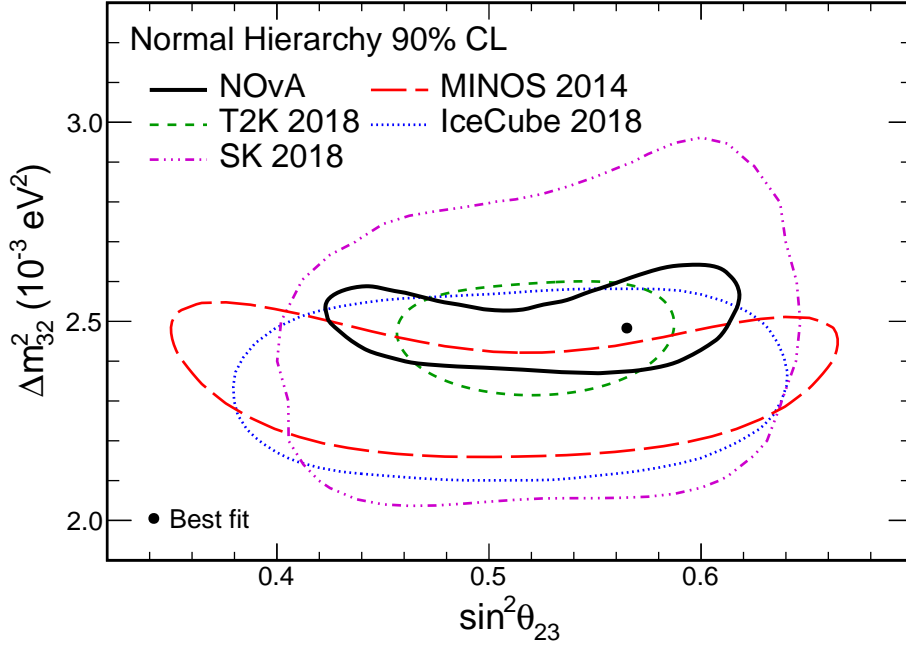
Figure 2.6: The 90% confidence region contours for $\sin^2(\theta_{23})$–Δm^2_{32} from a number of the leading neutrino oscillation experiments [35–37]. The best fit point for the NOνA experiment is shown as a black dot. [37]

δ_{CP}

While there are no accurate measurements of δ_{CP} there are some hints that it may be none–zero from long baseline accelerator neutrino experiments T2K and NOνA.

The T2K experiment's joint fit to electron neutrino appearance and anti–electron neutrino appearance shows an excess of electron neutrino events and a deficit of anti–electron neutrino events when compared to the predictions for $\delta_{CP} = 0$. This results in a preference for negative values of δ_{CP} with a 3σ confidence interval of $[-3.41, -0.03]$ in the case of normal neutrino mass ordering. The results of the T2K fit are shown in Fig. 2.7. [41]

The NOνA experiment has also performed joint fits to neutrino and anti–neutrino oscillation data, the results of the fit are shown in Fig. 2.8. As with T2K the normal mass ordering is preferred, however for NOνA the full range of δ_{CP} is covered at 3σ highlighting the need for further study of CP–violation in neutrino oscillations [37].
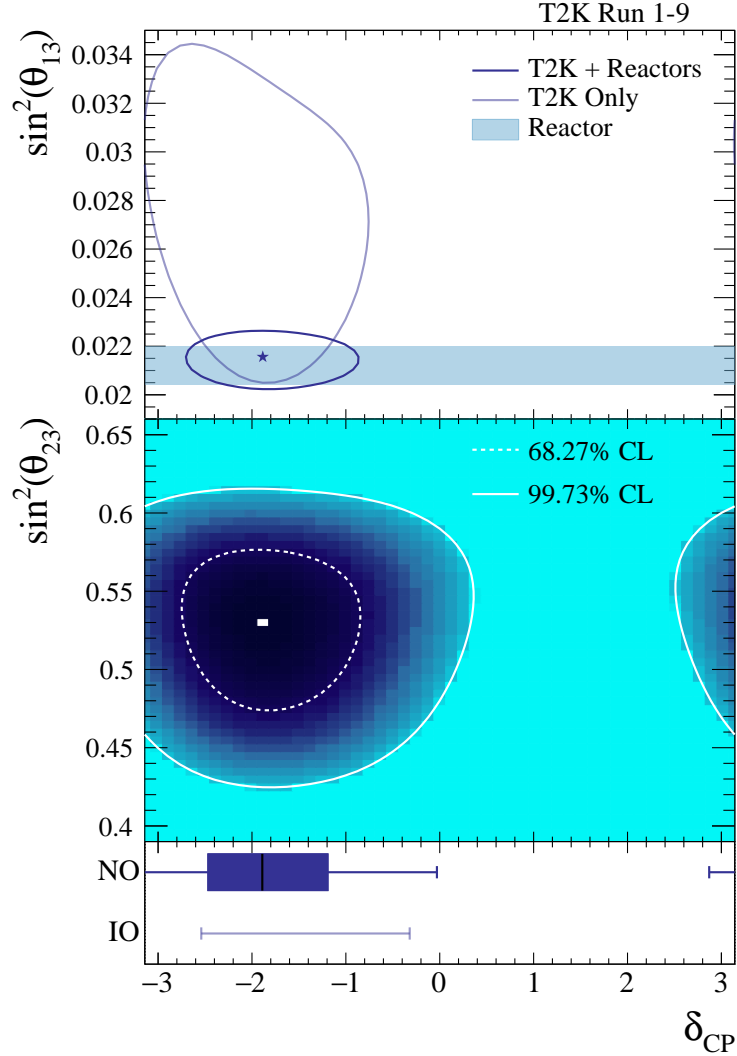
Figure 2.7: Confidence intervals for δ_{CP} from the T2K experiment [41]. Top: 68.27% confidence level contours for δ_{CP} versus $\sin^2\theta_{13}$ under the assumption of normal ordering. Middle : Confidence intervals at the 68.27% and 99.73% confidence level for δ_{CP} versus $sin^2\theta_{23}$ from a fit to T2K and reactor data under the assumption of normal ordering. Bottom: Confidence intervals for δ_{CP} from a fit to T2K and reactor data for both the normal and inverted orderings. The vertical line in the shaded box shows the best-fit value of δ_{CP}, the shaded box shows the 68.27% confidence interval, and the error bar shows the 99.73% confidence interval.
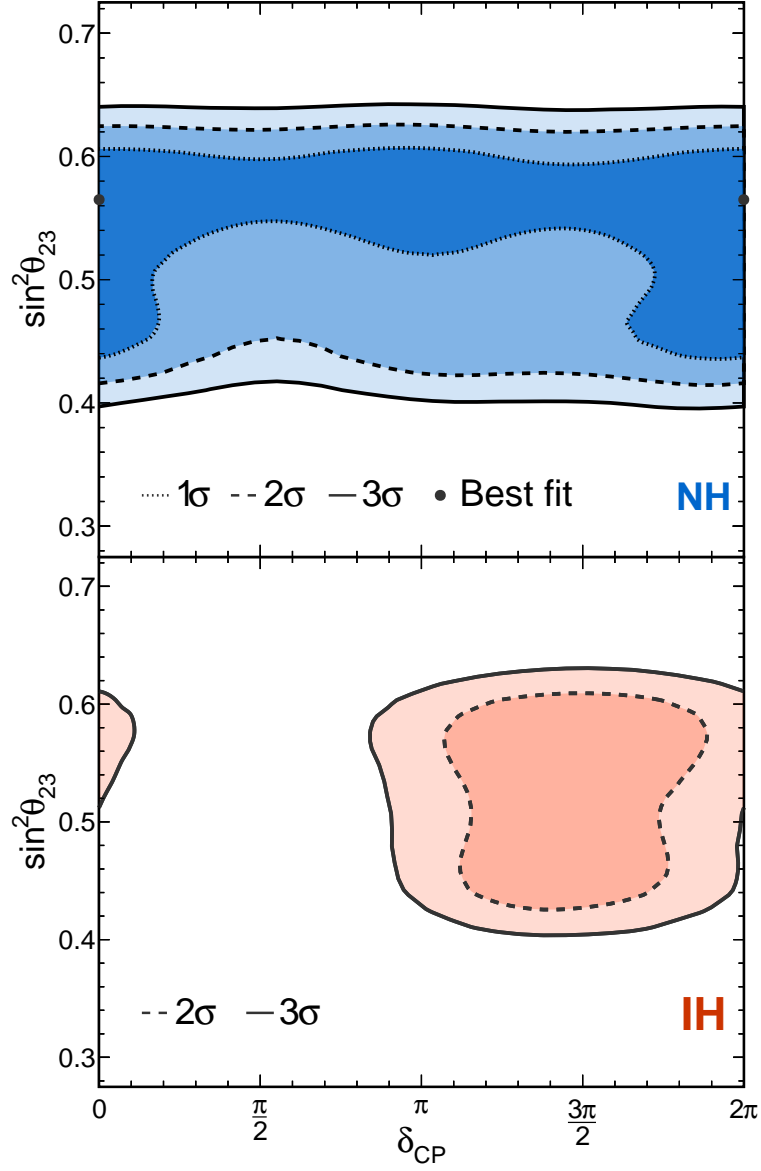
Figure 2.8: Confidence intervals for δ_{CP} from the NOνA experiment [37].
Top: Confidence interval for δ_{CP} versus $\sin^2 \theta_{23}$ under the assumption of normal ordering.
Bottom: Confidence interval for δ_{CP} versus $\sin^2 \theta_{23}$ under the assumption of inverted ordering.

2.4 Neutrino Interactions

To perform a neutrino oscillation experiment the composition of the beam needs to be measured, and the change in beam composition as a function of energy and distance travelled is analysed. In practice, this relies on measuring neutrino events and categorising them by flavour in order to compare the measurement to prediction. However, because we only see the neutrinos that interact, we are actually seeing the results of a convolution of the neutrino beam composition with the neutrino interaction cross section. Therefore, it is important to understand neutrino interaction cross sections to make accurate oscillation predictions.

Broadly speaking there are two major types of neutrino interactions: charged–current (CC) and neutral–current (NC). Only CC interactions are used in oscillation experiments because they are the only type of interaction which allows the initial flavour of the neutrino to be determined. Some NC interactions, e.g. scattering from an electron, produce high energy leptons in the detector and, therefore, form an irreducible background which must be modelled as part of the experiments simulation.

The types of charged–current interactions available are further split into three main categories.

Quasi–elastic (QE)

A neutrino elastically scatters of an individual nucleon liberating it from the nucleus.

Resonance (RES)

A neutrino excites the target nucleon into a resonance which then decays resulting in the possibility of mesons in the final state.

Deep Inelastic Scattering (DIS)

The neutrino has enough energy to resolve the individual quarks within the target nucleon, liberating the quark and resulting in a hadronic shower in the final state.

The cross sections for these processes vary as a function of neutrino energy, and they are each dominant in different energy regimes. Predictions and measurements
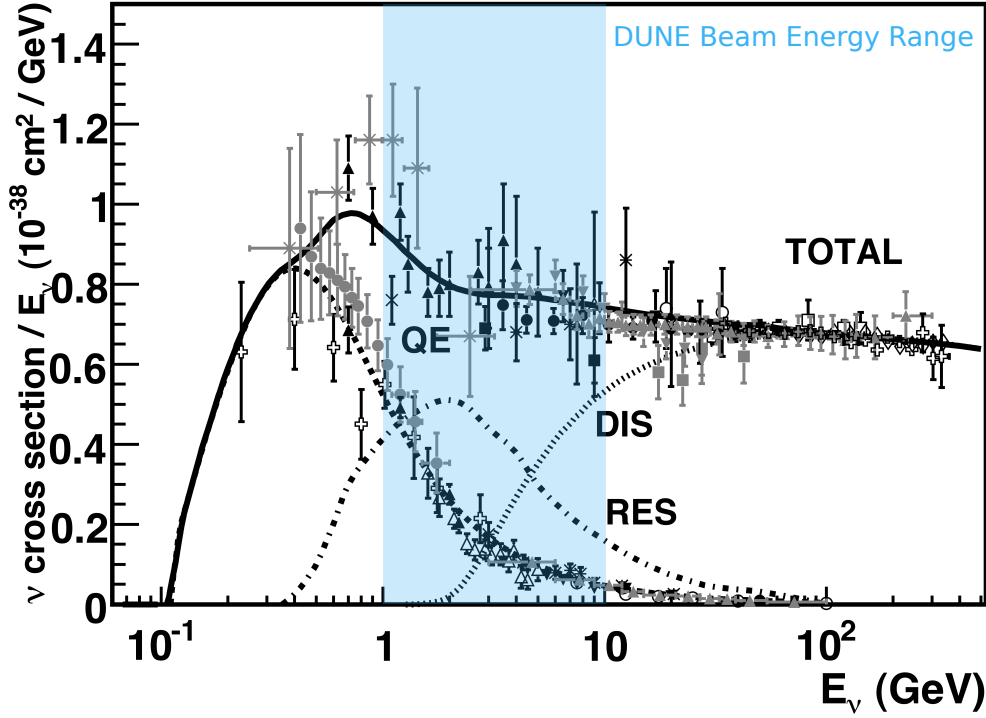
Figure 2.9: Muon neutrino cross section as a function of energy. Original figure from [42].

of the charged–current cross section for ν_μ are shown in Figure 2.9, the three main components of the cross section are shown and the energy range relevant for DUNE is highlighted [42]. Within the energy range of the DUNE beam all three of the major neutrino cross section components have a region in which they dominate, this means that understanding each of these cross sections is crucial for any neutrino oscillation measurement in DUNE.

The array of interaction modes available in DUNE means that there is a wide array particles which can be produced in the final state, and understanding the composition of the final state provides valuable input to the neutrino oscillation analysis. Part of this thesis, Chapter 5, looks at the identification of charge deposits within liquid argon TPCs. The results provide input in the analysis of ProtoDUNE–SP data, and the methods used could be adapted and developed for application in the identification of neutrino interaction modes in DUNE.

2.5 Supernova Neutrinos

Supernovae are extremely violent explosions which are undergone by certain types of stars at the end of their life. These explosions can emit one the order of 10^{53} erg of energy, and in certain cases, known as core–collapse supernovae, about 99% of this energy is carried away by neutrinos. Measurements of these neutrinos can provide insight into the mechanism involved in supernova bursts, as well as the study of neutrino masses [27].

2.5.1 Core–collapse Supernova Dynamics

Core–collapse supernovae occur in stars with masses of around 10–60 solar masses. These stars will have undergone all stages of nuclear fusion during their life, but since iron is the most tightly bond nucleus there is no fuel left to burn after it has been produced. At this stage the iron core of the star, which has a mass of around 1 solar mass, begins to collapse as the pressure produced by nuclear fusion is no longer enough to counter the force of gravity.

During the collapse of the core electron neutrinos are produced through electron capture on both nuclei and free protons.

$$e^- + N(Z, A) \rightarrow N(Z - 1, A) + \nu_e \tag{2.33}$$

$$e^- + p \rightarrow n + \nu_e \tag{2.34}$$

At first, the mean free path of these neutrinos is much longer than the size of the core and the neutrinos leave the core carrying away their energy. This phase of the collapse is known as the infall phase, it lasts on the order of 10ms and releases neutrinos with energies of around 12–16 MeV.

Once the density of the core increases beyond around $3 \times 10^{11} \mathrm{g}\ \mathrm{cm}^{-3}$ neutrinos become trapped in the core, as the cross section for coherent scattering becomes large enough to prevent neutrinos from passing through the core. Neutrinos are still being produced by capture processes at this point, but they are unable to leave the core.

The core–collapse comes to a sudden halt about 1 second after it began when the density of the inner core reaches that of nuclear matter. At this stage, the

core settles into equilibrium as a proto–neutron star while a shock–wave caused by this sudden halt propagates out through the layers of the star. Behind the shock, neutrino production is accelerated as nuclei are dissociated and the free protons capture electrons. Neutrinos begin to build–up behind the opaque shock. A few milliseconds after the bounce, the shock reaches a region of low enough density and becomes transparent, releasing the build–up of neutrinos in just a few milliseconds, this is known as the neutronisation burst.

One aspect of supernova dynamics which is still under debate is the so–called revival of the shock. As the shock dissipates through nucleon dissociation and neutrino emission it becomes weakened and eventually stalls around 100 ms after the initial bounce. At this time, known as the accretion phase, matter falls onto the collapsed core. If the shock cannot be revived a supernova will not occur. It is thought that neutrino flux produced in the proto–neutron star is able to revive the shock but the precise mechanics of this revival are still under debate. Studies have shown that the impact of spherically asymmetries might play an important role in allowing the burst to take place [43].

After the neutronisation burst the main remaining source of neutrino production comes from the proto–neutron star. Neutrinos of all flavours are produced in the core at a temperature of around 40 MeV. The release of neutrinos at this stage, known as the neutrino cooling phase, is significantly slower than that of the neutronisation burst and can last tens of seconds. During this phase, much like photons within a star, the neutrinos are mostly contained within the opaque environment of the proto–neutron star. They can only escape if they travel far enough from the core to a region where the opacity is sufficiently low. This region is called the neutrinosphere, it is different for neutrinos of different flavours, and for neutrinos and anti–neutrinos. The difference in the neutrinosphere for each flavour result in different energy distributions for each neutrino type, owing to the relative

temperature of the star at the radius of the neutrinosphere,

$$\langle E_{\nu_e} \rangle \approx 10 \text{MeV} \tag{2.35}$$

$$\langle E_{\overline{\nu_e}} \rangle \approx 15 \text{MeV} \tag{2.36}$$

$$\langle E_{\nu_x} \rangle \approx 20 \text{MeV} \tag{2.37}$$

where $\nu_x \in [\nu_\mu, \overline{\nu_\mu}, \nu_\tau, \overline{\nu_\tau}]$.

2.5.2 SN1987A

The first, and only, experimental observation of neutrinos from a supernova burst occurred in 1987. A small number of low–energy neutrino events where detected in coincidence with a supernova burst from the Large Magellanic Cloud, referred to as SN1987A. Three neutrino detectors reported an excess of low energy events in coincidence with the supernova: Kamiokande–II, IMB, and Baksan. These events are primarily produced by two types of interaction, inverse beta decay (IBD),

$$n + \nu_e \rightarrow p + e^+, \tag{2.38}$$

and elastic scattering,

$$\nu_e + e^- \rightarrow \nu_e + e^-. \tag{2.39}$$

For supernova neutrinos, the inverse beta decay cross section is significantly higher than that of elastic scattering, therefore, most events are likely to be due to inverse beta decay.

2.5.2.1 Kamiokande–II

Kamiokande–II was a water Cerenkov detector containing 2.1 kt of water. A significant increase in the rate of electron events with respect to background was observed in a 10 second window which is coincident with SN1987A [44]. Around 12 events were observed, their time sequence and amplitudes are shown in Figure 2.10. Unfortunately, due to an inaccurate detector clock, the absolute time of these events is only accurate to about one minute and therefore a time coincidence check with the other neutrino observations cannot be made.
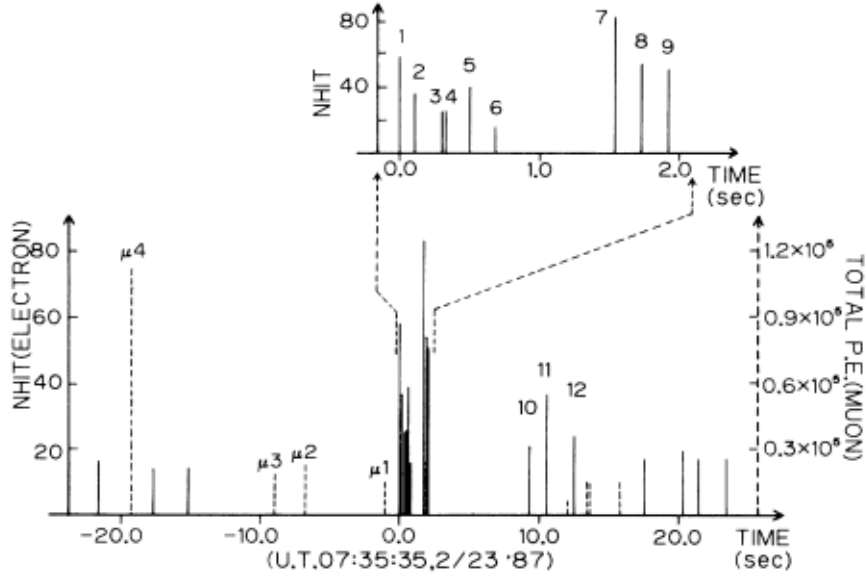
Figure 2.10: Measured supernova neutrino events from SN1987A in Kamiokande–II. Figure from [44].

2.5.2.2   IMB

IMB was another water Cerekov detector, with a fiducial mass of 3.3 kt. They observed eight neutrino candidate events with energies in the range of 20–40 MeV within a six second window, the background rate was estimated to be around 2 events per day [45].

2.5.2.3   Baksan

Unlike Kamiokande–II and IMB, the Baksan detector was a segmented liquid scintillator detector with a total mass of around 330 tons, however only a limited fiducial mass of around 200 tons was used for the supernova neutrino measurements. No excess above background could be observed by Baksan in isolation, however, when assisted by input from Kamiokande–II and IMB, a cluster of 5 events within a 10s window was observed which coincided with the measurements from IMB [46].

Since SN1987A significant progress has been made for both experimental and theoretical aspects of neutrino physics. Progress has been made in modelling supernova explosions, and the impact of neutrino oscillations on the supernova environment have been considered [47]. The current and next generation of neutrino

experiments expect to measure thousands of neutrino events for a galactic supernova instead of tens, this data could provide insights into the dynamics of supernovae as well as neutrino physics.

2.5.3 Supernova Neutrino Prospects in DUNE

The current world leading supernova neutrino detector is Super–Kamiokande which expects to measure around 8000 events for a supernova at 10 kpc [48]. As with Kamiokande–II, these events would primarily be produced via inverse beta decay interactions on the protons within the water. As such Super–Kamiokande is mostly sensitive to the $\overline{\nu}_e$ component of the supernova neutrino flux. This is common amongst all water Cerenkov and scintillator based detectors, and therefore the majority of the current landscape of supernova neutrino detectors. The large charged–current cross section for ν_e on argon therefore makes DUNE a highly complementary detector to the other major supernova neutrino detectors, and DUNE offers a unique sensitivity to the neutronisation burst which is primarily made up of ν_e.

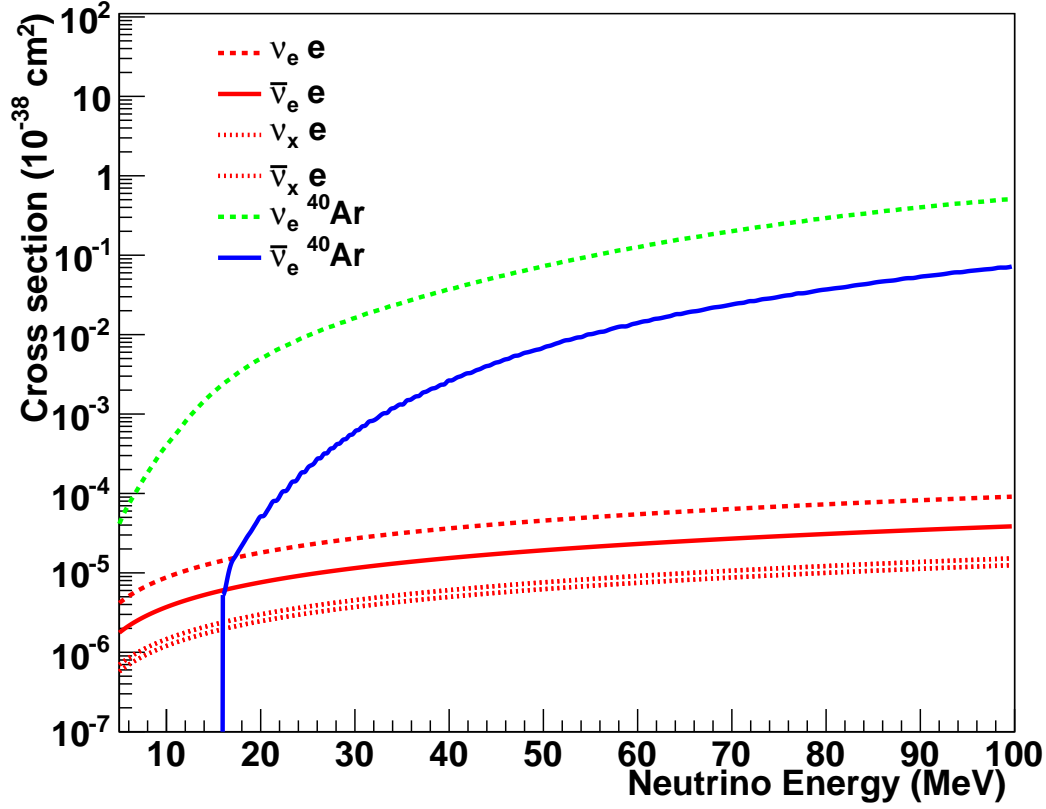#### 2.5.3.1 Supernova Neutrino Interactions in Liquid Argon

Liquid argon should bring a strong sensitivity to the ν_e component of a supernova neutrino burst, via the charged–current absorption of ν_e on ^{40}Ar,

$$\nu_e +^{40} \mathrm{Ar} \rightarrow e^- +^{40} \mathrm{K}^*. \tag{2.40}$$

This interaction leaves an e^- and an excited K in the final state. In addition there are charged–current $\overline{\nu}_e$ interactions with argon, and elastic scattering interactions with electrons which are available to neutrinos of all flavours. The dominant cross sections in liquid argon as a function of energy are shown in Figure 2.11 [49].

2.5.3.2 Supernova Neutrino Events in DUNE

For a 10 kpc supernova DUNE expects to observe roughly 3000 neutrino events, over a period of around 10 seconds. In DUNE this will show up as a sudden increase in the rate of low–energy electron events in the detector. Figure 2.12 shows the predicted time structure and energy spectrum for a simulated supernova event in DUNE [49].

Figure 2.11: Supernova neutrino cross sections in liquid argon. Figure from [49].

The details of the rate and energy of these events as a function of time can hold potential insights into both neutrino physics and the dynamics of supernova bursts.

Detecting and reconstructing tens of MeV electrons from supernova neutrinos is necessary to study supernova neutrinos, as can be seen from the observed energy spectrum for supernova neutrinos in Figure **??**. There are significant challenges involved in this measurement from the detection of low energy activity, as well as the impacts of the ionisation geometry of tens of MeV on reconstruction. Effectively reconstructing electrons in the tens of MeV range is essential to improving our understanding of supernova neutrinos in DUNE. This is one of the subjects of this thesis, and is discussed in chapter 6 using the case of Michel electrons in ProtoDUNE–SP to benchmark the performance of low energy electron reconstruction in liquid argon time projection chambers.
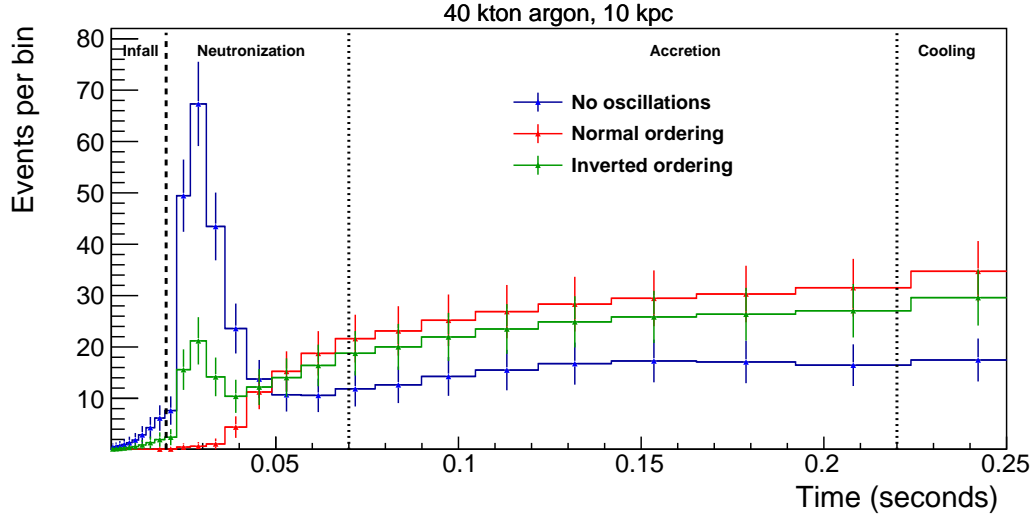
(a) Observed event rate. Figure from [49].
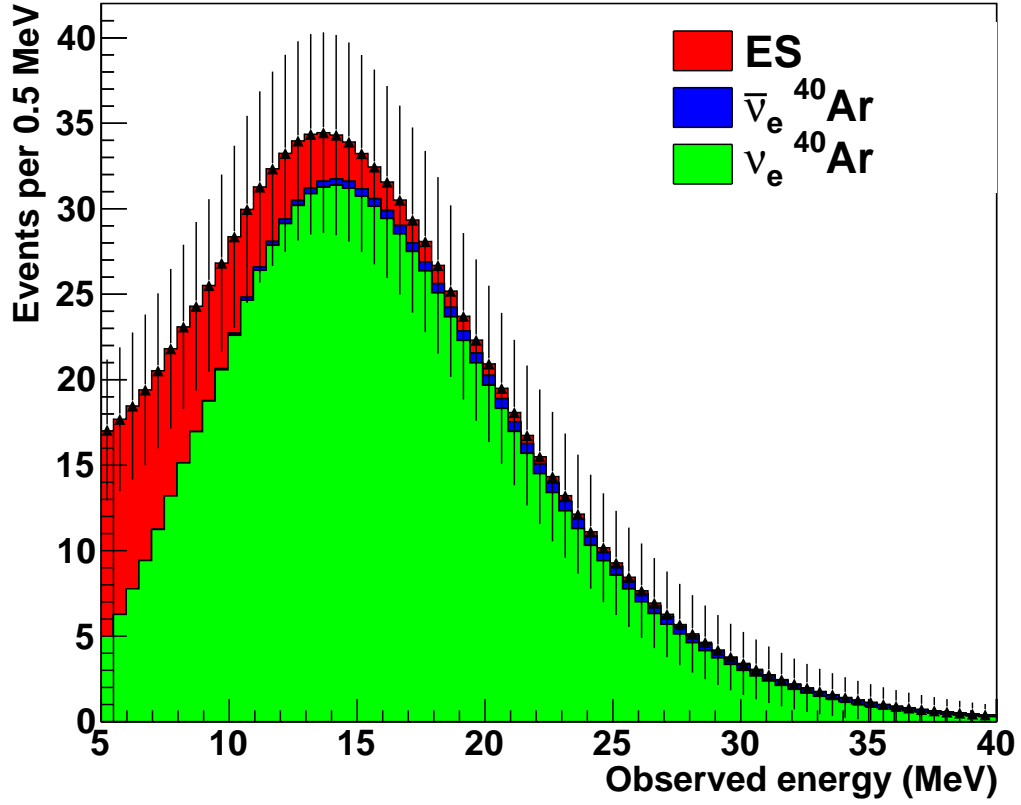
(b) Observed energy. Figure from [50].

Figure 2.12: Supernova neutrinos predictions for a 10kpc supernova in DUNE.

3

The ProtoDUNE–SP Experiment

Contents

ProtoDUNE–SP is one of two prototypes for the DUNE far detector modules that has been operating at the Neutrino Platform at CERN since the summer of 2018. The experiment collected data from a charged particle beam for approximately 3 months before Long Shutdown 2 of the Large Hadron Collider. Since then a programme of cosmic ray data collection has been ongoing.

This chapter will outline the technical details of the ProtoDUNE–SP experiment. Section 3.1 will outline the role of ProtoDUNE–SP in the context of the DUNE
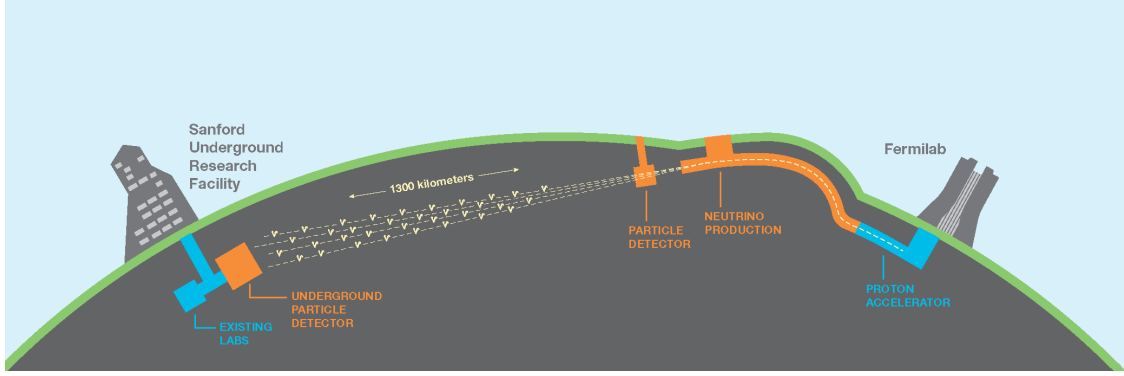
Figure 3.1: The Deep Underground Neutrino Experiment. Figure from [**TODO**].

experiment. This will be followed by a discussion of the main elements of the experiment, the ProtoDUNE–SP detector systems and the H4 beam line, in Sections 3.2 and 3.3 respectively. The high event rate in ProtoDUNE–SP is dominated by a high flux of comsic rays which will be discussed in Section 3.4. Section 3.5 will then discuss the simulation and reconstruction of ProtoDUNE–SP data. Finally Section 3.6 will cover details of the online monitoring system in ProtoDUNE–SP; as the primary developer and expert on the ProtoDUNE–SP online monitoring system during my time at CERN, the development and maintenance of this system represent a significant body of work over 12 months.

3.1 The DUNE Experiment and ProtoDUNE–SP

The DUNE experiment will be a next generation neutrino physics and nucleon decay experiment consisting of three principal components; an intense broad band neutrino beam and precise near detector based at the Fermilab National Accelerator Laboratory near Chicago, and a far detector at Sanford Underground Research Facility in South Dakota, approximately 1300 km away from the neutrino source, as demonstrated in Figure 3.1. The DUNE experiment identifies three primary scientific goals [49]:

- Perform a comprehensive programme of neutrino oscillation measurements including measurements of δ_{CP}, neutrino mass ordering, and the θ_{23} octant.

- Search for proton decay in several decay modes.

- Measure ν_e from a core–collapse supernova if one occurs within our galaxy during the lifetime of the experiment.

In addition, the experiment hopes to fulfill a significant programme of secondary science goals:

- Other accelerator based neutrino physics, such as non–standard interactions, sterile neutrinos, and CPT violation.

- Measurements of neutrino properties using atmospheric neutrinos.

- Dark matter searches in both the near and far detectors.

- A programme of neutrino interaction physics studies in the DUNE near detector.

To achieve these goals DUNE has opted to base the near and far detector designs on the liquid argon time projection chamber (LArTPC) technology. The DUNE far detector will consist of four LArTPC detectors each with 10 kt of active liquid argon mass. This technology will have never before been used on this scale, and therefore, there has been a significant programme of LArTPC research and development ongoing to validate and characterise the performance of the technology for DUNE.

3.1.1 Liquid Argon Time Projection Chambers

A LArTPC consists of a large volume of highly–purified liquid argon immersed in an electric field. Charged particles traversing the liquid argon produce two primary energy depositions, a trail of ionisation electrons along their path, and prompt ultra–violet scintillation photons. After deposition the ionisation electrons drift in the electric field toward the charge readout plane where they induce electrical signals. Liquid argon is transparent to its own scintillation light and therefore the scintillation photons can travel through the argon to be collected in a photon detection system.The LArTPC detection principal is illustrated in Figure 3.2.

The details of the charge readout and photon detection systems are specific to each detector, but broadly speaking LArTPC detectors can be split into two main
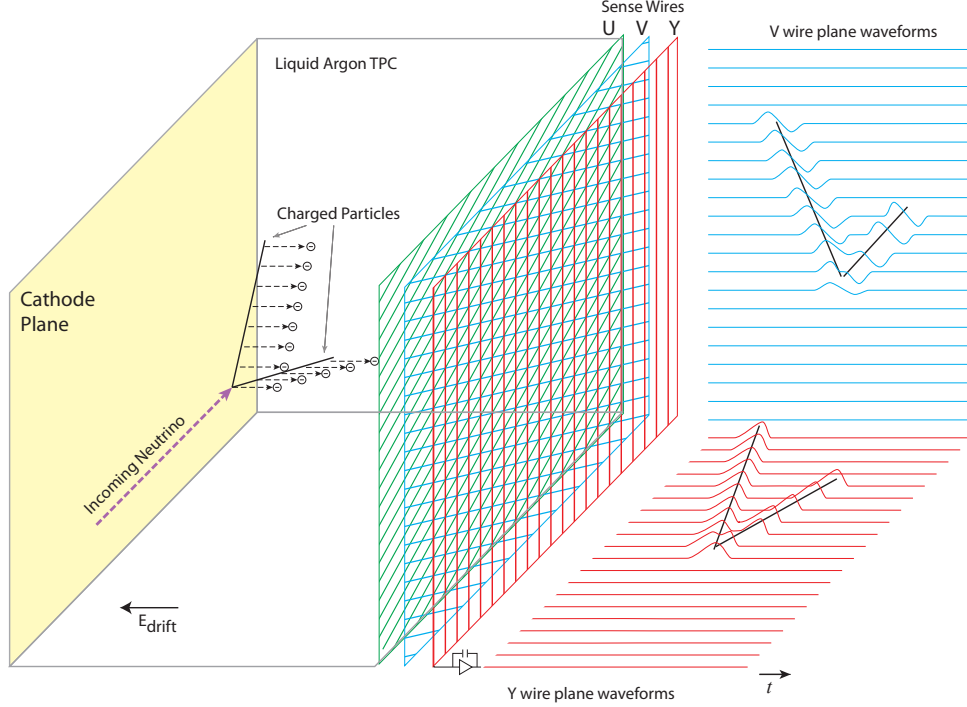
Figure 3.2: LArTPC detection principal. Figure from [5].

categories: single–phase and dual–phase. In a single–phase detector the drifting ionisation electrons remain in the liquid argon and the signals are typically read out on three anode wire planes. A dual–phase LArTPC contains an additional region of gaseous argon in which a high electric field, known as the extraction field, is applied to extract the ionisation from the liquid before it is amplified and collected on a pair of anode wire planes [51].

ProtoDUNE–SP is one of two large scale prototypes for the DUNE far detector modules, which focusses on the single–phase LArTPC technology. The DUNE far detector modules feature a modular design in which each module is built up of a number of identical components, ProtoDUNE–SP was designed to prototype the design of many of these components at a 1:1 scale, including the anode planes, cathode plane, and photon detectors. The ProtoDUNE–SP experiment has four primary goals, as outlined in the Technical Design Report [52]:

- Prototype the production and installation procedures for the single–phase far detector design.

- Validate the design from the perspective of basic detector performance; this can be achieved with cosmic-ray data.

- Accumulate large samples of test-beam data to understand/calibrate the response of the detector to different particle species.

- Demonstrate the long-term operational stability of the detector as part of the risk mitigation program ahead of the construction of the first 10 kt far detector module.

As such, ProtoDUNE–SP represents a significant milestone in the development of the far detector for the DUNE experiment. Its successful operation, both in a test–beam and with cosmic rays, provides valuable data with which to understand reconstruction and analysis of the data that will be collected by the DUNE far detector.

3.2 The ProtoDUNE–SP Detector

The ProtoDUNE–SP detector is located at the Neutrino Platform at CERN along the H4 beamline. It is a single–phase LArTPC detector with a total liquid argon mass of 0.77 kt, making it the largest single–phase liquid argon TPC built to date. The detector is built in a modular fashion with each component representing a 1:1 prototype of the proposed DUNE far detector components. The main components, which are labelled in Figure **??**, are:

- Anode Plane Assemblies

- Cathode Plane Assemblies

- Photon detection system

- Field Cage and High Voltage Systems

- Beam Plug
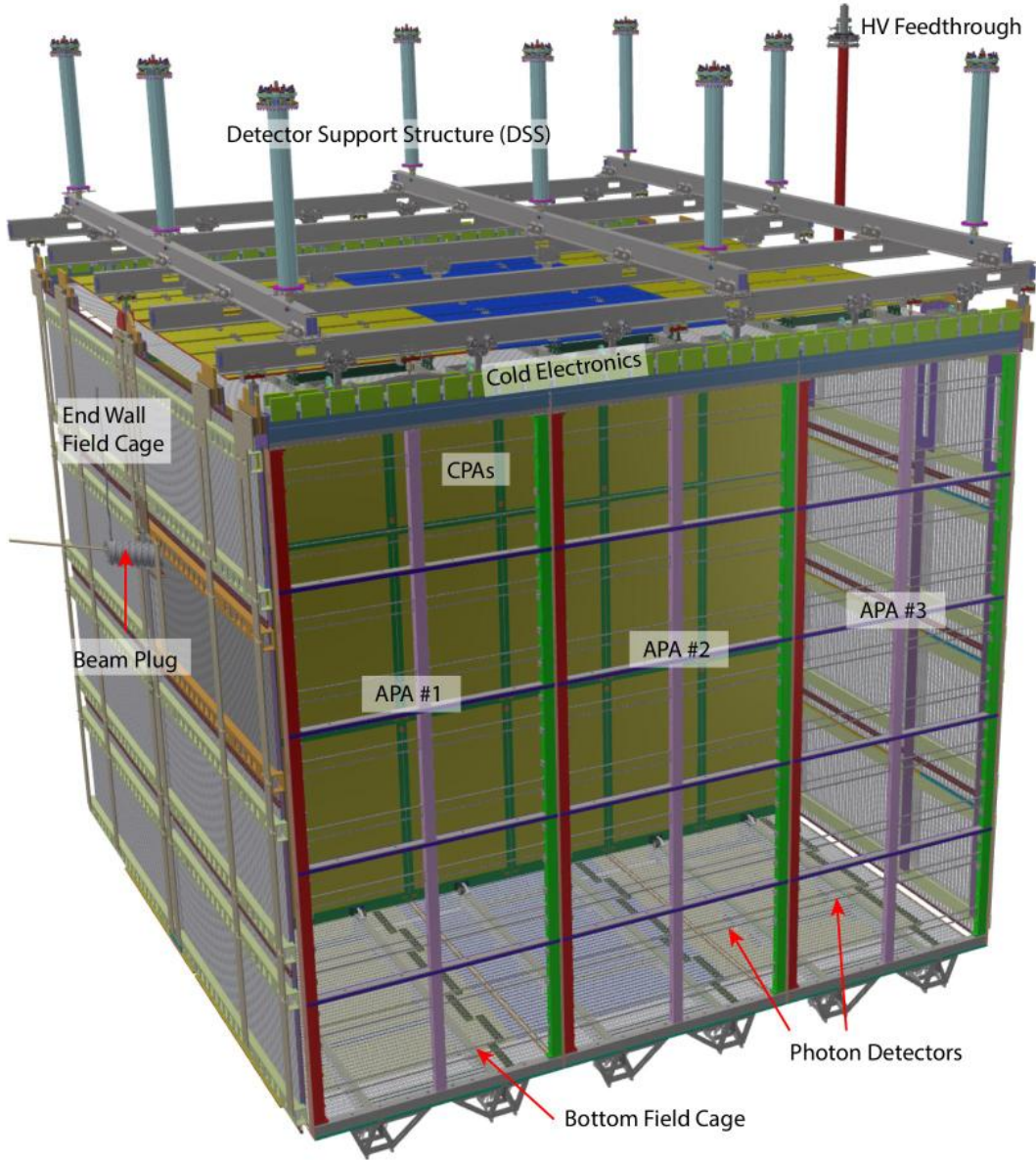
Figure 3.3: The ProtoDUNE–SP TPC. Figure from [52].

4

Energy Loss in Liquid Argon

This chapter will cover in more detail both the theory and measurement of electromagnetic energy loss in liquid argon. Energy loss for both electrons and photons will be discussed and the implications of this for electron reconstruction at different energy scales will be highlighted.

The work in this section is complete and part of this work was reported in the document submitted for transfer of status.

4.1 Electron Energy Loss

4.2 Photon Energy Loss

4.3 Electron–Ion Recombination

4.4 Implications on Electron Reconstruction in Liquid Argon

5
Charge Identification with Convolutional Neural Networks

A major problem faced by the next generation of neutrino experiments is the correct categorisation of particle interactions within the detector. Typically identifying the underlying type of a neutrino interaction involves determining the lepton content of the final state particles; as such it is important to be able to distinguish muons from electrons, or more generally tracks from showers.

This chapter will describe an approach for hit classification in LArTPCs using machine learning techniques. A brief theoretical overview of neural networks will be presented in section 5.1, including a discussion of convolutional neural networks and their application to pattern recognition. Section 5.2 will detail an approach to hit classification in LArTPCs based on tagging the source of energy depositions with a convolutional neural network. The performance of this approach will be analysed with ProtoDUNE–SP simulation and data in sections 5.3 and 5.4 respectively.

5.1   Neural Networks

An artificial neural network (ANN) consists of a set of nodes, together with a set of connections between those nodes. The nodes in the graph take the form of an artificial neuron which passes a number of inputs through a nonlinear activation

function to produce a single output. In an ANN the connections provide a mechanism for taking the output of a given node and using it as the input for a subsequent node. This structure of nodes and connections provides a very flexible framework, the basis for a number of machine learning algorithms which utilise this flexibility to learn the structure of complex data sets.

In order for an ANN to make accurate predictions based on data, the weights and biases between each set of neurons must be tuned such that the outputs of the network match those expected for a given input. In supervised learning [53], the loss, a measure of the difference between the truth and the output of an ANN, can be used to learn the appropriate values of the weights and biases using the method of gradient descent. The loss is computed and its gradient as a function of the weights and biases can be calculated with the back–propagation algorithm [54]; the loss is then minimised based on the gradient calculated with back–propagation. This process can be repeated until the loss function reaches an acceptable level or stops decreasing.

One of the most widely used ANN's is the multi–layer perceptron (MLP) [53]; this class of networks consists of at least three layers of nodes: an input layer, one or more hidden layers, and an output layer. These layers are connected in a feed–forward configuration such that the graph of nodes contains no cycle. Traditionally, the layers are also fully connected such that the output of each node is connected to the inputs of all nodes in the next layer. These networks are able to approximate any function to arbitrary precision with a single hidden layer [55]; however, there is no limit on the number of nodes required in order to achieve a good approximation. In practice networks with additional hidden layers can reach the required precision with fewer nodes than a network with a single hidden layer [56].

ANN's provide a flexible tool for a variety of pattern recognition tasks but there can be issues with their training and use. Typical issues with ANN's include a risk of slow learning due to vanishing gradients for typical sigmoid activation functions and a high risk of over–training due to the large number of free parameters. In

particular, over–training can lead to poor generalisation of the network for real world examples, despite excellent performance when evaluated on the training sample [53].

An extension of the MLP with considerable success, particularly in image classification tasks, is the convolutional neural network (CNN) [57, 58]. When evaluating data with a high dimensional input, having a fully connected network architecture leads to large numbers of neurons and high computational cost. In addition, for spatially correlated data such an architecture does not take the local spatial structure of the data into account. A CNN attempts to resolve these issues by exploiting the local connectivity of the data; single input neurons are replaced by convolutional kernels which are evaluated on small regions of the input. These convolutional kernels are evaluated over all valid locations in the input producing feature maps which describe the spatial distribution of the features which each kernel has learned to identify. Each set of feature maps can then be used as an input for either convolutional layers or fully connected layers.

Convolutional kernels provide a local translation invariant evaluation of features within the data; with this method low level features are identified first and their spatial distribution can then be exploited to identify higher level structure in the data [57]. This makes these networks ideal for pattern recognition in images, where common features can be located anywhere in the image. The high spatial and calorimetric energy resolution of LArTPC detector data make these algorithms an ideal candidate for classification of the data, and successful applications on CNNs have been achieved in ongoing neutrino experiments [59, 60]. The remainder of this chapter will detail a use of CNNs to identify low level features in LArTPC data.

5.2 Hit Identification with Convolutional Neural Networks

As well as in neutrino event classification, effective track shower separation has important applications throughout DUNE's physics programme; defining pure calibration samples such as minimum ionising muons and π_0 decays is crucial for understanding the energy response of the DUNE detector. Each of these samples

has a unique topology, but the first step in identifying many of these samples is the same: defining tracks and showers which can be combined to give the final state. To do this collections of hits have to be clustered and identified as track or shower objects. Here we will present a method for classifying the ionisation source of hits, a label is then associated with each hit, and subsequent reconstruction and analysis algorithms can use this when defining data samples.

Aside from track and shower objects, a useful calibration sample with a unique topology in LAr is the Michel electron. At typical Michel electron energies the ionisation energy loss of electrons in LAr undergoes a transition from collision dominated to radiation dominated, as such Michel electrons typically have a combined topology with a short track–like component and a few small radiated energy depositions. Due to the unique topology of these interactions, Michel electrons where chosen as a unique category for hit classification.

A CNN was used for hit classification, the network was trained to predict $\{p_t, p_s, p_e, p_m\}$, the probabilities for track, shower, empty, and Michel classifications respectively. The empty category is included to ensure that the network doesn't learn to assign a track–like or shower–like tag to empty or noisy regions of the data. Since the Michel electron category has overlap with the track and shower categories, the Michel electron probability is decoupled from the other probabilities which are constrained to sum to one.

Training data was built using simulations of the ProtoDUNE–SP detector in the LArSoft framework [61]; cosmic ray simulations were combined with simulations of the ProtoDUNE–SP beam for peak beam energies in the range 1–7 GeV and both positive and negative beam polarity. The input was formed of small patches of the raw detector readout in each plane, 48 wires in total where considered around the central energy deposition and an equal number of bins were formed in the drift time coordinate by averaging the ADC values over time such that the distance scale was equal in both coordinates. The truth for each training sample was obtained from the simulation by associating the measured ionisation energy depositions to the corresponding simulated particle. In total ~ 26 million input patches were produced,

figure 5.1 shows example patches for each label type, and details of the number of each patch type in the training, validation, and test data sets are given in table 5.1.
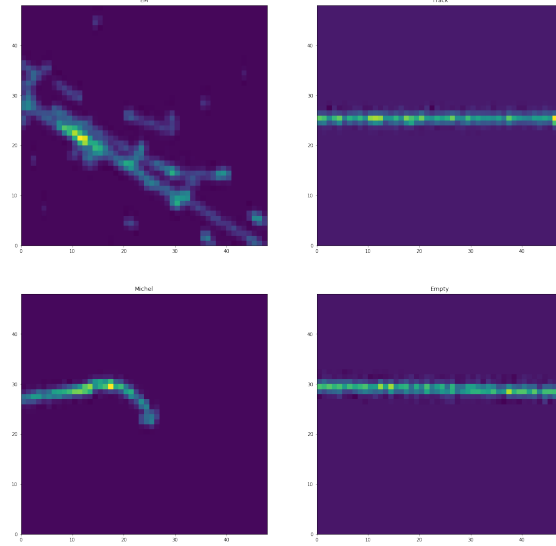
Figure 5.1: Example input patches for each label. Clockwise from top–left: Shower, Track, Empty, Michel.

| Patch Type	Shower	Track	Empty	Michel
Training	13,493,982	9,727,604	2,517,882	731,456
Validation	734,673	562,038	141,388	42,727
Test	764,659	518,805	139,987	39,674

Table 5.1: Summary of the number of samples with each truth label in the training, test, and validation data sets.

The network architecture was designed to provide the best performance possible given constraints on running time; since the CNN is part of the low level reconstruction chain and it must run over a large number of candidate images for each event, run time for each event is required to be $O(10)$s. While better classification performance was achieved with deeper networks, the best performance while achieving the running time goal was achieved with a relatively shallow network consisting of one convolutional layer followed by two dense layers; it is reasonable to assume that with improved computational resources, e.g. evaluation with GPU's, the performance of the classification could be improved within the time constraints.

The TensorFlow library was used to design and train the CNN, with the TensorBoard visualisation suite being used to monitor training [62]. The final

network architecture used is shown in figure 5.2; the 48×48 pixel input images are passed through a single convolutional layer with 48 5×5 filters; the output feature map is passed onto a pair of dense layers with 128, and 32 nodes respectively. Leaky rectified linear units are used as activation functions throughout the hidden layers [63]. These units are more computationally efficient than sigmoid like functions as well as providing a non–vanishing gradient for all inputs, avoiding saturation in learning. The output of the network is split into two branches; a three–way softmax function is used to constrain the joint probability for track, shower, and empty to sum to one, and a sigmoid function is used for the output of the Michel electron classifier. Finally, regularisation is achieved with the dropout algorithm [64]; in each iteration of the training weights have a probability p to be set to zero while the remaining weights are scaled by a factor $1/(1-p)$. With this approach, each training iteration uses only a random sample of the available nodes and as such nodes cannot co–adapt. The resulting network is a model average of each possible sub–network.

The network was trained using stochastic gradient descent (SGD) with the total loss being the weighted sum of the losses for the two output branches, $L_{tot} = 0.1 \cdot L_{tse} + L_m$, where the Michel classifier is given higher precedence due to the smaller training data set available for the Michel output. In order to speed up the learning process and converge on an optimal model, both the momentum and decay algorithms were used; momentum reduces oscillations of the weights during learning, while the decay of the learning rate allows for rapid learning during early stages of SGD and increased precision as the model converges [53]. Learning metrics were monitored during training using TensorBoard. The losses for each branch as well as the total loss for the validation data set are given in figure 5.3 as a function of the training epoch. The validation losses remain stable giving an indication that regularisation with dropout was successful in preventing over–fitting of the training data. However, the validation set loss does not increase significantly after the first couple of epochs and so the training could have been terminated sooner with this network architecture. The final losses measured with the test data set are given in table 5.2.
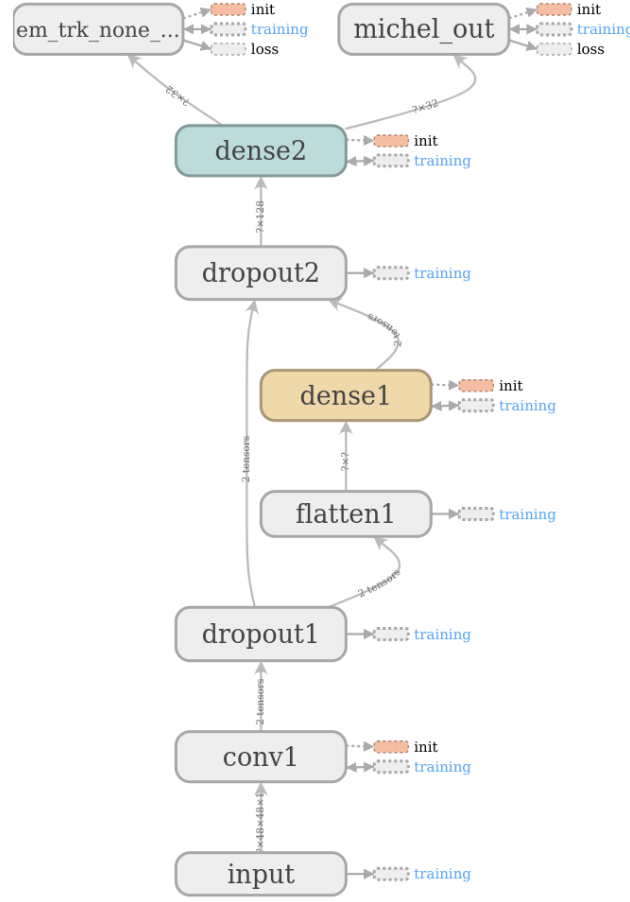
**Figure 5.2:** Network architecture used for hit classification, visualisation from the TensorBoard library.

Loss Type	L_{tot}	L_{tse}	L_m
Loss Value	0.033	0.155	0.017

Table 5.2: Test set losses after full training process.

5.3 Performance on ProtoDUNE–SP Simulation

The performance of the hit tagging was evaluated with reconstructed events in the ProtoDUNE–SP detector from the latest simulation samples; in the simulations, the detector was simulated under a number of different conditions, specifically including the space charge effect (SCE) [65] and excluding it. The hit tagging was trained on a part of the simulated data set which included the SCE and, as such, the samples
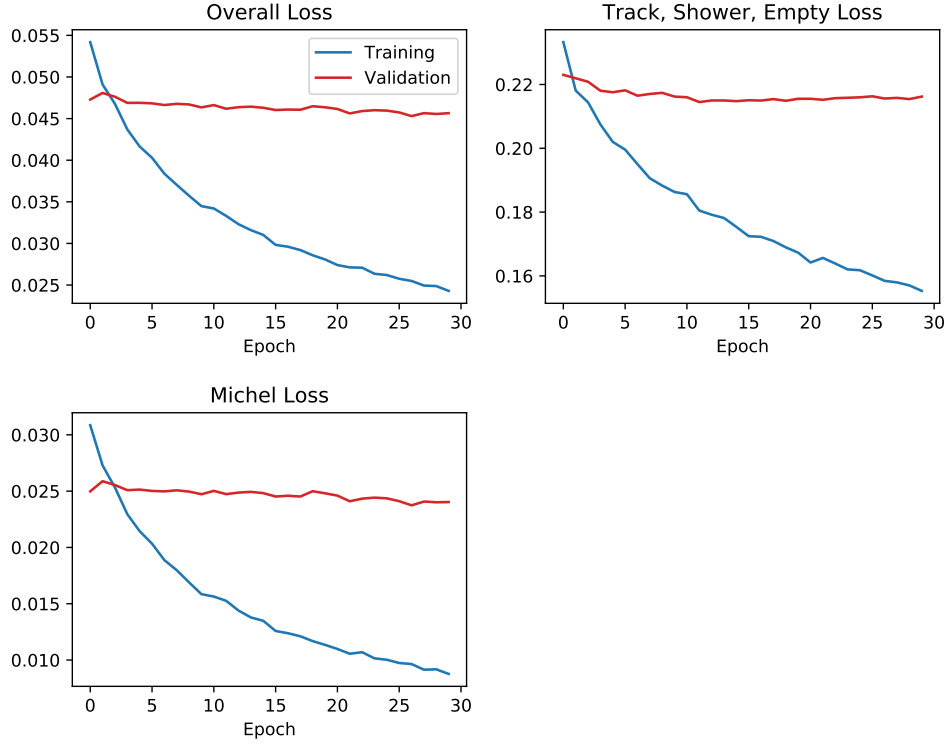
Figure 5.3: Evolution of the validation and training set losses during the training process.

without the SCE can be used as a validation that the network is robust to SCE differences between the simulations, and hence between the simulations and the data.

The distributions of the shower like classifier output for true shower hits and all other hits are given in figure 5.4; a strong separation between track and shower hits is observed. The shower classification threshold was optimised based on the F1 metric. This metric is defined as the harmonic mean of the precision and recall of a classifier and optimising with this score will ensure that both precision and recall will be high in the final classifier; for use cases where neither precision or recall is favoured, the F1 metric can be used to optimise for the best overall performance. The value of the F1 metric as a function of threshold is also shown in figure 5.4; the score peaks at a threshold of 0.72 with a value of 0.863 corresponding to a precision of 0.863 and a recall of 0.863.
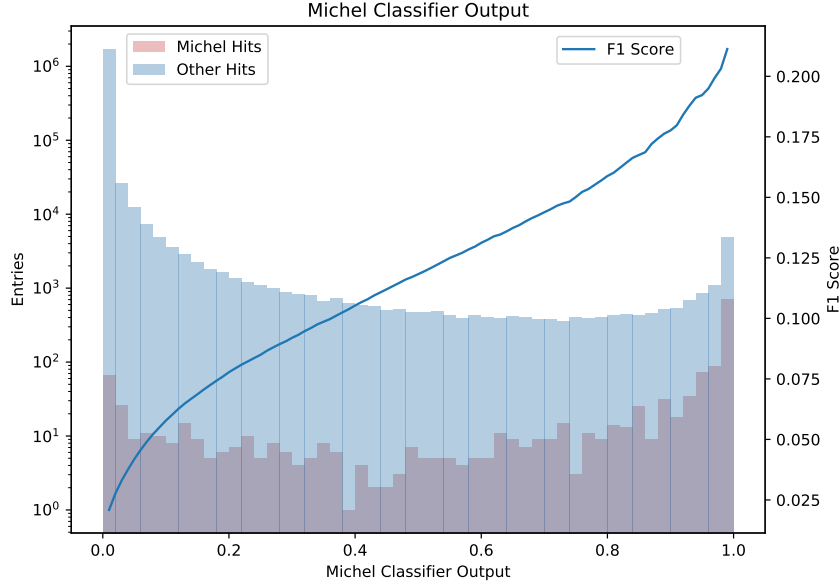
Figure 5.5 gives the distributions of the Michel classifier output for true Michel electrons and all other hits. The large difference in sample size between the Michel electron and other hits in this sample means that despite high recall by the Michel
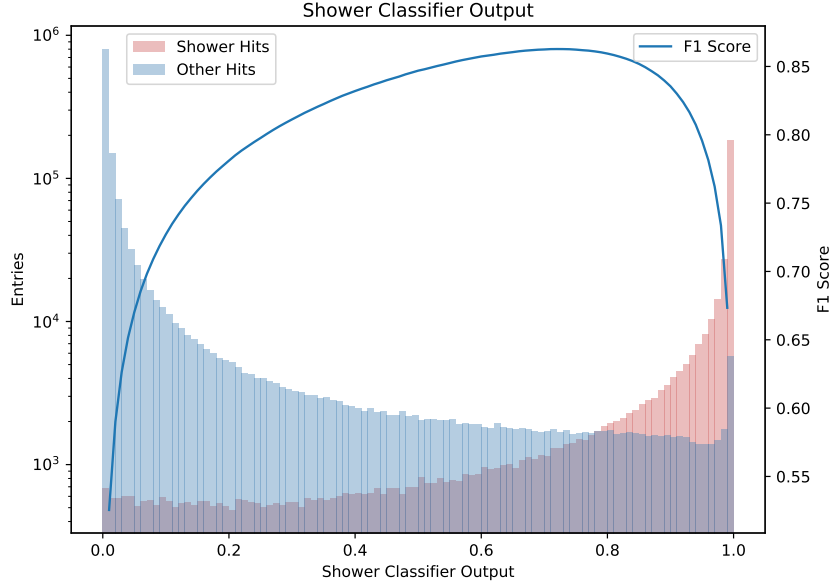
Figure 5.4: Shower classifier output distributions for true showers, and all other hits. Threshold optimisation was done using the F1 score metric which is also plotted.

electron classifier, low precision is achieved. In chapter 6 we will see that despite the low performance of the classifier for individual hits, a pure sample of Michel electron events can be selected by clustering hits with high Michel electron scores. This is due to the fact that the simple hit by hit classification test does not account for spatial correlations between Michel tagged hits.

Finally, the overall performance of each classifier was evaluated using the receiver operating characteristic (ROC) curve [66]; ROC curves are a test of the classification ability of a binary classifier. The curves show a comparison of the true positive rate and the false positive rate of the classifier as a function of the classification threshold chosen for the classifier. Figure 5.6 shows the ROC curves for the shower and Michel classifiers; the locations of these curves in the top left corner of the plots show that both have excellent performance as classifiers. In addition, the ROC curves show good agreement between the SCE on and SCE off data sets, showing that the classifiers are robust to changes in the SCE model should it differ between data and simulation. It is worth noting that the ROC curve only accounts for classification rates within each true sub–sample, it cannot account for the difference

Figure 5.5: Michel classifier output distributions for true Michel electrons, and all other hits. Threshold optimisation was initially done with the F1 score metric, the threshold was modified when combined with a clustering algorithm, see chapter 6.

in sample size between the Michel electron sample and all other hits, and thus the ROC curve is a more instructive metric for the shower classifier where the size of the true and false samples are of a similar magnitude.

5.4 Validation and Performance on ProtoDUNE–SP Data

For validation on real ProtoDUNE–SP data two approaches were used: visual validation with event scans and cross validation with the output of the Pandora reconstruction framework [67]. Data from ProtoDUNE–SP run number 5387 was used for the validation; the data for this run was taken under stable operating conditions with a peak beam energy of 1 GeV.

Hand scans of the events show qualitatively that performance on the data is good. Figure 5.7 shows an example of the track like classification of hits in a real event. We can see that for hits along the tracks the classifier produces a large output score, and for shower like activity in the event the score is low, as we expect.
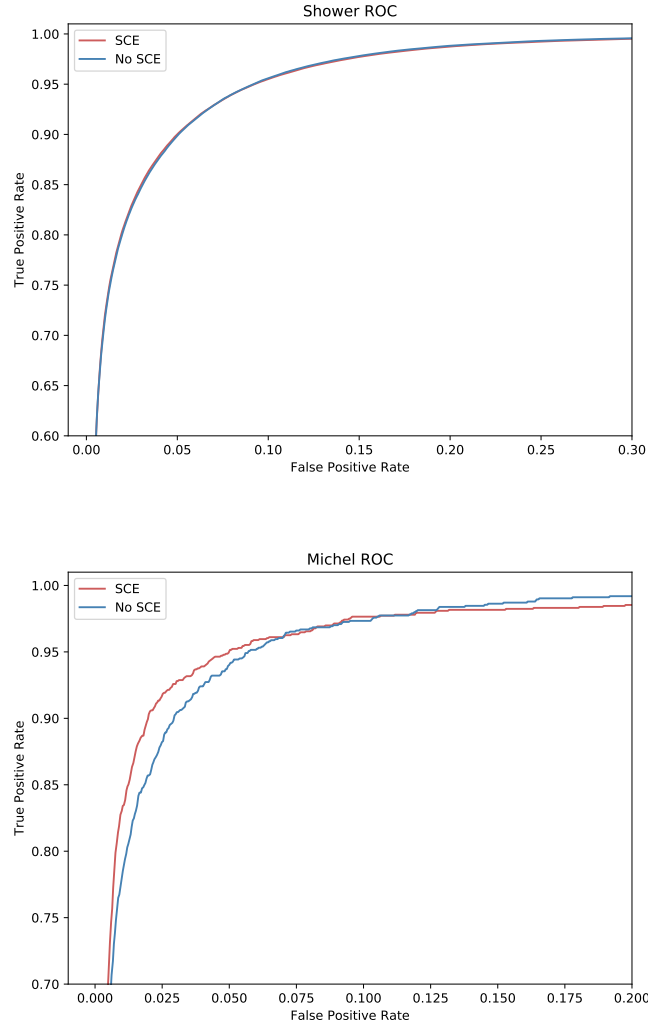
Figure 5.6: ROC curves for the shower (top), and Michel (bottom) classifiers. ROC curves for simulations including and excluding the SCE are included.

In particular the classifier is able to identify that hits which are adjacent to the track, delta rays, are from scattered electrons.

The Pandora reconstruction framework is the primary reconstruction used by the ProtoDUNE–SP experiment; for a more quantitative validation of the performance of the hit tagging algorithm, the hit tagging output can be compared to the reconstructed objects produced by Pandora. After the ProtoDUNE–SP data has been reconstructed, all of the reconstructed hits will have been clustered into either track or shower objects. As such the comparison of a hits CNN output with the type of reconstructed object it belongs to is a test of the agreement between the

CNN approach and the Pandora reconstruction algorithms. The Michel electron performance cannot be validated in this way due to a lack of tagged Michel electron objects in the Pandora output. Therefore, hand scanning of events is the primary validation of the Michel electron classifier and will be discussed in chapter 6.

The first test performed was the comparison of the CNN output distributions for hits in both Pandora tracks and Pandora showers, the corresponding distributions are given in figure 5.8 for both data and Monte Carlo; a strong correlation between the reconstructed Pandora objects and the associated CNN score can be seen in both cases, however the correlation is stronger in Monte Carlo than in data. The discrepancy between Pandora and the CNN is still being understood, differences between the data and simulations impact the performance of both algorithms. Figure 5.7 shows reconstructed hits labelled according to whether they agree or disagree with Pandora, we can see that for long tracks the agreement is good while smaller objects tend to disagree, with the CNN typically assigning a shower like classification but Pandora reconstructing them as a track. Work to understand the discrepancy between the CNN score and Pandora is ongoing.

This chapter has presented work on the development of a hit classification algorithm for LArTPCs based on CNNs; the performance of this approach for track–shower separation has been evaluated with ProtoDUNE–SP simulation and reconstruction, demonstrating good performance. This hit tagging framework is designed such that it can be utilised throughout the LArSoft reconstruction chain and is complementary to other reconstruction algorithms in the framework; chapter 6 will detail an example use of the hit tagging output: Michel electron event selection. Additional plans for this chapter are detailed below.

- Understand the difference between data and MC when comparing the CNN to Pandora.
- Test network robustness to other detector effects in simulation.
- Retrain networks with future simulations, including data driven models of detector effects.
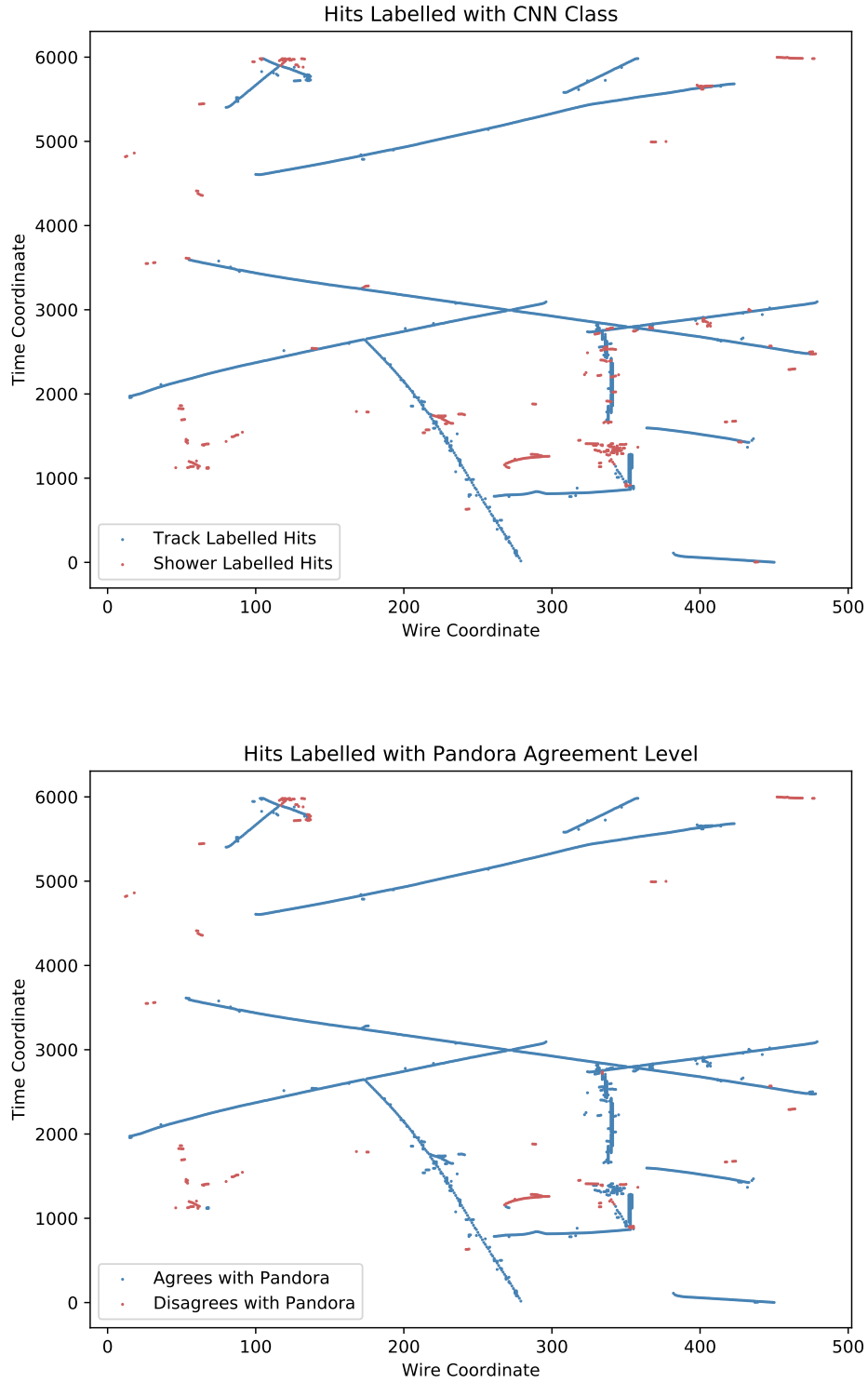
Figure 5.7: Reconstructed hits from ProtoDUNE–SP run number 5387 labelled with CNN classification (top), and Pandora agreement level (bottom).
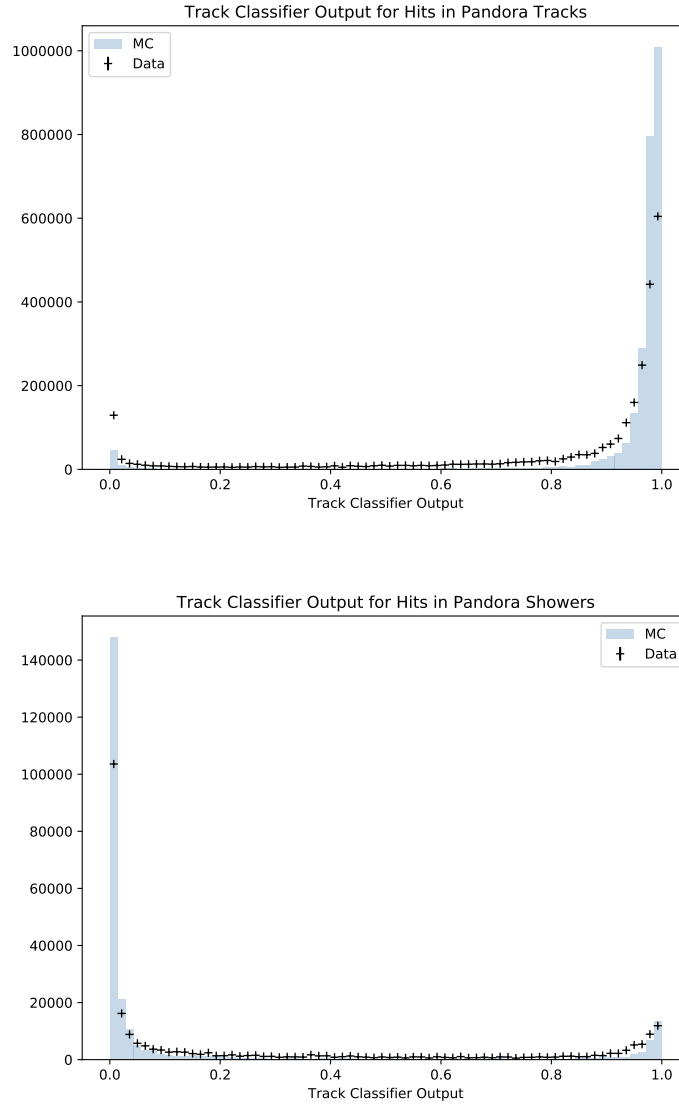
Figure 5.8: Output distributions for the track classifier on reconstructed Pandora objects.

6

Study of Michel Electrons in ProtoDUNE–SP

Contents

Studying electrons in the tens of MeV energy range can provide valuable input into reconstruction techniques and energy uncertainty for the measurement of astrophysical neutrinos from supernova bursts. Understanding the response of LArTPC detectors to electrons in this range will be important for any large scale LArTPC experiment wishing to study supernova bursts. At these energies electron interactions have large contributions from both ionisation energy loss and radiative energy loss and therefore they have a unique signature which is neither track–like or shower–like. Low–energy electrons therefore require unique reconstruction algorithms to maximise the overall reconstruction performance. This chapter will discuss an approach to low–energy electron reconstruction in LArTPC detectors based on the use of convolutional neural networks and semantic segmentation.

Michel electron events from ProtoDUNE–SP will be used to test the performance of this technique and to provide an estimate of the energy uncertainty of LArTPC detectors for low–energy electrons.

Chapter outline.

6.1   Michel Electrons in Liquid Argon

Michel electrons are produced when a muon decays at rest. This decay gives rise to a characteristic energy spectrum which has a sharp cut–off at around 50 MeV, corresponding to half the muon mass. In matter it is also possible for μ^- to be captured on nuclei before they decay, this causes a broadening of the Michel electron spectrum for these events. A comparison of the Michel electron energy spectrum for free μ^+ and captured μ^- is given in Fig. 6.1. The capture process occurs roughly 70% of the time for negative muons in liquid argon and therefore in ProtoDUNE–SP the observed energy spectrum is a combination of the two processes in roughly equal quantities.

As discussed in chapter 4, the energy loss for electrons in liquid argon passes from an ionisation dominated regime to a radiation dominated regime in the tens of MeV region. The crossover point for this transition occurs at around 45 MeV, very close to the peak of the Michel electron spectrum. This leads to a unique signature for Michel electrons in liquid argon detectors, a short ($\sim$ 5cm) track segment is surrounded by a number of small radiated energy deposits. Figure 6.2 shows an example of a Michel electron candidate from ProtoDUNE–SP data, along with labels of the key features.

One of the main challenges for Michel electron reconstruction in liquid argon is to successfully associate the radiated energy depositions back to the initial Michel electron once they have produced ionisation in the detector. Photons have a radiation length of around 20–30 cm in liquid argon which is many times larger than the size of the typical track–like part of the event, around 5 cm. Fig. 6.3a shows the spectrum of radiated photons from Michel electron events in ProtoDUNE–SP simulation alongside the photon multiplicity as a function of Michel electron

"figures/""michel_spectra".pdf
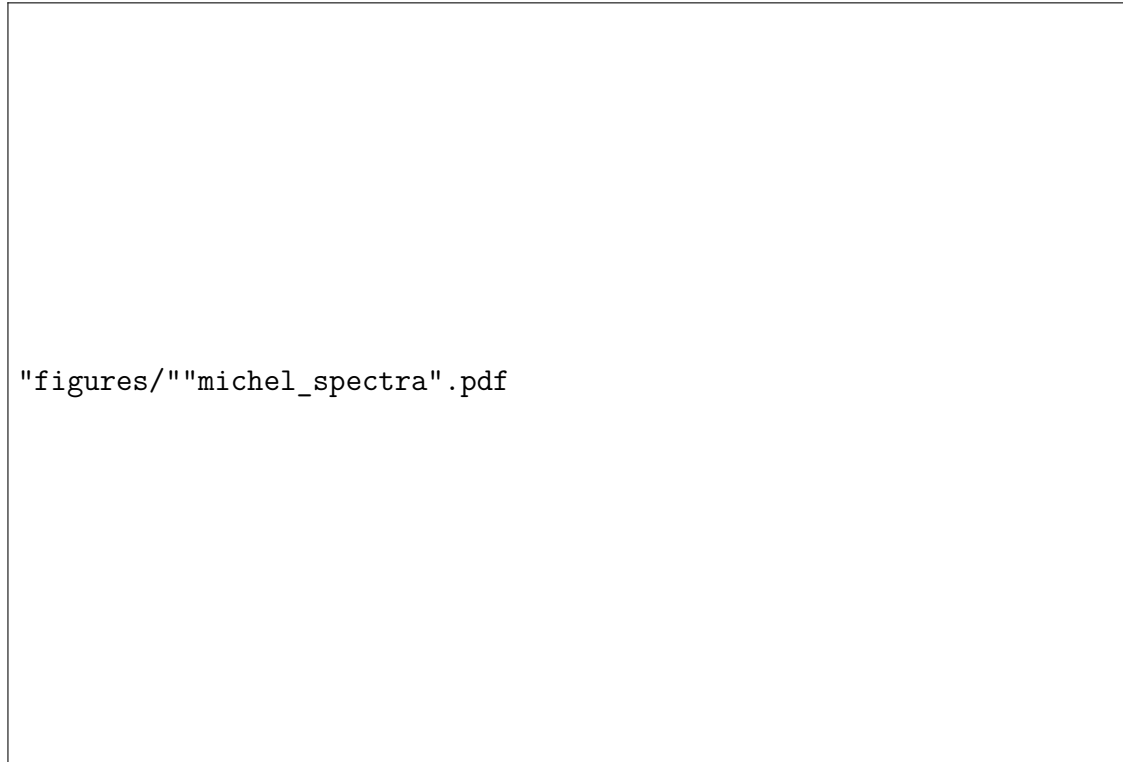
Figure 6.1: Michel electron energy spectra in liquid argon. (a) free muons. (b) muon capture at rest.
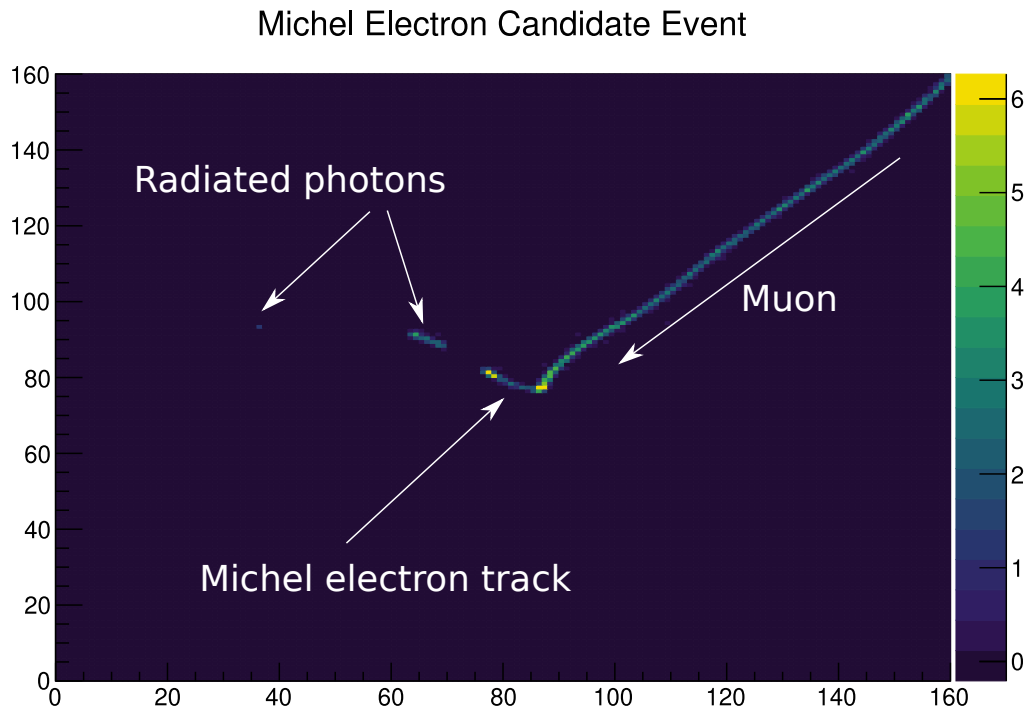
Figure 6.2: Michel electron candidate event from ProtoDUNE–SP data.

energy. While most of the radiated photons only carry a small fraction of the Michel electrons energy, in some cases a single radiated photon can carry a significant fraction of the electron energy. In addition, around the peak of the Michel electron spectrum (~ 45 MeV) there is a high photon multiplicity and a large spread in the multiplicity distribution. The combination of these effects leads to a significant spread in the fraction of radiated energy for Michel electron events.

Paragraph + figure on fraction of energy lost to radiation.

The energy which is lost into radiated photons is only visible once the photons interact in the argon to produce secondary electrons which then ionise the argon. These secondary electrons are scattered over large angles and distances in the detector when compared to the short Michel electron track, the spatial distribution of secondary electrons is shown in Fig. 6.4. TODO, analysis.
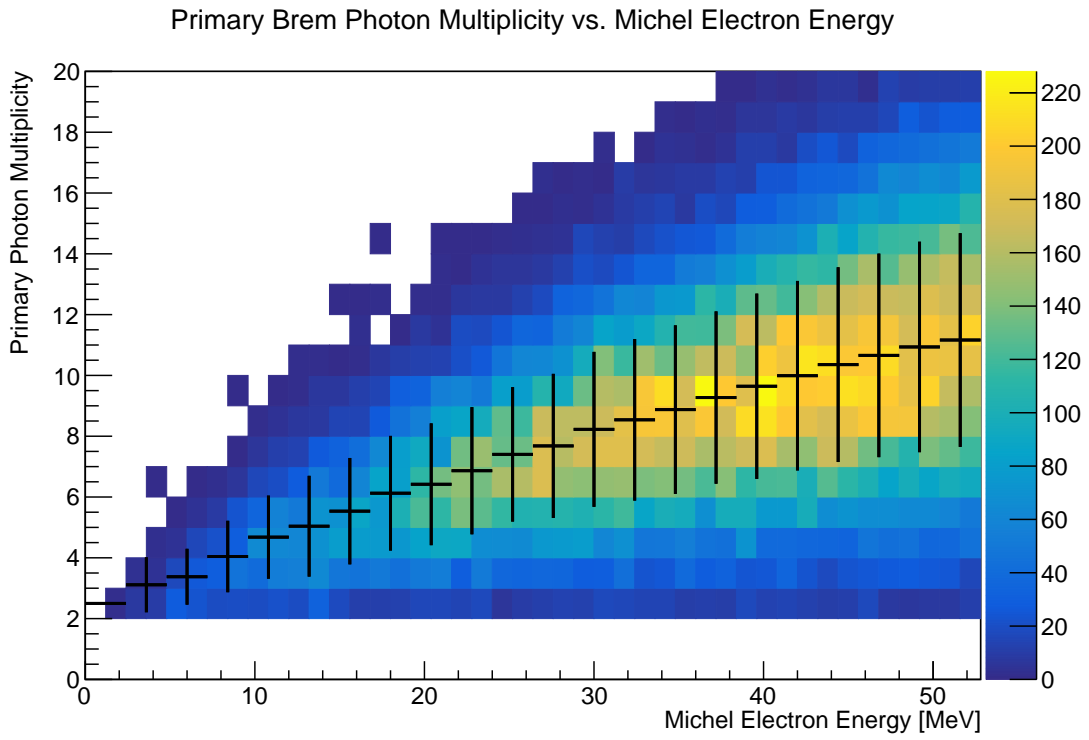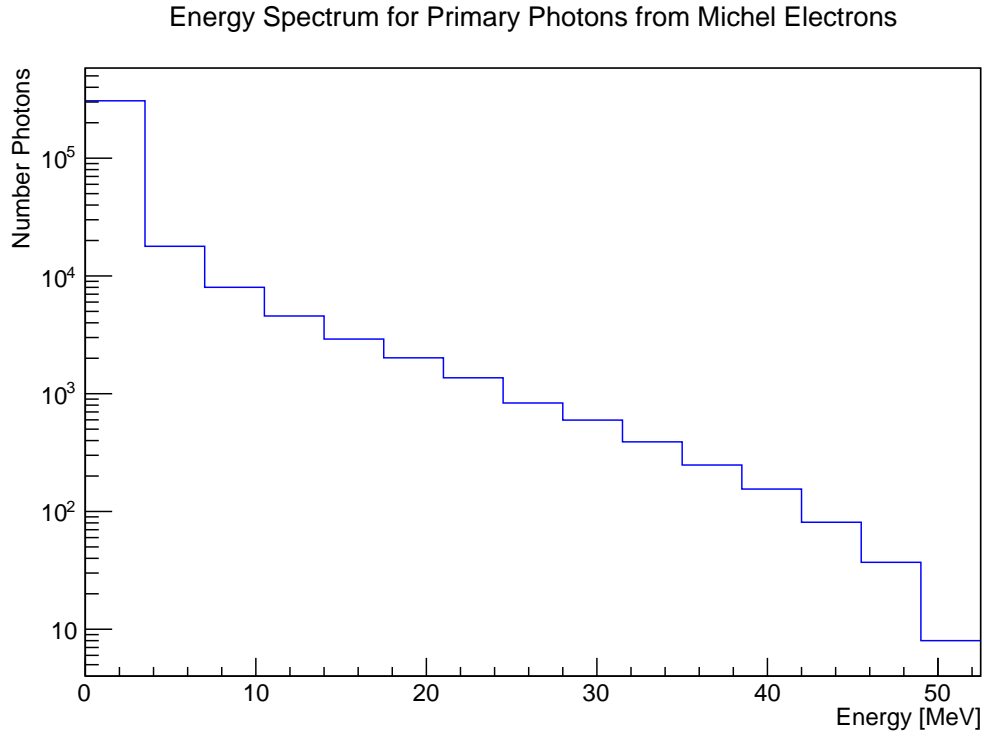
To highlight the impact of the radiated energy deposits we can consider the results of perfect energy reconstruction in two cases:

- Only considering the Michel electron track.

- Considering all ionisation energy within some radius and angle of the Michel electron track.

Fig. 6.5 illustrates the considerable increase in energy collected if radiated energy is considered, the distribution is significantly narrower and much more energy is recovered when considering the energy deposited within a cone of height 40cm and angle 30 °of the Michel electron vertex. The average energy recovered is increased from TODO % to TODO % and the spread is reduced from TODO % to TODO %.

TODO, figure and paragraph for energy fraction vs radius.

The MC study presented here highlights the importance of radiated energy deposits in Michel electron and other low–energy electron events. Based on these results it is clear that to minimise energy uncertainties for these events it is important to maximise the amount of energy collected from radiated photons. The rest of this chapter will discuss an algorithm which was developed to tackle this problem, and it's application on Michel electron events in ProtoDUNE–SP data.

Energy Spectrum for Primary Photons from Michel Electrons

(a) Photon energy spectrum.

Primary Brem Photon Multiplicity vs. Michel Electron Energy

(b) Photon multiplicity as a function of true Michel electron energy.

Figure 6.3: Properties of radiated energy deposits from Michel electrons in ProtoDUNE–SP simulation.
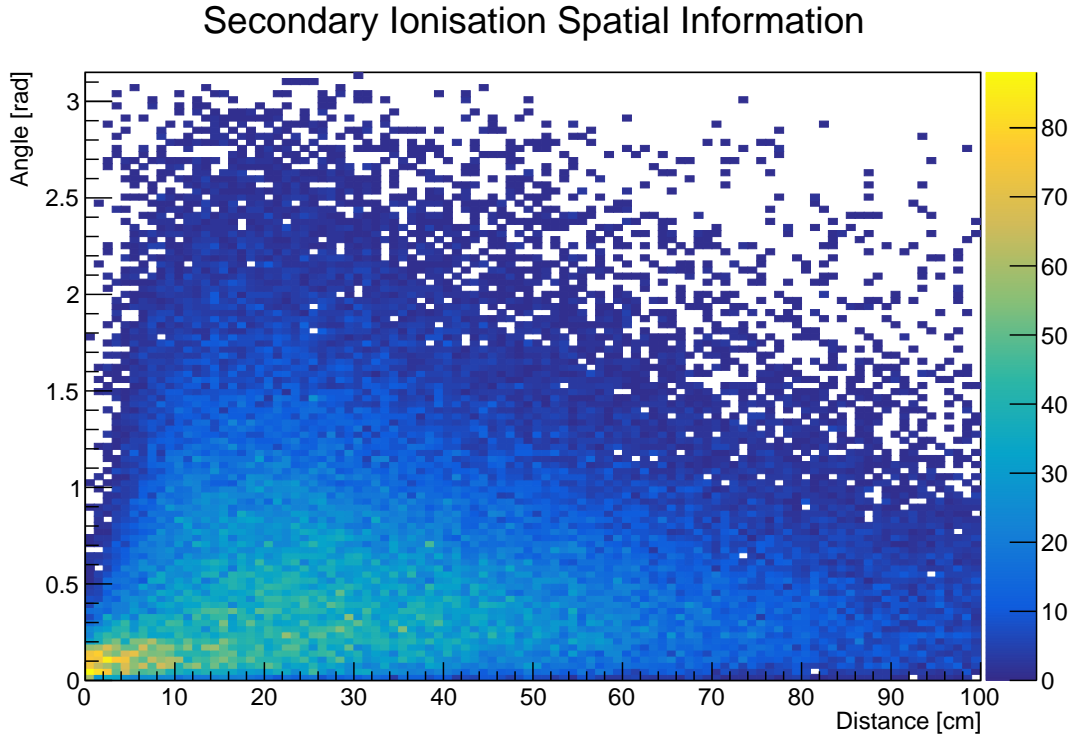
Figure 6.4: Spatial distribution of radiated ionisation deposits.

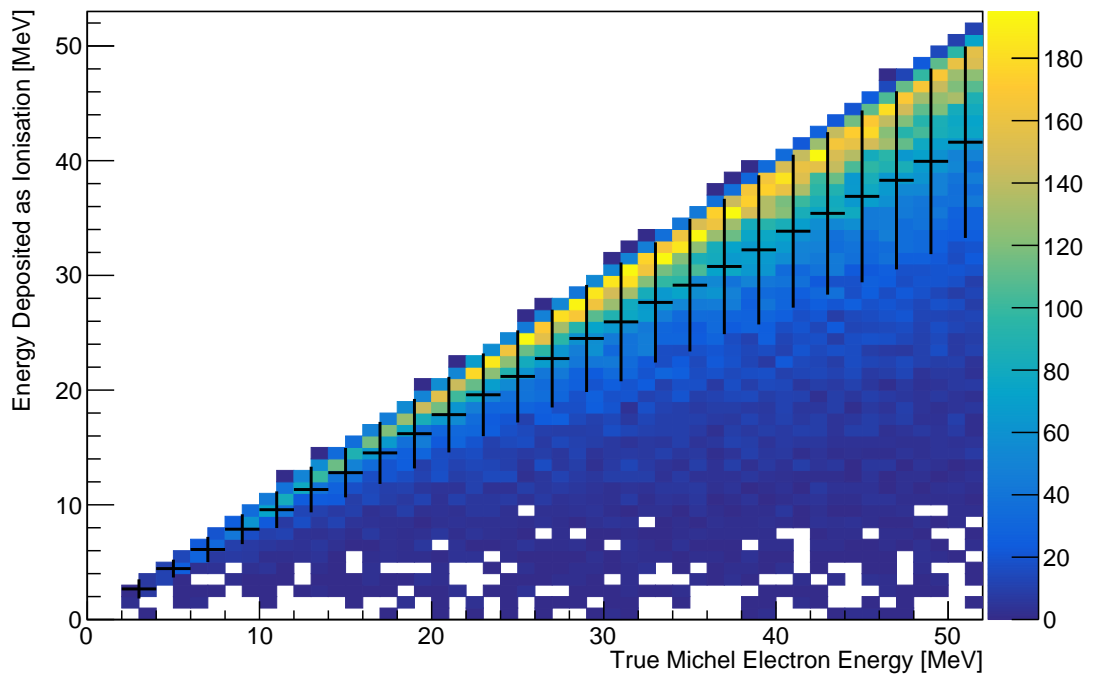## 6.2 Michel Electron Event Selection

In order to select Michel electrons in ProtoDUNE–SP data, an event selection algorithm was developed based on combining the results from the hit tagging CNN from the previous chapter with clustering performed by the main ProtoDUNE–SP reconstruction framework, Pandora. The performance of the Michel electron classifier in isolation are discussed in the previous chapter.

The event selection algorithm proceeds in the following steps:

1. Start with all primary tracks from Pandora.

2. Define a set of Michel electron candidates from the list of all daughters of the track.

3. Find the best Michel electron candidate from the list of Michel electron candidates.
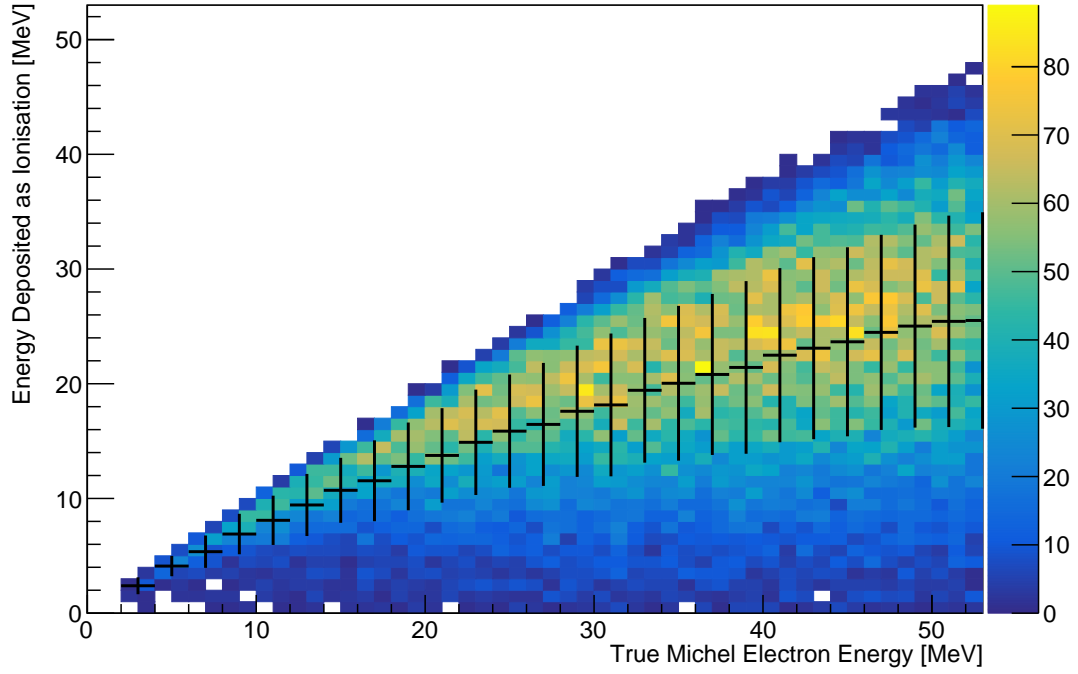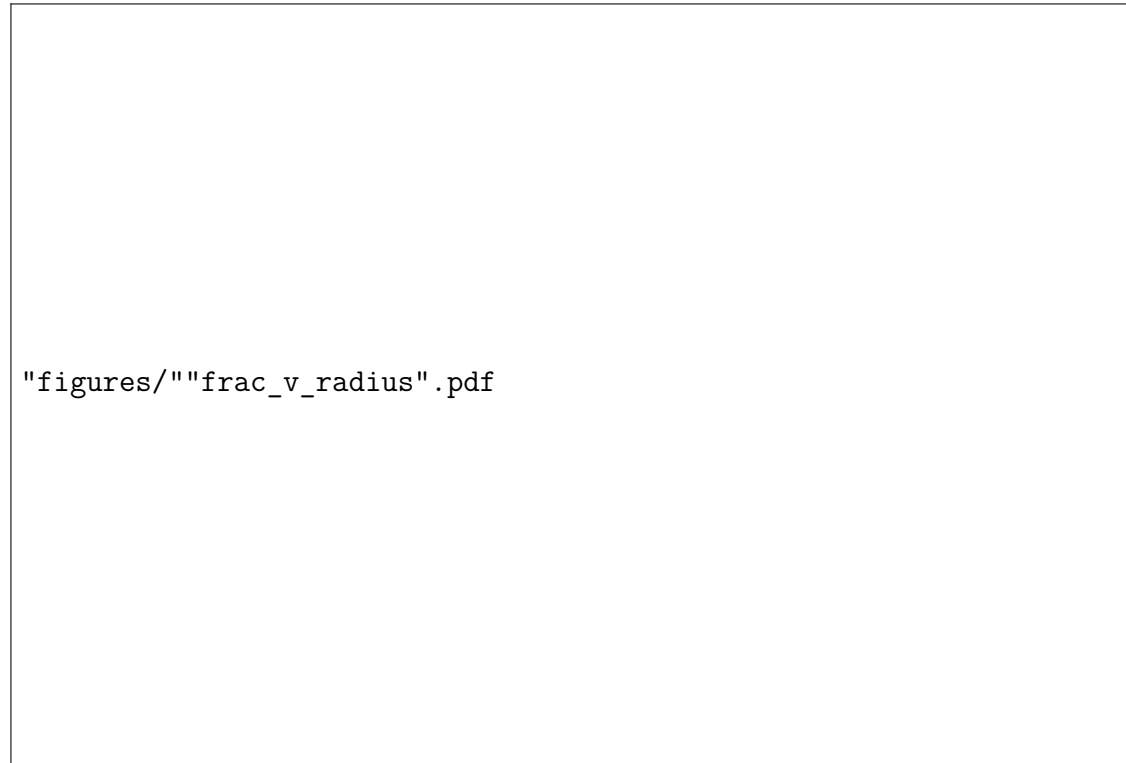
(a) Initial Michel electron track only.

(b) Ionisation withing a 40cm cone at 6 pening angle.

Figure 6.5: Available ionisation energy vs true Michel electron energy.

"figures/""frac_v_radius".pdf

Figure 6.6: Fraction of Michel electron energy collected vs collection radius.

4. Select events where the best Michel electron candidate passes the event selection cuts.

In the first step the initial sample of muon candidates is defined. All tracks from the Pandora reconstruction chain which have been labelled as primary tracks are considered.

The second step defines a set of Michel electron candidates for each track in the sample. A Michel electron candidate is any daughter of the primary Pandora track which satisfies the following conditions:

- Starts within 5 cm of the primary track endpoint.

- Contains a minimum of 5 hits on the collection plane.

In the third step the Michel electron candidates are analysed in order to define the best Michel electron candidate for each track. The best Michel electron candidate is the Michel electron candidate with the largest fraction of Michel–like hits based

Fraction of daughter particle hits that are Michel--like
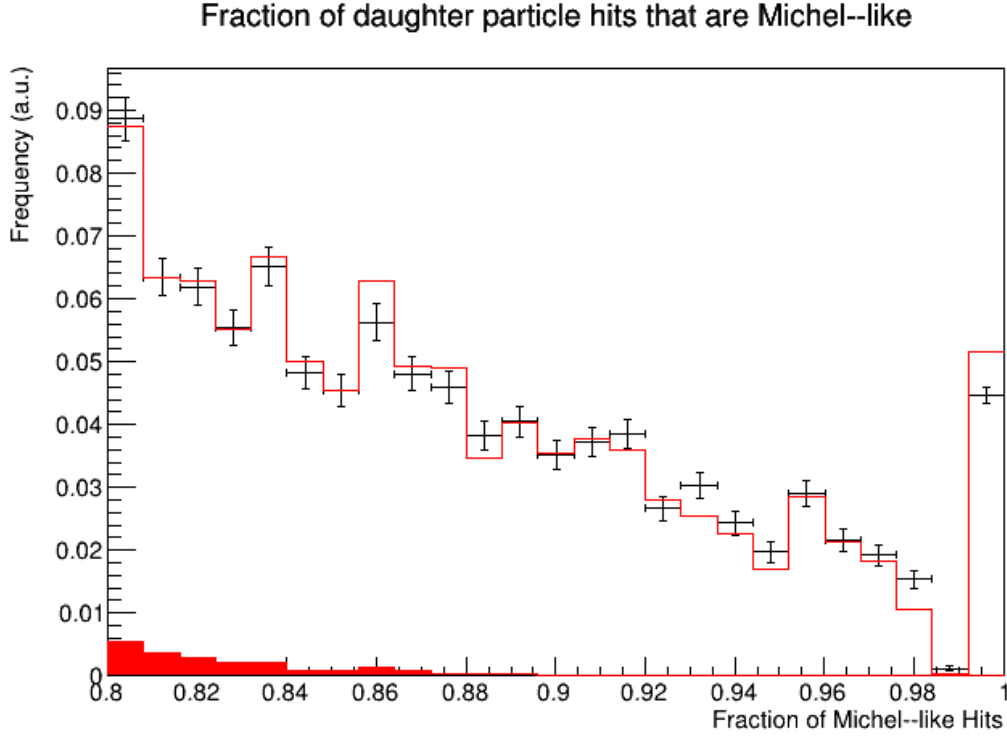
Figure 6.7: Fraction of Michel–like hits in the best Michel electron candidate.

on the output of the Michel electron score from the CNN with a threshold of 0.9. In the case of a tie the Michel electron candidate with the most hits is chosen.

The fourth step is the final decision, which is based on the fraction of Michel like hits in the best Michel electron candidate. Figure 6.7 shows a comparison of the fraction of Michel–like hits for the best Michel electron candidate in ProtoDUNE–SP data and simulation. TODO, analysis of fig. Events are selected if the best Michel electron candidate is made up of more than 80 % of Michel–like hits then it is selected as a Michel electron candidate.

Based on this algorithm Michel electron events are selected with an average purity of TODO % and an average efficiency of TODO % in ProtoDUNE–SP simulation. Figure 6.8 shows the distribution of event selection efficiency and purity as a function on Michel electron energy. TODO, analysis and figure.

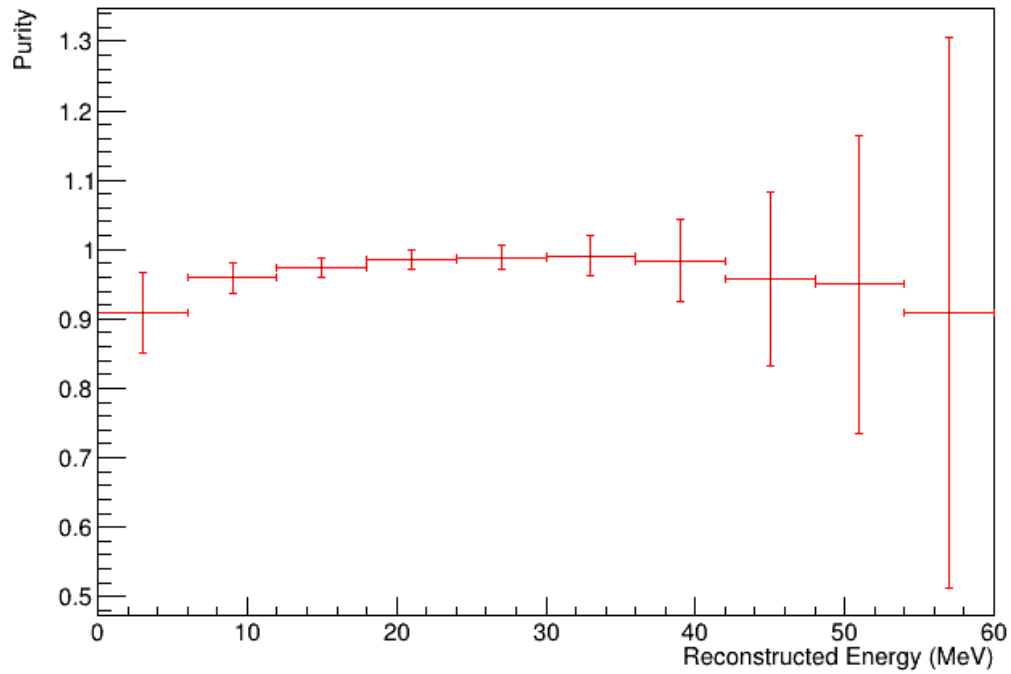TODO, muon kinematic distributions.
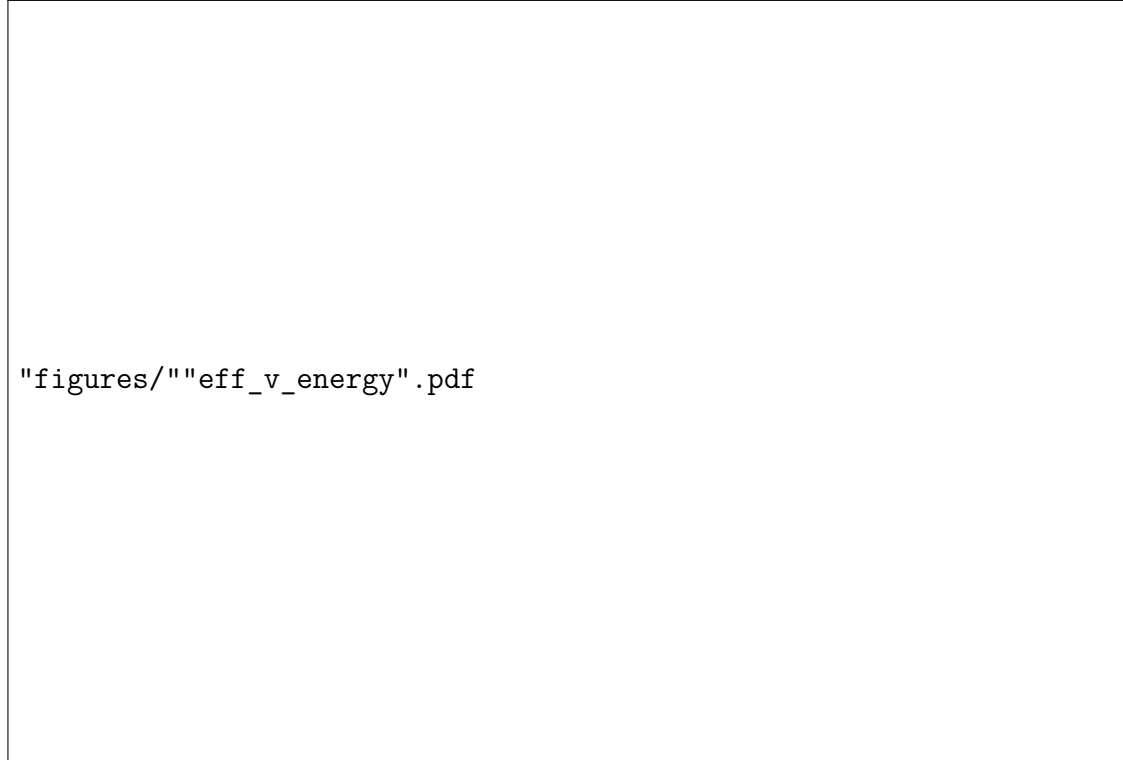
(a) Purity vs True Michel electron energy.

(b) Efficiency vs True Michel electron energy.

Figure 6.8: Purity and efficiency of Michel electron event selection as a function of energy.

6.3 Michel Electron Energy Reconstruction

To reconstruct the energy of Michel electrons in liquid argon the relevant hits must first be selected. Once the hits are selected the ionisation energy deposited by each hit is then reconstructed, the reconstructed energy of the Michel electron is the sum of the reconstructed energy of all relevant hits. In this section we will detail a hit selection algorithm based on a type of convolutional neural network called a U-Net, which returns hit selection maps for the Michel electron energy reconstruction. This algorithm is used to select Michel electron hits with a high purity and efficiency, the resulting reconstructed energy spectrum is used to estimate the energy resolution of ProtoDUNE–SP for electrons in the tens of MeV range.

6.3.1 Michel Electron Hit Tagging with U-Nets

A U-Net is a type of convolutional neural network which is designed to perform semantic segmentation of images [**TODO**]. In semantic segmentation the goal of the network is to return a map of pixels which correspond to the areas of interest; the output of the network is the same dimension as the input with a one–to–one correspondence between input pixels and output pixels. The architecture used for the hit selection algorithm is shown in Fig. 6.9. During the first half of the network architecture the resolution of the output is decreases, this is analogous to many conventional CNN's and during this phase the network learns about the content of the image. The second phase of the architecture allows the U-Net to rebuild the locations of different features within the initial image, this is achieved by passing the details of previous layers to the network as the resolution of the output map is slowly increased back to the original resolution [**TODO**].

In the Michel electron case, the goal of the network is to return a map of all ionisation energy deposits which come from the Michel electron, this includes the initial track and any secondary deposits from radiated photons. The inputs and outputs are two dimensional images of the location of reconstructed hits centered on the selected Michel electron. The amplitude of each input pixel is given by the integrated charge of any reconstructed hits within the pixel. For the outputs

the pixels have an amplitude of 1 if they contain a Michel electron hit, and 0 otherwise. Only data from the collection plane is used because there is a higher signal to noise ratio on these wires.

Intersection–over–union was used as the loss function for the U-Net. This loss is defined as

$$\mathrm{IOU}(A, B) = \frac{|A \cap B|}{|A \cup B|} \tag{6.1}$$

where A is the set of all selected hits, and B is the set of all true hits. This loss rewards the network for selecting as many correct hits as possible (high intersection), while penalising it for selecting more hits than it needs to (high union). The IOU score lies between 0 and 1, with a score of 1 corresponding to a perfect match between the two sets and therefore perfect hit tagging in our Michel electron case.

The network architecture used for the Michel electron reconstruction is shown in Figure 6.9. The network consists of a repeating structure which contains the following key components:

- Convolutional layers in the form of inception units.

- Pooling layers for downscaling.

- Residual connections and up–sampling.

FIXME. Description. As with the hit tagging CNN from the previous chapter, both dropout and early–stopping are implemented to prevent over–fitting.

The datasets for the training process were generated from a full simulation of the ProtoDUNE–SP detector under beam operation including both cosmic ray and beam particles. The images produced contain the location and integrated charge for each hit within the image window. The training data is split into training, test, and validation sets in the ratio 80:10:10. In total around 40,000,000 images were generated for the training stage.

As with the hit tagging CNN from the previous chapter, the training and validation scores were monitored throughout training using TensorFlow. The

"figures/""unet_arch".png
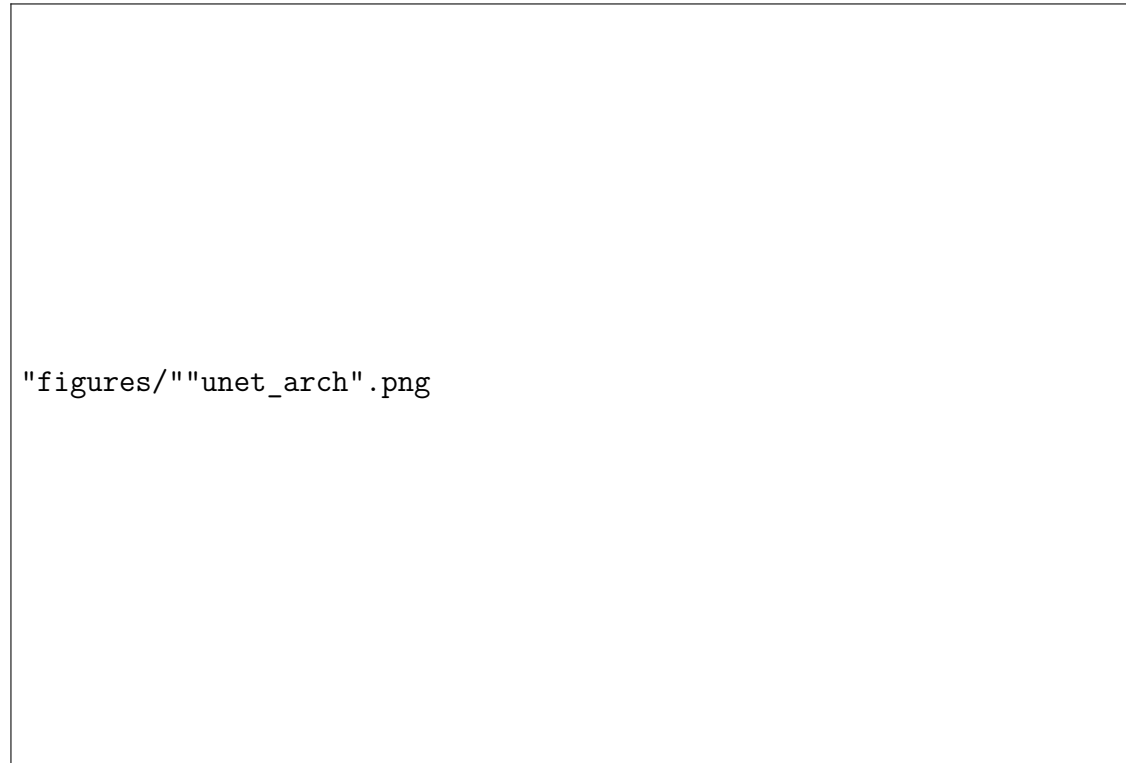
Figure 6.9: CNN architecture used to select ionisation energy deposits.

weights of the network were saved after each epoch, and the final weights were those from the epoch before the epoch when the validation score first decreased. Figure 6.10 shows the evolution of the loss over time, along with a vertical line representing the loss at which the weights were chosen.

A demonstration of the output of the U-Net is given in Figure 6.11 which shows the input, output, and truth images for an event from ProtoDUNE–SP simulation.

6.3.2 Michel Electron Reconstruction

Michel electron reconstruction was evaluated on a dataset which was part of the same batch of simulation as the training, test, and validation data, but distinct from all of them.

6.3.2.1 Hit Selection

The U-Net produces a sharply peaked output distribution in both data and simulation as seen in Figure 6.12, which shows sharp peaks in the distribution
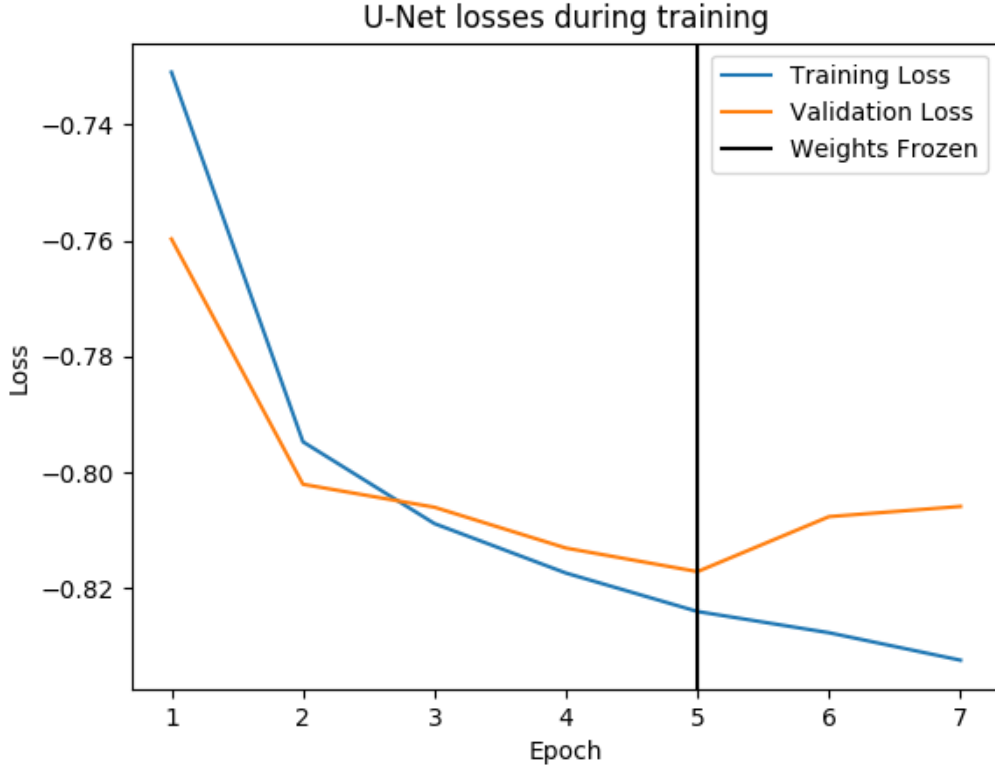
Figure 6.10: U-Net training and validation loss as a function of epoch.

at 0 and 1. The distribution has slightly sharper peaks in simulation as with seen with the hit tagging CNN from the previous chapter, this is unsurprising due to the fact that the simulation does not perfectly match the data. TODO. Is there a good way to mitigate this?

Hits from the input images are selected as Michel electron hits if their score exceed a selection threshold of 0.9. The number of hits selected per event for data and simulation is shown in figure 6.13. Around 10 hits are selected on average per event, with a slightly larger spread in data than in simulation.

The performance of the hit tagging algorithm was analysed with the simulated sample. The U-Net output distribution for true Michel electron hits and falsely tagged hits is shown in Figure 6.14, along with a ratio of the true and false hits as a function of energy. The ratio shows a strong separation between true hits and false hits, which appear at high scores and low scores respectively.
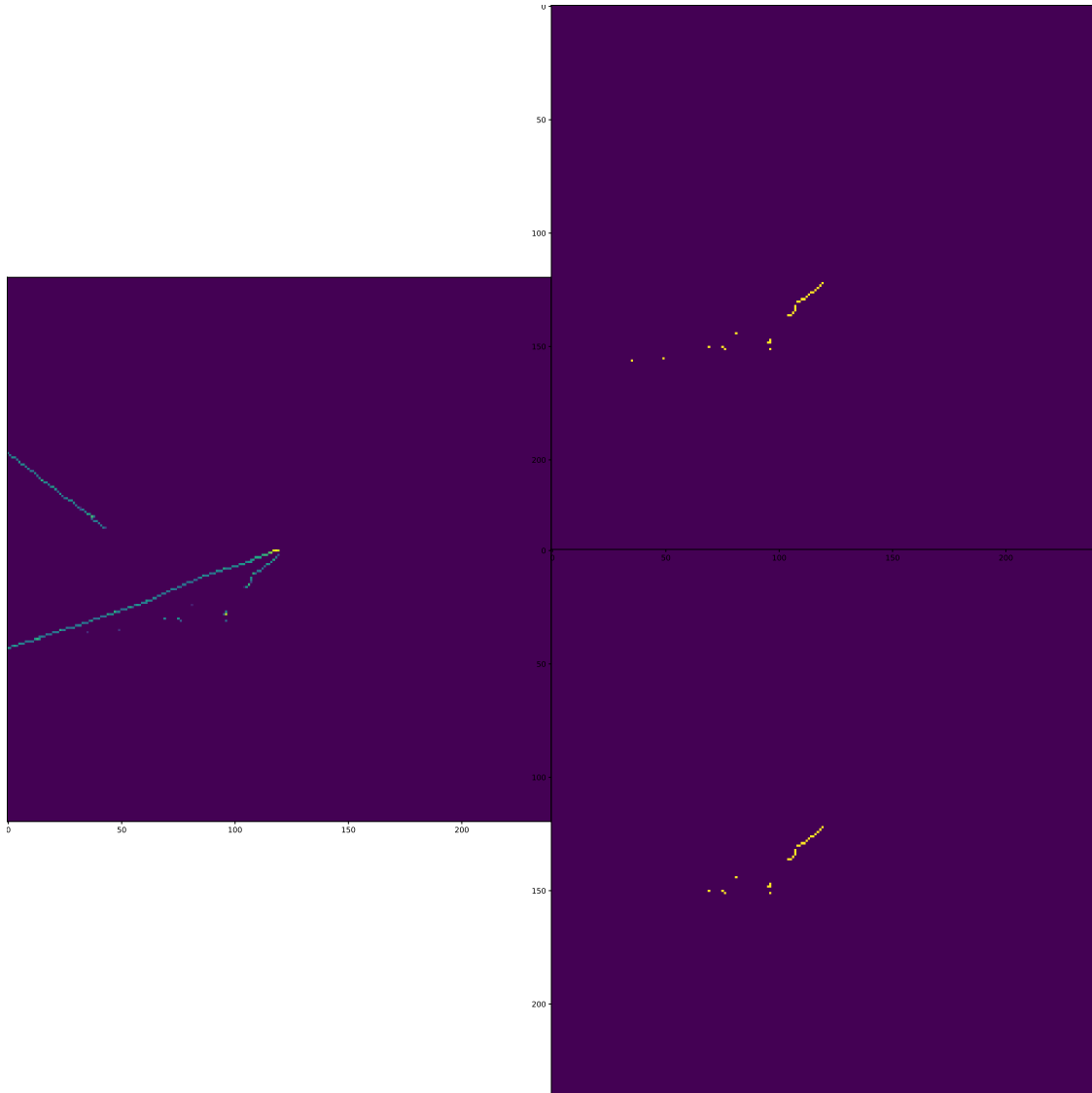
Figure 6.11: Example input, true output, and prediction images for U-Net. Left: Input image. Top Right: True Output. Bottom Right: U-Net Prediction.

Based on the score distributions for true and false hits the precision and completeness of the hit tagging algorithm can be evaluated. The precision and completeness are defined as

$$\text{Precision} \quad = \quad \frac{N_{TP}}{N_{TP} + N_{FP}} \tag{6.2}$$

$$\text{Completeness} \quad = \quad \frac{N_{TP}}{N_{TP} + N_{FN}} \tag{6.3}$$

where N_{TP}, N_{FP}, and N_{FN} are the number of true–positive, false–positive, and false–negative hits respectively. These parameters give a quantitative evaluation
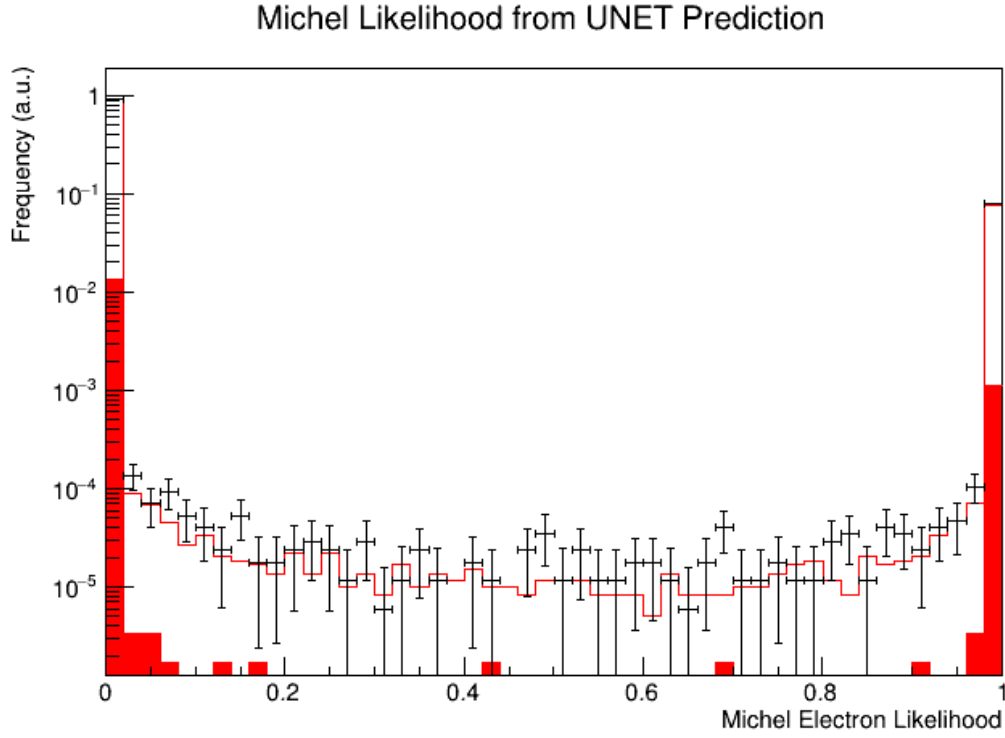
Figure 6.12: U-Net Predicted Distribution.
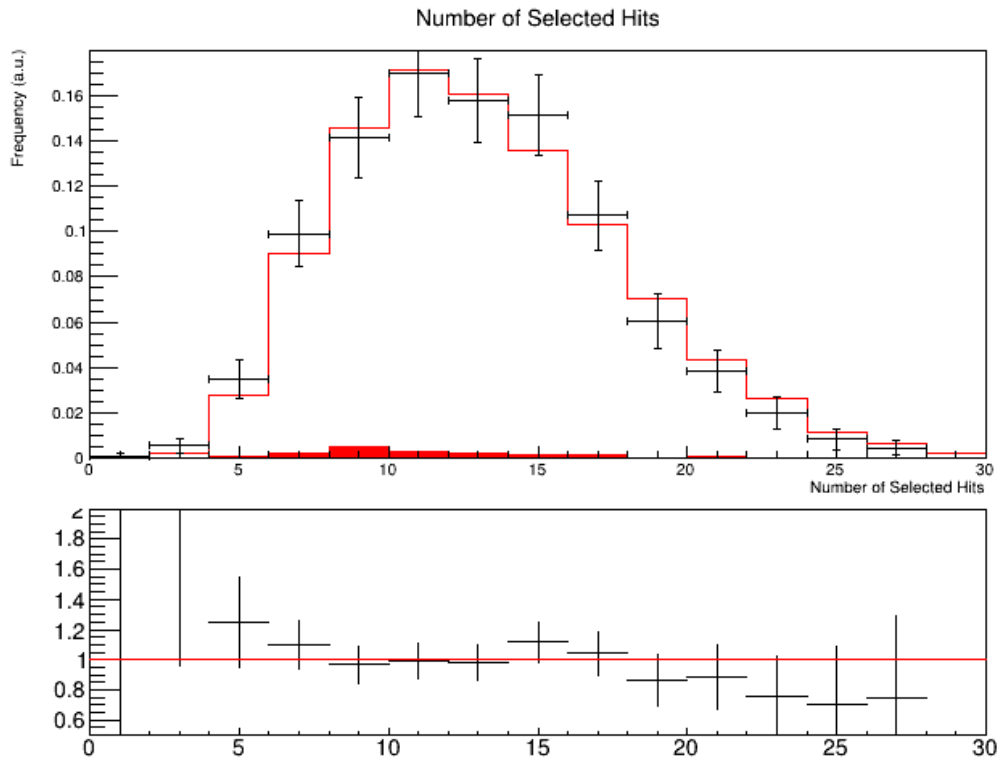
Figure 6.13: Number of hits in Michel electron events.
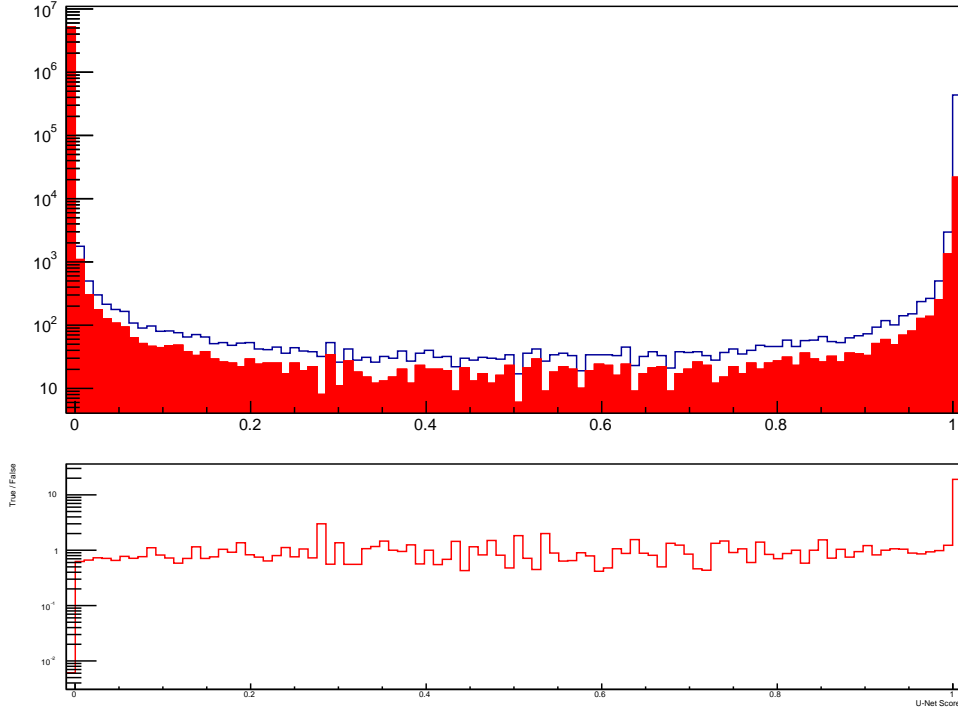
**Figure 6.14:** U-Net output distribution.

of the performance of the hit tagging algorithm, allowing for comparison between different algorithms. The purity and completeness of the hit tagging was calculated for a range of selection thresholds in the range $[10^{-7}, 1 - 10^{-7}]$, Figure 6.15 shows the purity against completeness for the values in this range. The hit tagging algorithm produces a high precision and completeness throughout range of thresholds, however the steepness of the distributions means that the choice of threshold makes little difference to the performance meaning that little can be done to optimise the performance by varying the threshold.

6.3.2.2 Ionisation Energy Reconstruction

The total ionisation energy is reconstructed by summing the hit–by–hit ionisation energy for all hits selected by the U-Net. The ionisation energy for each hit is reconstructed from the hit integral in ADC as

$$E_{hit} = \frac{I_{hit} \times C_X \times C_{YZ} \times N \times W_{ion}}{C \times R}, \qquad (6.4)$$

## Purity vs completeness for varying threshold
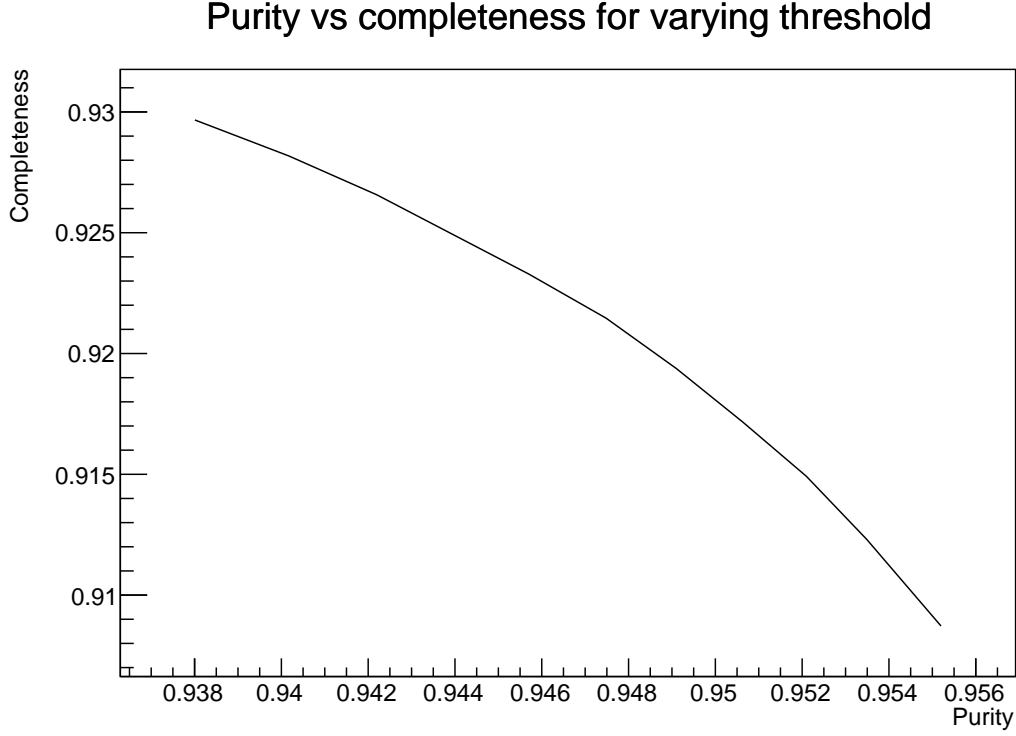
Figure 6.15: U-Net purity vs completeness.

where E_{hit} is the reconstructed hit energy in MeV, I_{hit} is the integrated hit charge in ADC, C_X is the X–correction factor which is dependent on the X coordinate of the hit within the TPC, C_{YZ} is the YZ–correction factor which is dependent on the Y and Z coordinates of the hit within the TPC, N is a dimensionless normalisation factor which normalises the data and MC distributions to give the same magnitude, W_{ion} is the ionisation energy of argon in MeV per electron, C is a constant conversion factor which has units ADC per electron, and R is the recombination factor. The distribution of reconstructed hit energies in ProtoDUNE–SP data and simulation is shown in Figure 6.16.

The position dependent calibration matrices correct for non-uniformity in the detector response across the TPC. In the X direction the main contributing factors are attenuation due to electron absorption, and variations in the electron drift velocity due to space charge effects. The main contributing factor for the YZ–correction matrix is wire–to–wire response variations.

As discussed in chapter 4 the recombination factor is a $\frac{dE}{dx}$ dependent factor

Reconstructed Hit Energy
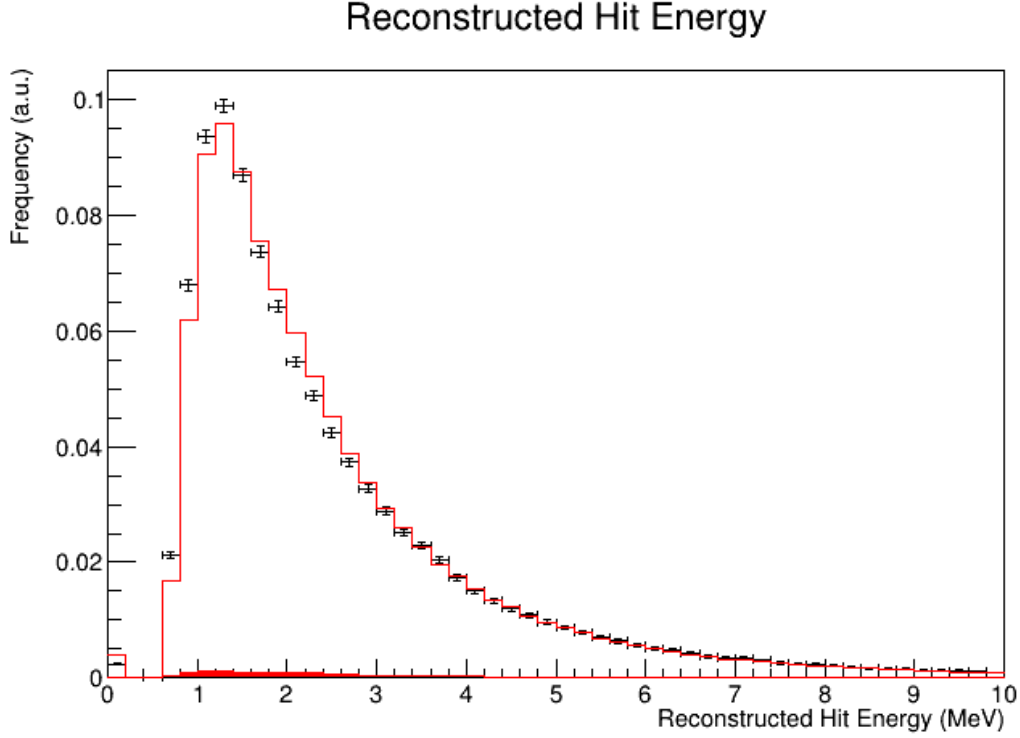
Figure 6.16: Reconstructed Hit Ionisation Energy

which depends on the conditions in the liquid argon. Due to the shortness of Michel electron tracks and the other charge deposits it is challenging to assign $\frac{dE}{dx}$ on a hit–by–hit basis for this sample, therefore, an average recombination factor is used for all hits. The recombination factor is calculated using the box model [**TODO**] under ProtoDUNE–SP operating conditions to be 0.69.
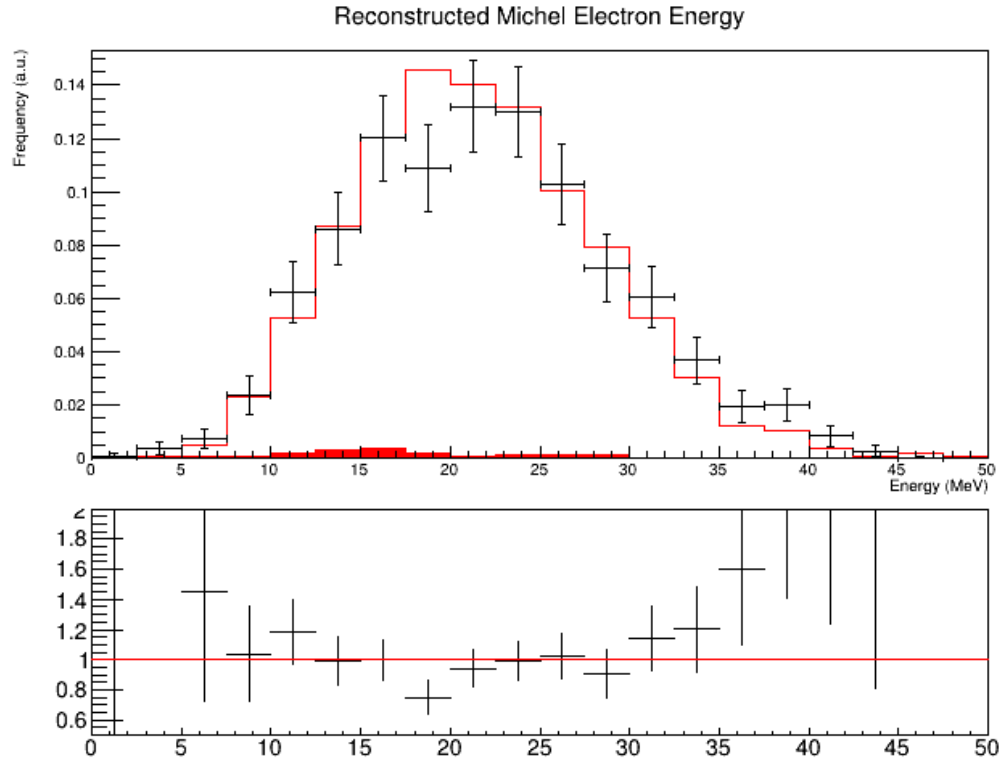
The reconstructed ionisation energy spectrum from Michel electron candidates is shown in Figure 6.17 along with the average ionisation energy per hit. The distribution peaks at around 18 MeV and has a tail up to just under 50 MeV.

TODO: analysis of ionisation reconstruction performance.

TODO: Energy resolution fits vs energy.

6.3.2.3 Michel Electron Energy Reconstruction

The true Michel electron energy includes contributions from scintillation light as well as radiated ionisation energy which is not contained within the images used in reconstruction. To estimate the total Michel electron energy the reconstructed

Figure 6.17: Reconstructed Michel Electron Ionisation Energy

Figure 6.18: Reconstucted Ionisation vs True Ionisation.

"figures/""frac_diff_v_ion".png
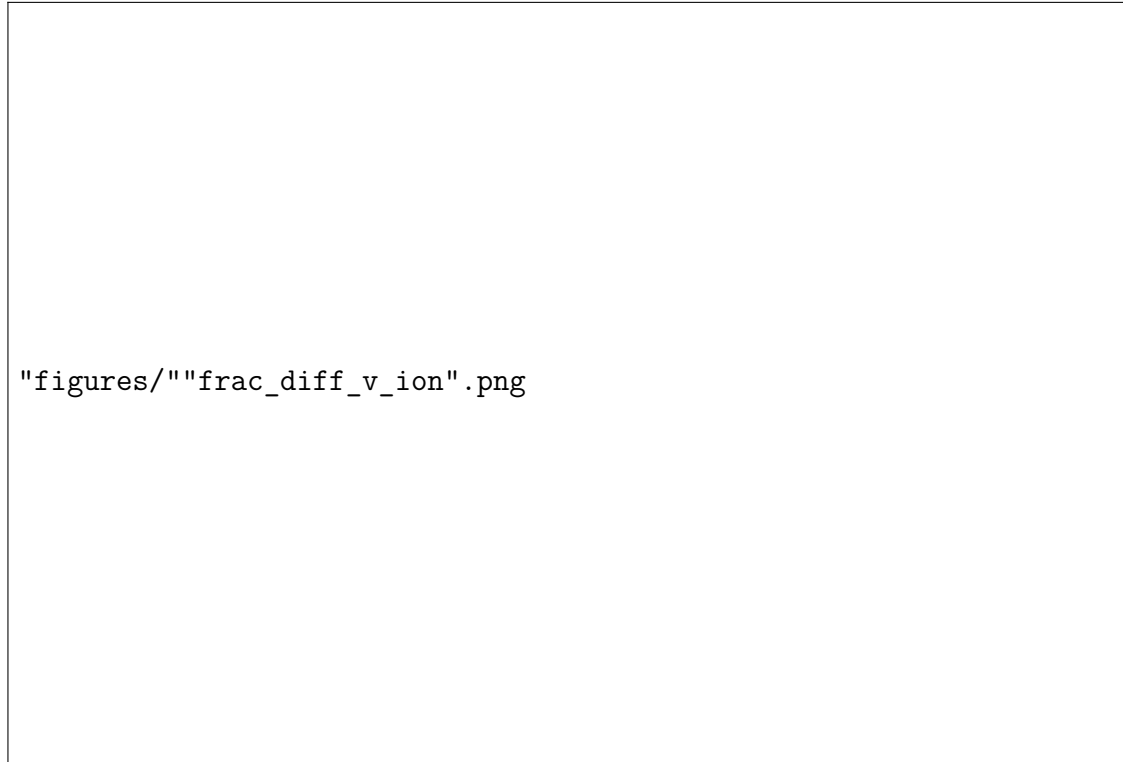
Figure 6.19: Fractional energy difference between reconstructed and true Michel electron energy.

"figures/""res_bias_v_ion".png

Figure 6.20: Energy resolution and bias as a function of true ionisation energy.

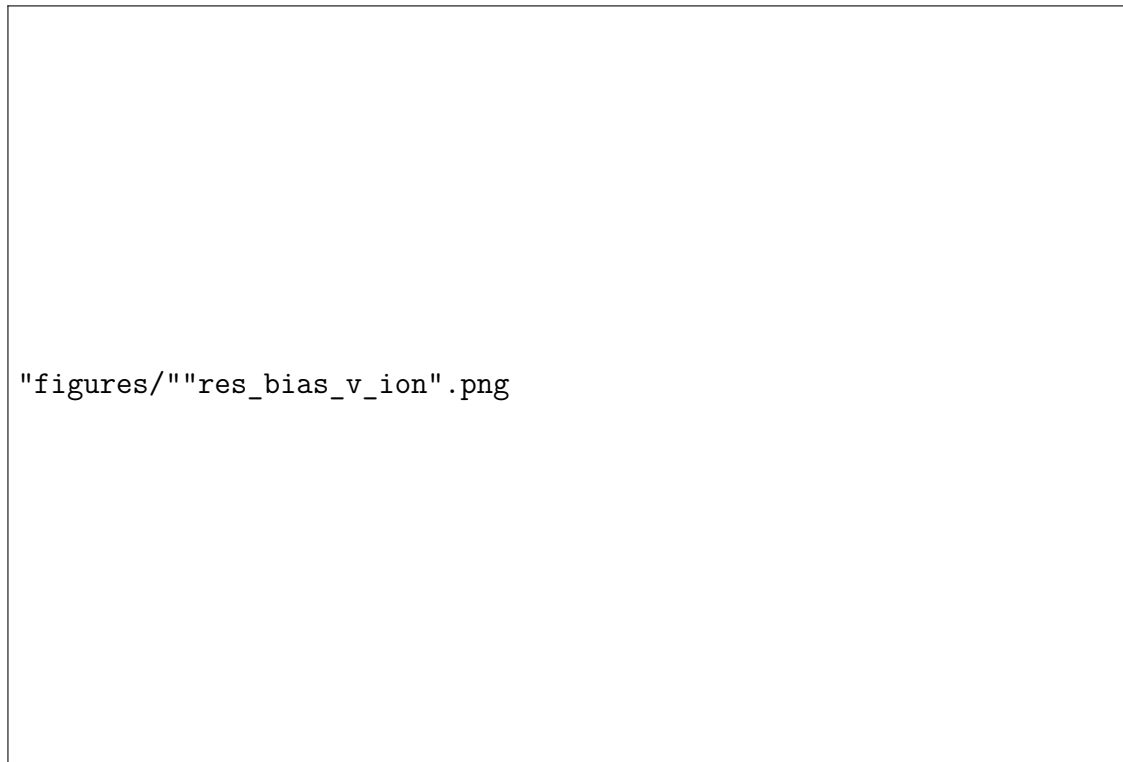ionisation energy needs to be scaled to account for these losses. As shown in Figure 6.5 there is a none–linear correlation between the true Michel electron energy and the available ionisation energy in reconstruction, therefore, a quadratic energy scaling factor was used to convert the reconstructed ionisation energy into a reconstructed Michel electron energy.

The energy scaling factor was estimated by fitting the reconstructed ionisation energy as a function of true Michel electron energy in ProtoDUNE–SP simulation with a quadratic correction as shown in Figure 6.21. This quadratic is then inverted to give the reconstructed Michel electron energy for a given reconstructed ionisation energy,

$$E_{michel} = \left(\frac{E_{ion}}{a} - d \right)^{\frac{1}{2}} - \frac{b}{2a}, \quad d = \frac{c}{a} - \left(\frac{b}{2a} \right)^2 \tag{6.5}$$

where E_{michel} is the reconstructed Michel electron energy, E_{ion} is the reconstructed ionisation energy, and a, b, and c are the parameters from the quadratic fit. The fit gives

$$a = TODO, \tag{6.6}$$

$$b = TODO, \tag{6.7}$$

$$c = TODO. \tag{6.8}$$

The reconstructed Michel electron energy spectrum is shown in Figure 6.22, alongside the true Michel electron energy spectrum from the simulation. There is a significant difference in the shape of the two spectra, this is due to the significant energy loss to scintillation and radiation that cannot collected in ProtoDUNE–SP due to challenges in the reconstruction.

TODO: Energy resolution fits vs energy.

The energy uncertainty and bias are estimated by fitting the fractional energy difference between the reconstructed and true Michel electron energies as a function of true Michel electron energy. The fractional energy difference, defined as

$$\Delta = \frac{E_{reco} - E_{true}}{E_{true}}, \tag{6.9}$$
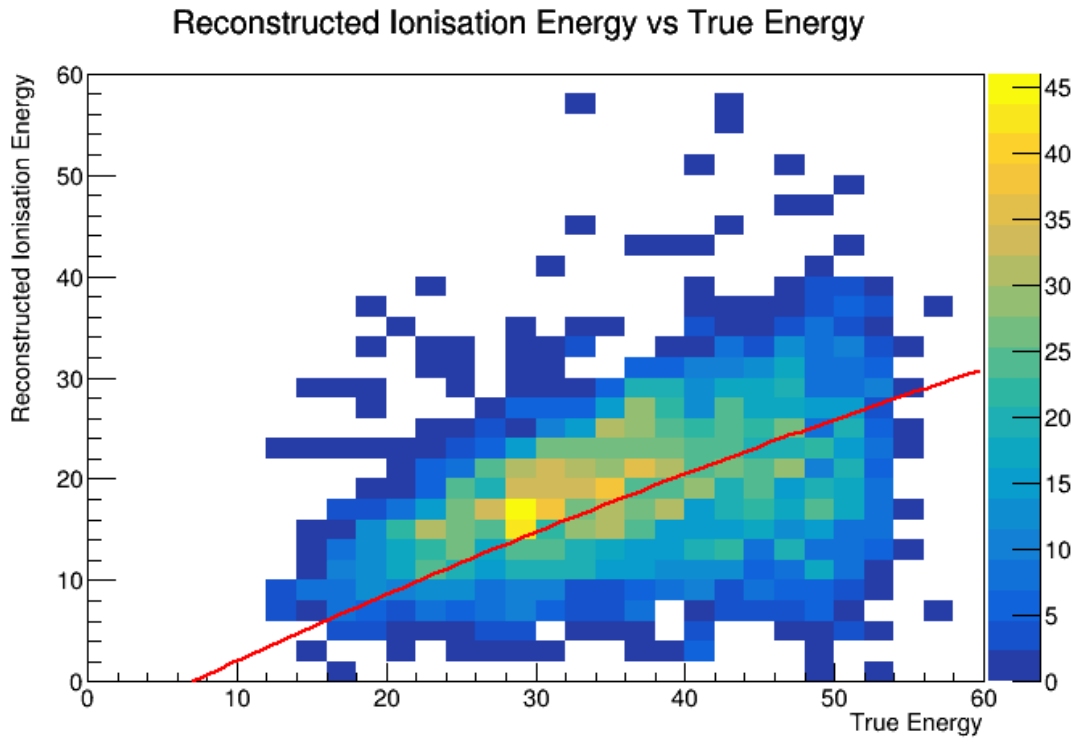
Figure 6.21: Quadratic Energy Scale Factor.

"figures/""reco_v_mich".png
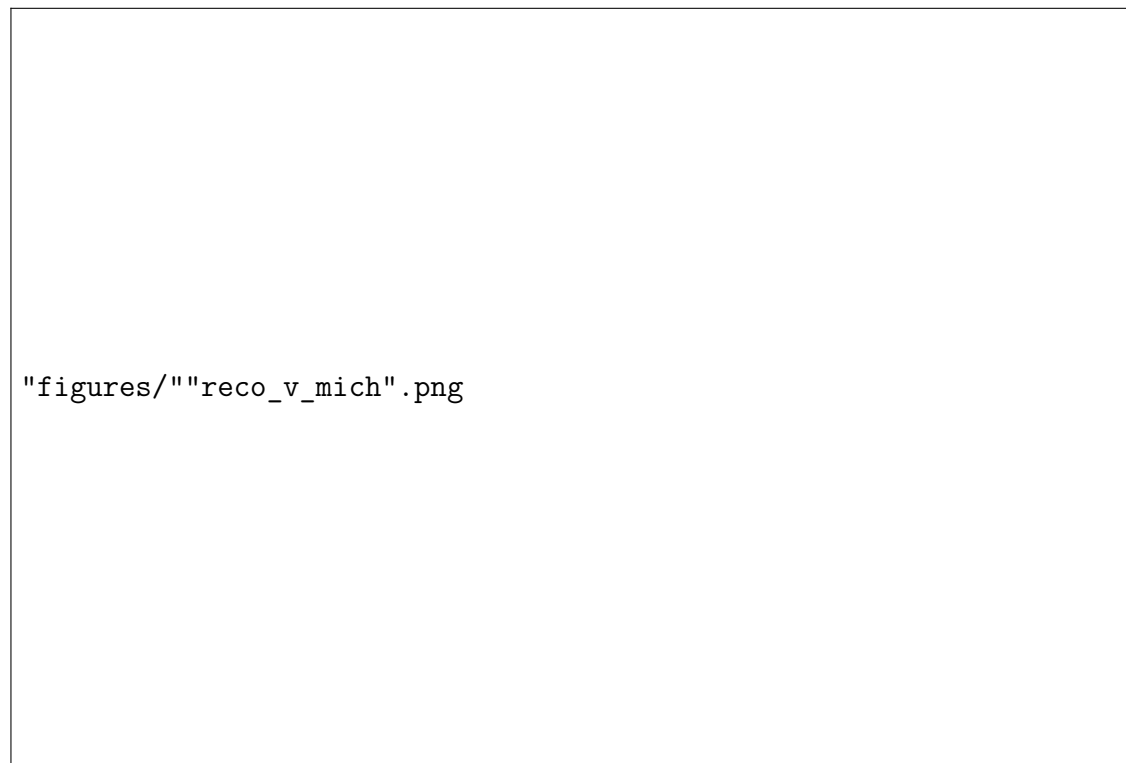
Figure 6.22: Reconstructed Energy vs True Michel Electron Energy.

```
"figures/""frac_diff_v_energy".png
```

Figure 6.23: Fractional energy difference between reconstructed and true Michel electron energy.

is considered in bins of true Michel electron energy which are plotted in Figure 6.23. This difference is fit with a gaussian distribution in each bin in order to estimate the energy uncertainty and bias as a function of the true Michel electron energy.
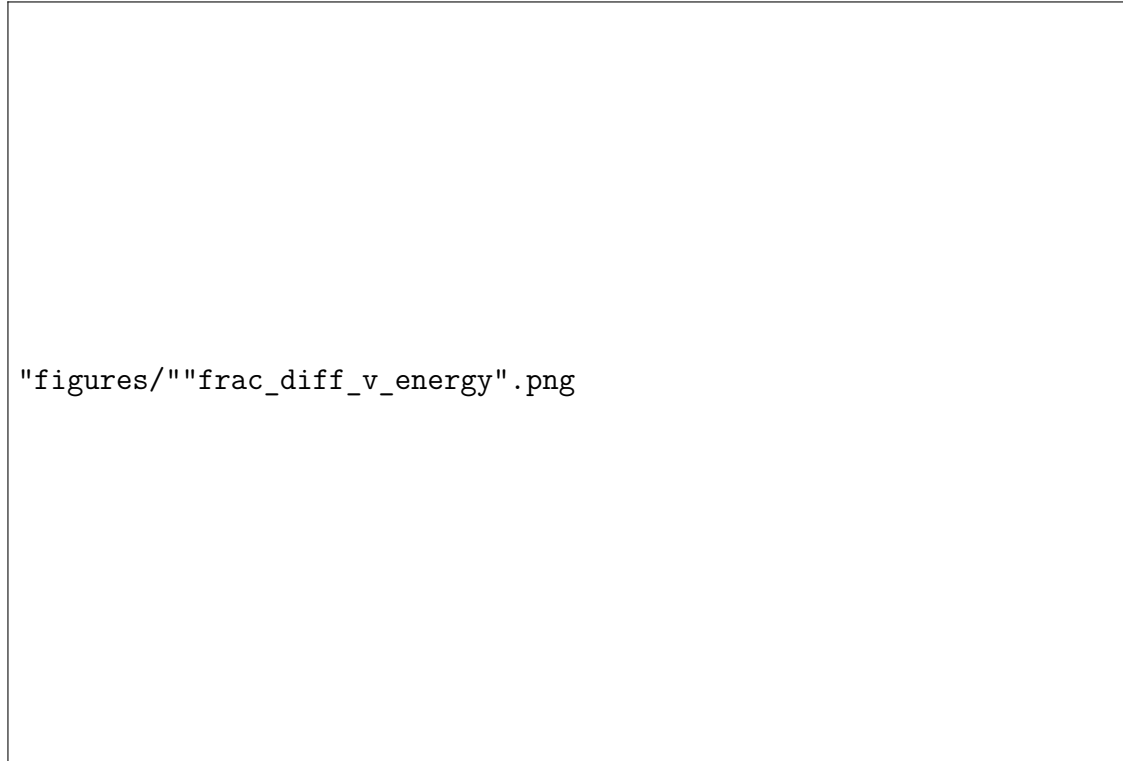
The energy resolution and bias as a function of true Michel electron energy are estimated as the standard deviation and mean of the gaussian fit to the fractional energy difference in each energy bin, these values are plotted in Figure 6.24. TODO: analysis of results.

6.4 Conclusions

- Reco energy scaling

- Uncertainty vs energy

- Differences in dune far detector

"figures/""res_bias_v_energy".png
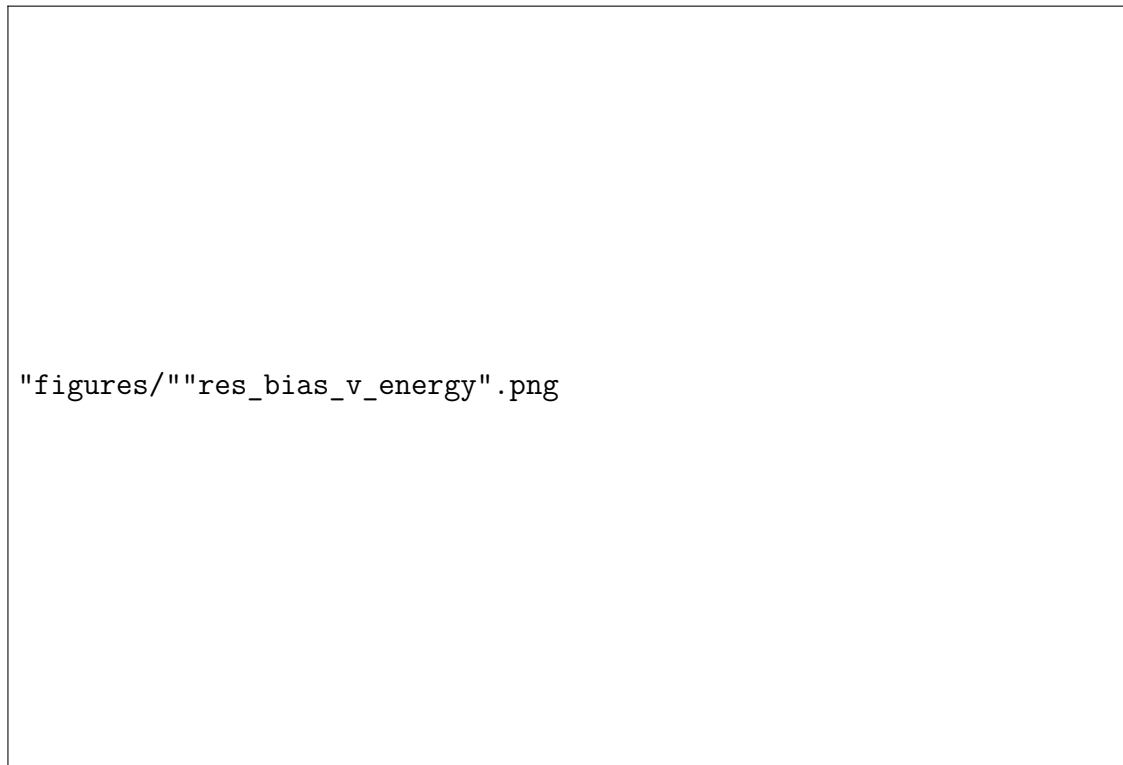
Figure 6.24: Energy resolution and bias as a function of true Michel electron energy.

7
Implications for DUNE

This chapter will analyse the implications of the measured uncertainties on analyses for the DUNE experiment. In particular the impact of the measured energy scale uncertainty and energy scale bias on supernova neutrino physics in DUNE will be analysed. The difference in conditions between ProtoDUNE–SP and DUNE will be highlighted and the expected implications for energy scale uncertainties in DUNE will be discussed.

The work for this section has yet to be started as it will be dependent on the outcome of the Michel electron analysis in the previous section. I expect to be able to start work on this analysis in September/October 2019 after preliminary results of the Michel electron analysis; work for this section will be completed by the end of December 2019.

7.1 Supernova Neutrinos in DUNE

7.2 Impacts of Energy Uncertainties

8
Conclusions

This chapter will summarise the work presented in the thesis and provide concluding remarks on the implications of the results for future analyses in LArTPC experiments.

References

[1] G. Vedovato et al. "GW170817: Observation of Gravitational Waves from a Binary Neutron Star Inspiral". In: *Physical Review Letters* 119.16 (2017), pp. 30–33.

[2] M. G. Aartsen et al. "Multimessenger observations of a flaring blazar coincident with high-energy neutrino IceCube-170922A". In: *Science* 361.6398 (2018). arXiv: 1807.08816.

[3] Kate Scholberg. "Supernova Neutrino Detection". In: *Ann. Rev. Nucl. Part. Sci.* 62 (2012), pp. 81–103. arXiv: 1205.6003 [astro-ph.IM].

[4] R. Acciarri et al. "Long-Baseline Neutrino Facility (LBNF) and Deep Underground Neutrino Experiment (DUNE)". In: (2016). arXiv: 1601.05471 [physics.ins-det].

[5] R. Acciarri et al. "Design and Construction of the MicroBooNE Detector". In: *JINST* 12.02 (2017), P02017. arXiv: 1612.05824 [physics.ins-det].

[6] F. Cavanna et al. "LArIAT: Liquid Argon In A Testbeam". In: (2014). arXiv: 1406.5560 [physics.ins-det].

[7] M. Antonello et al. "A Proposal for a Three Detector Short-Baseline Neutrino Oscillation Program in the Fermilab Booster Neutrino Beam". In: (2015). arXiv: 1503.01520 [physics.ins-det].

[8] B. Abi et al. "The Single-Phase ProtoDUNE Technical Design Report". In: (2017). arXiv: 1706.07081 [physics.ins-det].

[9] R. Acciarri et al. "Michel Electron Reconstruction Using Cosmic-Ray Data from the MicroBooNE LArTPC". In: *JINST* 12.09 (2017), P09014. arXiv: 1704.02927 [physics.ins-det].

[10] E. Fermi. "Versuch einer Theorie der β-Strahlen. I". In: *Zeitschrift für Physik* 88.3-4 (1934), pp. 161–177.

[11] H. Bethe and R. Peierls. "The Neutrino". In: *Nature* 133.532 (1934).

[12] F. Reines and C. L. Cowan. "Detection of the free neutrino". In: *Physical Review* 92.3 (1953), pp. 830–831.

[13] G. Danby et al. "Observation of high-energy neutrino reactions and the existence of two kinds of neutrinos". In: *Physical Review Letters* 9.1 (1962), pp. 36–44.

[14] F. J. Hasert et al. "Observation of neutrino-like interactions without muon or electron in the gargamelle neutrino experiment". In: *Physics Letters B* 46.1 (1973), pp. 138–140.

[15] K. Kodama et al. "Observation of tau neutrino interactions". In: *Physics Letters, Section B: Nuclear, Elementary Particle and High-Energy Physics* 504.3 (2001), pp. 218–224.

[16] "Electroweak parameters of the Z^0 resonance and the standard model". In: *Physics Letters B* 276.1 (1992), pp. 247–253. URL: http://www.sciencedirect.com/science/article/pii/037026939290572L.

[17] Raymond Davis, Don S. Harmer, and Kenneth C. Hoffman. "Search for neutrinos from the sun". In: *Physical Review Letters* 20.21 (1968), pp. 1205–1209.

[18] John N. Bahcall, Neta A. Bahcall, and Giora Shaviv. "Present status of the theoretical predictions for the Cl36 solar-neutrino experiment". In: *Physical Review Letters* 20.21 (1968), pp. 1209–1212.

[19] K. S. Hirata et al. "Experimental study of the atmospheric neutrino flux". In: *Physics Letters B* 205.2-3 (1988), pp. 416–420.

[20] Y. Fukuda et al. "Evidence for oscillation of atmospheric neutrinos". In: *Physical Review Letters* 81.8 (1998), pp. 1562–1567.

[21] Q. R. Ahmad et al. "Direct Evidence for Neutrino Flavor Transformation from Neutral-Current Interactions in the Sudbury Neutrino Observatory". In: *Physical Review Letters* 89.1 (2002), pp. 6–11. arXiv: 0204008v2 [arXiv:nucl-ex].

[22] A. Yu. Smirnov. "Solar neutrinos: Oscillations or No-oscillations?" In: (Sept. 2016). arXiv: 1609.02386 [hep-ph].

[23] K. Eguchi et al. "First Results from KamLAND: Evidence for Reactor Antineutrino Disappearance". In: *Physical Review Letters* 90.2 (2003), p. 6. arXiv: 0212021v1 [arXiv:hep-ex].

[24] T. Araki et al. "Measurement of neutrino oscillation with KamLAND: Evidence of spectral distortion". In: *Physical Review Letters* 94.8 (2005), pp. 1–5. arXiv: 0406035v3 [arXiv:hep-ex].

[25] N. Agafonova et al. "Observation of a first ν_τ candidate event in the OPERA experiment in the CNGS beam". In: *Physics Letters B* 691.3 (2010), pp. 138–145. URL: http://linkinghub.elsevier.com/retrieve/pii/S0370269310007537.

[26] N. Agafonova et al. "Final Results of the OPERA Experiment on ν_τ Appearance in the CNGS Neutrino Beam". In: *Physical Review Letters* 120.21 (2018), p. 211801. URL: https://doi.org/10.1103/PhysRevLett.120.211801.

[27] Carlo Giunti et al. *Fundamentals of Neutrino Physics and Astrophysics*. eng. Oxford University Press, 2007.

[28] M. Tanabashi et al. "Review of Particle Physics". In: *Phys. Rev. D* 98 (3 Aug. 2018), p. 030001. URL: https://link.aps.org/doi/10.1103/PhysRevD.98.030001.

[29] Stephen King. "Neutrino Mass and Mixing in the Seesaw Playground". In: *Nuclear Physics B* 908 (Nov. 2015).

[30] C. Arnaboldi et al. "CUORE: A cryogenic underground observatory for rare events". In: *Nuclear Instruments and Methods in Physics Research, Section A: Accelerators, Spectrometers, Detectors and Associated Equipment* 518.3 (2004), pp. 775–798. arXiv: 0212053 [hep-ex].

[31] V. Álvarez et al. "NEXT-100 technical design report (TDR). Executive summary". In: *Journal of Instrumentation* 7.6 (2012). arXiv: 1202.0721.

[32] S. Andringa et al. "Current Status and Future Prospects of the SNO+ Experiment". In: *Advances in High Energy Physics* 2016 (2016). arXiv: 1508.05759.

[33] S. Fukuda et al. "Solar ^8B and hep Neutrino Measurements from 1258 Days of Super-Kamiokande Data". In: *Phys. Rev. Lett.* 86 (25 June 2001), pp. 5651–5655. URL: https://link.aps.org/doi/10.1103/PhysRevLett.86.5651.

[34] F. Capozzi et al. "Neutrino masses and mixings: Status of known and unknown 3ν parameters". In: *Nucl. Phys.* B908 (2016), pp. 218–234. arXiv: 1601.07777 [hep-ph].

[35] K. Abe et al. "Measurement of neutrino and antineutrino oscillations by the T2K experiment including a new additional sample of ν_e interactions at the far detector". In: *Phys. Rev. D* 96 (9 Nov. 2017), p. 092006. URL: https://link.aps.org/doi/10.1103/PhysRevD.96.092006.

[36] P. Adamson et al. "Combined Analysis of ν_μ Disappearance and $\nu_\mu \to \nu_e$ Appearance in MINOS Using Accelerator and Atmospheric Neutrinos". In: *Phys. Rev. Lett.* 112 (19 May 2014), p. 191801. URL: https://link.aps.org/doi/10.1103/PhysRevLett.112.191801.

[37] M. A. Acero et al. "First measurement of neutrino oscillation parameters using neutrinos and antineutrinos by NOvA". In: *Phys. Rev. Lett.* 123 (15 Oct. 2019), p. 151803. URL: https://link.aps.org/doi/10.1103/PhysRevLett.123.151803.

[38] F.P. An et al. "Observation of electron-antineutrino disappearance at Daya Bay". In: *Phys. Rev. Lett.* 108 (2012), p. 171803. arXiv: 1203.1669 [hep-ex].

[39] Y. Abe et al. "First Measurement of θ_{13} from Delayed Neutron Capture on Hydrogen in the Double Chooz Experiment". In: *Phys. Lett. B* 723 (2013), pp. 66–70. arXiv: 1301.2948 [hep-ex].

[40] J.K. Ahn et al. "Observation of Reactor Electron Antineutrino Disappearance in the RENO Experiment". In: *Phys. Rev. Lett.* 108 (2012), p. 191802. arXiv: 1204.0626 [hep-ex].

[41] K. Abe et al. "Constraint on the Matter-Antimatter Symmetry-Violating Phase in Neutrino Oscillations". In: *Nature* 580 (2020), pp. 339–344. arXiv: 1910.03887. URL: http://arxiv.org/abs/1910.03887.

[42] J.A. Formaggio and G.P. Zeller. "From eV to EeV: Neutrino Cross Sections Across Energy Scales". In: *Rev. Mod. Phys.* 84 (2012), pp. 1307–1341. arXiv: 1305.7513 [hep-ex].

[43] Irene Tamborra et al. "Self-sustained asymmetry of lepton-number emission: A new phenomenon during the supernova shock-accretion phase in three dimensions". In: *Astrophys. J.* 792.2 (2014), p. 96. arXiv: 1402.5418 [astro-ph.SR].

[44] K. Hirata et al. "Observation of a Neutrino Burst from the Supernova SN 1987a". In: *Phys. Rev. Lett.* 58 (1987). Ed. by K.C. Wali, pp. 1490–1493.

[45] R. M. Bionta et al. "Observation of a neutrino burst in coincidence with supernova 1987A in the Large Magellanic Cloud". In: *Phys. Rev. Lett.* 58 (14 Apr. 1987), pp. 1494–1496. URL: https://link.aps.org/doi/10.1103/PhysRevLett.58.1494.

[46] Thomas J. Loredo and Don Q. Lamb. "Bayesian analysis of neutrinos observed from supernova SN-1987A". In: *Phys. Rev. D* 65 (2002), p. 063002. arXiv: astro-ph/0107260.

[47] Alessandro Mirizzi et al. "Supernova Neutrinos: Production, Oscillations and Detection". In: *Riv. Nuovo Cim.* 39.1-2 (2016), pp. 1–112. arXiv: 1508.00785 [astro-ph.HE].

[48] K. Abe et al. "Real-Time Supernova Neutrino Burst Monitor at Super-Kamiokande". In: *Astropart. Phys.* 81 (2016), pp. 39–48. arXiv: 1601.04778 [astro-ph.HE].

[49] Babak Abi et al. "Deep Underground Neutrino Experiment (DUNE), Far Detector Technical Design Report, Volume II DUNE Physics". In: (Feb. 2020). arXiv: 2002.03005 [hep-ex].

[50] R. Acciarri et al. "Long-Baseline Neutrino Facility (LBNF) and Deep Underground Neutrino Experiment (DUNE): Conceptual Design Report, Volume 2: The Physics Program for DUNE at LBNF". In: (Dec. 2015). arXiv: 1512.06148 [physics.ins-det].

[51] Babak Abi et al. "Deep Underground Neutrino Experiment (DUNE), Far Detector Technical Design Report, Volume I Introduction to DUNE". In: (Feb. 2020). arXiv: 2002.02967 [physics.ins-det].

[52] B. Abi et al. "The Single-Phase ProtoDUNE Technical Design Report". In: (2017). arXiv: 1706.07081. URL: http://arxiv.org/abs/1706.07081.

[53] Russell D. Reed and Robert J. Marks. *Neural Smithing: Supervised Learning in Feedforward Artificial Neural Networks*. Cambridge, MA, USA: MIT Press, 1998.

[54] David E Rumelhart, Geoffrey E Hinton, and Ronald J Williams. "Learning representations by back-propagating errors". In: *Nature* 323.6088 (1986), pp. 533–536. URL: https://doi.org/10.1038/323533a0.

[55] George Cybenko. "Approximation by superpositions of a sigmoidal function". In: *MCSS* 2 (1989), pp. 303–314.

[56] Yann Lecun, Yoshua Bengio, and Geoffrey Hinton. "Deep learning". In: *Nature* 521.7553 (2015), pp. 436–444. arXiv: 1807.07987.

[57] L. D. Jackel et al. *Backpropagation Applied to Handwritten Zip Code Recognition*. 2008. arXiv: 1004.3732.

[58] Christian Szegedy et al. "Going deeper with convolutions". In: *Proceedings of the IEEE Computer Society Conference on Computer Vision and Pattern Recognition*. 2015. arXiv: 1409.4842.

[59] A. Aurisano et al. "A Convolutional Neural Network Neutrino Event Classifier". In: *JINST* 11.09 (2016), P09001. arXiv: 1604.01444 [hep-ex].

[60] R. Acciarri et al. "Convolutional Neural Networks Applied to Neutrino Events in a Liquid Argon Time Projection Chamber". In: *JINST* 12.03 (2017), P03011. arXiv: 1611.05531 [physics.ins-det].

[61] E. L. Snider and G. Petrillo. "LArSoft: Toolkit for simulation, reconstruction and analysis of liquid argon TPC neutrino detectors". In: *Journal of Physics: Conference Series* 898.4 (2017).

[62] Martin Abadi et al. "TensorFlow: A system for large-scale machine learning". In: *12th USENIX Symposium on Operating Systems Design and Implementation (OSDI 16)*. 2016, pp. 265–283. URL: https://www.usenix.org/system/files/conference/osdi16/osdi16-abadi.pdf.

[63] Kaiming He et al. "Delving deep into rectifiers: Surpassing human-level performance on imagenet classification". In: *Proceedings of the IEEE International Conference on Computer Vision* (2015), pp. 1026–1034. arXiv: 1502.01852.

[64] Nitish Srivastava et al. "Dropout: a simple way to prevent neural networks from overfitting". In: *Journal of Machine Learning Research* 15 (2014), pp. 1929–1958.

[65] Michael Mooney. "The MicroBooNE Experiment and the Impact of Space Charge Effects". In: *Proceedings, Meeting of the APS Division of Particles and Fields (DPF 2015): Ann Arbor, Michigan, USA, 4-8 Aug 2015*. 2015. arXiv: 1511.01563 [physics.ins-det].

[66] Tom Fawcett. "An Introduction to ROC Analysis". In: *Pattern Recognition Letters* 27.8 (2006), pp. 861–874.

[67] J. S. Marshall and M. A. Thomson. "The Pandora software development kit for pattern recognition". In: *European Physical Journal C* 75.9 (2015), pp. 1–16. arXiv: 1506.05348.